# Department of Physics and Astronomy

## University of Heidelberg

Master thesis

in Physics

submitted by

Alexander Ackermann

born in Sinsheim

2019

# Development and characterization of a

# femtosecond-pulse compressor

This Master thesis has been carried out by Alexander Ackermann

at the

Max-Planck-Institute for Nuclear Physics

under the supervision of

Priv.-Doz. Dr. José Ramón Crespo López-Urrutia

## Entwicklung und Charakterisierung eines Kompressors für Femtosekundenpulse:

Um hochpräzise Spektroskopie an hochgeladenen Ionen durchzuführen, wird ein infraroter Frequenzkamm ins Ultraviolette übersetzt durch Erzeugung hoher Harmonischer (engl. HHG) in einem Gas im Fokus eines Femtosekunden Überhöhungsresonators. Um die erforderliche Intensität von $10^{13}\,\mathrm{W/cm^2}$ bei einer Pulswiederholungsfrequenz von $100\,\mathrm{MHz}$ zu erreichen, werden 24 ps lange Pulse mit 10 W Durchschnittsleistung in einer Verstärkungsstufe für gechirpte Pulse auf 80 W verstärkt und auf unter 200 fs komprimiert.

In dieser Arbeit wird die Pulskomprimierung mit einem Gitter sowie Gitterprisma Kompressor und Puls Charakterisierung mittels frequency resolved optical gating (FROG) behandelt. Basierend auf simulierten Spektrogrammen, die experimentellen Spektrogrammen ähneln, wurde die Unsicherheit der rekonstruierten Dispersionswerte jedes vermessenenen Pulses einzeln berechnet.

Mit dem GRISM Kompressor wurden Pulsdauern von 150 fs bei 6,5 W Ausgangsleistung demonstriert. Bei hoher Leistung verschlechterten sich sowohl Komprimierung als auch Qualität des Strahlenprofils, letzteres aufgrund der Entstehung einer thermischen Linse im Prisma.

Unter Nutzung des Gitterkompressors wurde eine Pulsdauer von 223 fs bei einer mittleren Ausgangsleistung von 69 W mit leicht verzerrtem Strahlenprofil erreicht. Außerdem stimmten quantitative Dispersionsmessungen im $1\sigma$ Bereich mit der Theorie überein.

## Development and characterization of a femtosecond-pulse compressor:

For ultrahigh precision spectroscopy of highly charged ions, an infrared frequency comb is translated into the ultraviolet region by high harmonic generation in a gas target in the focus region of an intra-vacuum femtosecond enhancement cavity. To reach the required intensity of $10^{13}\,\mathrm{W/cm^2}$ at a pulse repetition rate of $100\,\mathrm{MHz}$, the initially 24 ps long pulses with 10 W of average power pass a chirped amplification stage to reach 80 W of average power at less than 200 fs pulse duration. The pulse compression with either a grating or grating prism (GRISM) compressor and pulse characterization by frequency resolved optical gating (FROG) is the subject of this thesis.

Based on simulated pulses that mimic experimental ones, an error of the reconstructed dispersion parameters was calculated for each experimental FROG trace individually.

Utilizing the GRISM compressor, pulses of 150 fs temporal FWHM were demonstrated at 6.5 W average output power. With increasing power the compression and beam profile worsened, due to thermal lensing in the prism.

Using the grating compressor, a pulse duration of 223 fs at an average output power of 69 W in combination with a slightly distorted beam profile was achieved. Furthermore, experimental quantitative dispersion measurements agreed within $1\sigma$ with the theory.

# Contents

# I  Appendix      66

# 1 Introduction

State of the art optical atomic clocks operate at a relative precision of up to $10^{-18}$ Nicholson et al. [2015]. To answer questions regarding a potential variation of fundamental constants, e.g. the fine structure constant $\alpha$, even higher precision is required. Current clocks are limited by energy level shifts due to black body radiation, Stark effect and Zeeman shift. Highly charged ions are less sensitive to these effects because remaining electrons are tightly bound due to the high charge state. Therefore, the electronic wave packet is highly compact, which reduces the coupling to external electromagnetic fields. Consequently HCIs were suggested as clock candidates for the development of the next frequency standard Safronova et al. [2014a], Derevianko et al. [2012], Safronova et al. [2014b], Schiller [2007]. The current accuracy of atomic clocks will be improved by one order of magnitude to a relative precision on the $10^{-19}$ level Derevianko et al. [2012], facilitating even more precise measurements of universal constants.

Astronomical observations suggest a spatial gradient of $\alpha$ that leads to variations over cosmological distances Webb et al. [2011]. Since the solar system moves in the framework of the $\alpha$ dipole, the spatial variation of $\alpha$ should be detectable in terrestrial studies as a shift in time at a rate of $\dot{\alpha}/\alpha \quad 10^{-19} \, \mathrm{yr}^{-1}$ Berengut and Flambaum [2012]. Currently, by comparison of a $\mathrm{Hg}^+$ and a $\mathrm{Al}^+$ clock a variation of $\dot{\alpha}/\alpha = (-1.6 \pm 2.3) \cdot 10^{-17} \, \mathrm{yr}^{-1}$ Rosenband et al. [2008] is detectable. Certain highly charged ions possess transitions that include metastable states, and are strongly sensitive to variation of $\alpha$ Safronova et al. [2014b]. Utilizing HCI clocks the precision of $\alpha$ variation could be increased by two orders of magnitude Berengut et al. [2011].

Moreover due to their mentioned properties HCIs are suited for tests of strong field quantum electrodynamics. Furthermore a large portion of the baryonic matter in the universe consists of HCIs. They are found in active galactic nuclei, stellar coronae, in supernova remnants and in accretion disks. Thus, knowledge about HCIs is vital to understand astrophysical processes in our universe.

Therefore we develop an experiment for ultrahigh precision spectroscopy of HCIs, which is depicted in Fig. 1.1. The needed HCIs are produced in an electron beam ion trap (EBIT). An intense beam of highly energetic electrons, compressed and guided by a magnetic field, ionizes atoms and in conjunction with the magnetic field radially traps the produced ions due to its negative space charge Levine et al. [1988]. Additionally, drift tubes generate a potential well in the longitudinal direction to complete the three dimensional trapping. Due to collisions of ions and high energetic electrons, temperatures of $10^6 \, \mathrm{K}$ arise and result in Doppler broadening of HCI emission lines that limit spectroscopy precision in the EBIT to the ppm range Bekker et al. [2015]. To overcome this, HCIs are extracted from the EBIT and transferred
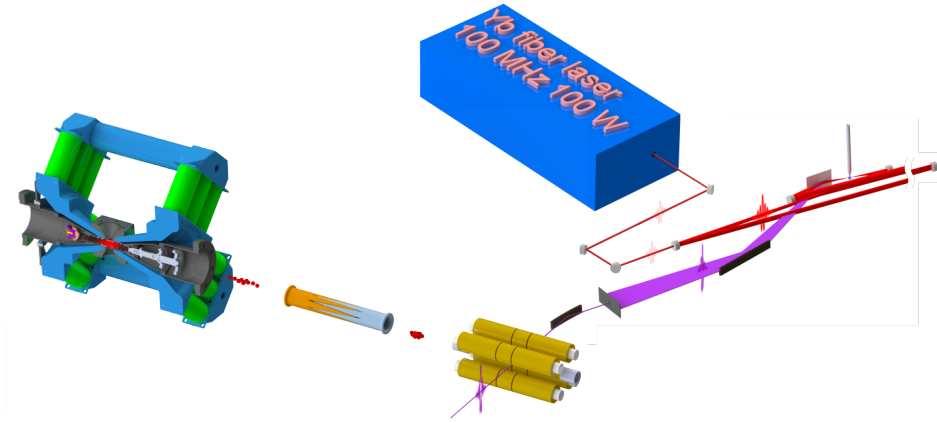
Figure 1.1: Sketch of the future experiment for ultrahigh precision spectroscopy of HCIs. HCIs are produced in an EBIT (on the left in blue and green), then cooled down and transported to a cryogenic Paul trap (in the center in yellow) and then spectroscopy is carried out by a XUV frequency comb generated in a intra-vacuum enhancement cavity (on the right).

to a linear Paul trap, where they are sympathetically laser-cooled by $Be^+$ ions to mK temperatures Schmöger et al. [2015], as part of MPIK's 'Cryogenic Paul Trap Experiment' (CryPTEx).

Since most transitions of HCIs are located in the extreme ultraviolet (XUV) region, the aim of this experiment is to generate a XUV frequency comb by high harmonic generation (HHG) of a driving Ytterbium-doped fiber-based infrared frequency comb. The laser possesses a 14 nm bandwidth centered around 1038 nm. To facilitate HHG, intensities on the order of $10^{13}$ W/cm² are required. In order to achieve such a high intensity, the beam is focused to a 14 μm diameter inside a femtosecond enhancement cavity. Due to the high repetition rate of 100 MHz, the laser has to be amplified before entering the cavity, which is accomplished by chirped pulse amplification.

This thesis covers the modeling and commissioning of two different compressor setups to compensate present dispersion in the uncompressed 24 ps long pulses and consequently compress them down to 200 fs. Also a home-built multishot second harmonic generation frequency resolved optical gating setup is commissioned and then used for pulse characterization.

# 2 Theory

## 2.1 Dispersion

This chapter is dedicated to the theory of dispersion of electromagnetic waves and its effects on laser pulse propagation. First, a short introduction to the frequency and time domain representations of the electric field is given, then the influence of the spectral phase on pulses will be investigated. At last, experimental setups for dispersion compensation will be introduced.

### 2.1.1 Electromagnetic pulses

Electromagnetic pulses are conveniently described in a complex representation, while still only the real part is a measurable quantity. In the slowly varying envelope approximation, which is valid even for few-cycle pulses Agrawal [2000], a product of a slowly varying envelope and a rapidly oscillating part, characterized by the phase $\phi(t)$, constitutes the temporal electric field as

$$\tilde{E}(t) = \varepsilon(t)\mathrm{e}^{i\phi(t)}, \tag{2.1}$$

where $\varepsilon(t)$ is the envelope and $\phi(t)$ the temporal phase. Expanding the temporal phase $\phi(t)$ into a Taylor series yields

$$\phi(t) = \phi_{\mathrm{CEO}} + \omega_0 t + \varphi(t), \tag{2.2}$$

where $\phi_{\mathrm{CEO}}$ is the carrier to envelope offset phase, $\omega_0$ the central frequency and $\varphi(t)$ contains phase terms of higher order in time. If $\varphi(t) = 0$, the oscillation imprinted into the envelope is constant and given by $\omega_0$. $\phi_{\mathrm{CEO}}$ defines the offset of that oscillation with respect to the envelope, see Fig. 2.1. The first time derivative of the temporal phase is called instantaneous frequency

$$\omega(t) = \omega_0 + \frac{\mathrm{d}\varphi(t)}{\mathrm{d}t}. \tag{2.3}$$

As depicted in Fig. 2.1, time and frequency domain are connected. This connection is mathematically based on the Fourier transformation ($\mathcal{F}$) as follows

$$\tilde{E}(\omega) = \mathcal{F}[\tilde{E}(t)] = \int_{-\infty}^{+\infty} \tilde{E}(t)\mathrm{e}^{-i\omega t}\mathrm{d}t = \varepsilon(\omega)\mathrm{e}^{i\phi(\omega)}, \tag{2.4}$$

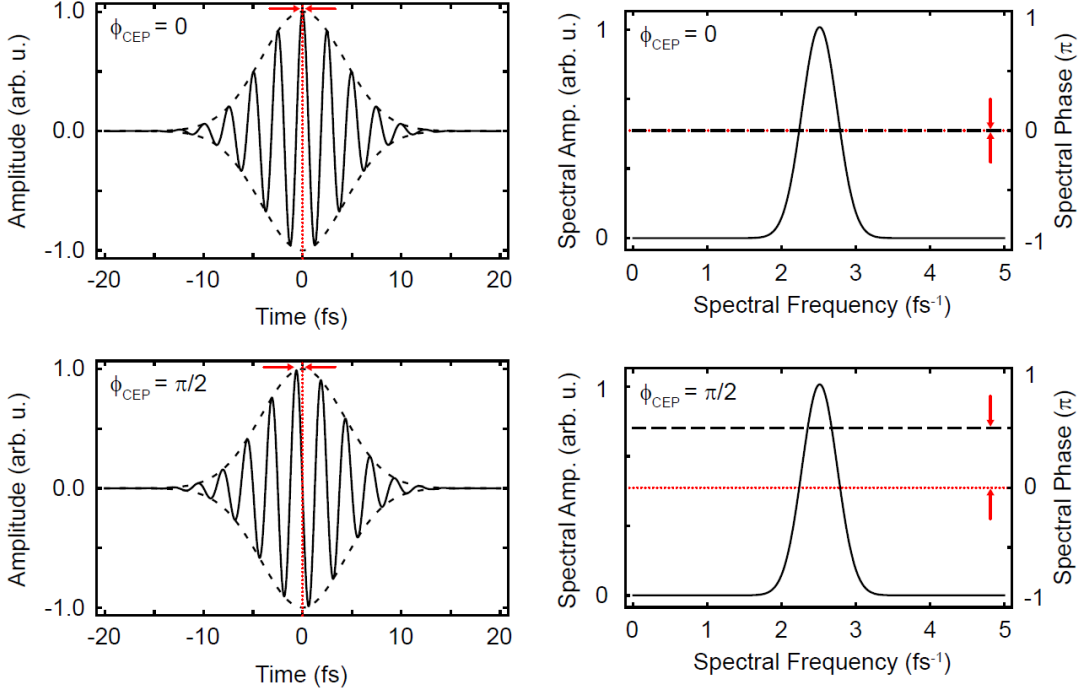where $\tilde{E}(\omega)$ is the electric field in the frequency domain, $\varepsilon(\omega)$ is the envelope in

Figure 2.1: Gaussian pulses represented in time (left) and frequency domain (right) for $\phi_{\text{CEO}} = 0$(top) and $\phi_{\text{CEO}} = \pi/2$ (bottom). In the time domain graphs, the dashed line depicts the envelope, the solid one the carrier frequency. The envelope is centered around $t = 0$ indicated by the red dashed line. In The frequency domain graphs, the solid line corresponds to the spectral intensity, the dashed line to the spectral phase and the red dashed line to the zero point of spectral phase. The red arrows mark the definition of the CEO in each respective domainOtt [2012].

frequency domain and $\phi(\omega)$ the spectral phase. Inverse Fourier transformation ($\mathcal{F}^{-1}$) of $\tilde{E}(\omega)$ transfers it back to the time domain

$$\tilde{E}(t) = \mathcal{F}^{-1}[\tilde{E}(\omega)] = \frac{1}{2\pi} \int_{-\infty}^{+\infty} \tilde{E}(\omega)\mathrm{e}^{i\omega t}\mathrm{d}\omega. \tag{2.5}$$

Both domains contain full information about the pulse. As time and frequency domain are connected by the Fourier transformation, spectral bandwidth $\Delta\omega_p$ and pulse duration $\tau_p$ are so as well and fulfill the uncertainty relation of Fourier analysis

$$\tau_{\text{p}}\Delta\omega_{\text{p}} = 2\pi\Delta\nu_{\text{p}}\tau_{\text{p}} \geq 2\pi c_{\text{B}}. \tag{2.6}$$

Here $c_{\text{B}}$ is a constant dependent on the pulse shape and $\nu_{\text{p}}$ is the bandwidth in units of ordinary frequency. If equality holds for Eq.2.6 the pulse is called transform- or Fourier-limited.

## 2.1.2 Spectral phase

This subchapter is dedicated to the spectral phase which is the most important quantity in regards to the pulse shape. Therefore understanding its influence on ultrashort pulses is vital to understand pulse compression.

The spectral phase can be expanded into a Taylor series

$$\phi(\omega) = \sum_{k=0}^{\infty} \frac{1}{k!} \frac{\mathrm{d}^k \phi(\omega)}{\mathrm{d}\omega^k} \omega^k = \phi_{\mathrm{ceo}} + \tau_0 \omega + \varphi(\omega), \tag{2.7}$$

where $\varphi(\omega)$ consists of terms of higher order in frequency. Then the Group Delay (GD) is obtained by

$$\tau(\omega) = -\frac{\mathrm{d}\phi(\omega)}{\mathrm{d}\omega} = -\tau_0 - \frac{\mathrm{d}\varphi(\omega)}{\mathrm{d}\omega}. \tag{2.8}$$

The GD is the analogue of frequency domain, to the instantaneous frequency Eq. 2.3 of the temporal domain and describes the temporal delay of the envelope as a function of frequency, if $\varphi(\omega)$ is nonzero. Utilizing the shifting theorem of the Fourier transformation, the effect on a laser pulse of each term of the spectral and temporal phase can be explained. Linear phase terms in any domain give rise to an offset in the other domain, without changing the pulse shape, see Fig.2.4. Higher order terms are
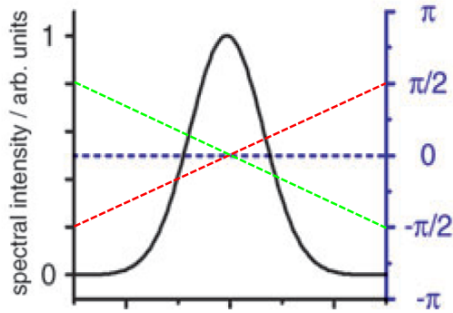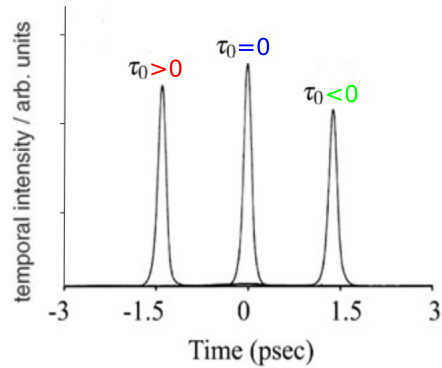


Figure 2.2: Frequency domain



Figure 2.3: Time domain

Figure 2.4: Constant or linear spectral phase terms, shift the pulse as a whole in time domain, according to Eq. 2.8.

more interesting, since they cause frequency dependent shifts. These are responsible for compressing or stretching pulses and more complex effects. Spectral phase terms of second order yield a GD with linear dependence on the frequency. Therefore high and low frequencies experience a temporal delay in opposite directions, which either stretches or compresses the pulse, see Fig. 2.7. This is called group delay dispersion (GDD), second order dispersion or linear chirp, because the instantaneous frequency either rises or falls with time. The GDD is calculated by the second derivative of

the spectral phase

$$\text{GDD} = \frac{d^2\phi}{d\omega^2}\bigg|_{\omega_0}.$$  (2.9)

A spectral phase dominated by it's third order, leads to a GD of quadratic de-
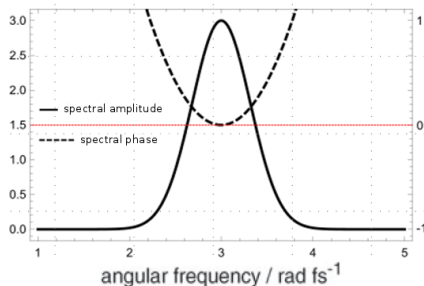


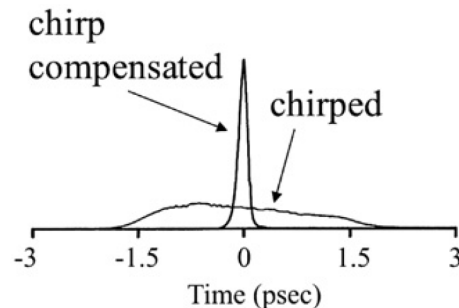Figure 2.5: Frequency domain



Figure 2.6: Time domain

Figure 2.7: Quadratic spectral phase terms stretch or compress the pulse in time domain, according to Eq. 2.8.

pendence on the frequency. Consequently, high and low frequencies are shifted in the same direction in time. This causes them to interfere. The produced beat note manifests in trailing or leading pulses, see Fig. 2.10. This type of dispersion is called third order dispersion (TOD) and is calculated by

$$\text{TOD} = \frac{d^3\phi}{d\omega^3}\bigg|_{\omega_0}.$$  (2.10)

## 2.1.3 Grating pair

In parallel arrangement, as in Fig. 2.11, a grating pair can act as a pulse compressor with the aid of the angular dispersion that is caused by diffraction. To investigate the dispersive behavior of a grating pair in detail, two frequency components propagating through the assembly will be considered: the central frequency $\omega_0$, solid line, and another arbitrary frequency component $\omega$ inside the spectrum, dashed line. After the first grating the two frequency components diverge due to their differing diffraction angles, according to the ordinary grating equation of reflective gratings

$$n\lambda = \frac{1}{g}(\sin(\theta_n) + \sin(\theta_i)),$$  (2.11)

where $g$ is the grating constant in lines per unit length, $\theta_i$ the incident angle and $\theta_n$ the outgoing angle of the $n$-th diffraction order's main maximum. The described frequency dependent fanning out is called angular dispersion. The second grating
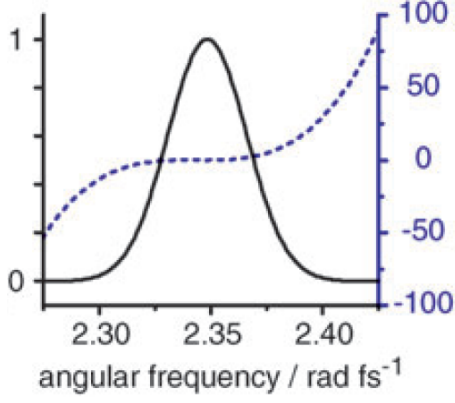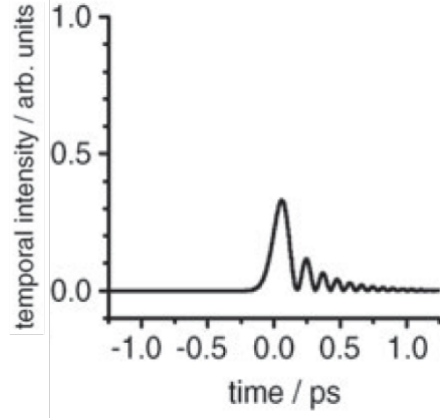
11

Figure 2.8: Frequency domain



Figure 2.9: Time domain

Figure 2.10: Cubic spectral phase terms, shift high and low frequencies in the same direction in time, according to Eq. 2.8. This leads to a beating effect that generates satellite pulses.

in parallel alignment compensates the angular dispersion again. Now all frequency components travel parallel to each other, in other words the beam has a spatial chirp. To remove this spatial chirp a retroreflector guides the beam back through the assembly. The optical path length is given by

$$L_{\text{opt}}(\omega) = \overline{ACP} = b/(\cos((\mu' + \delta)(\omega)))[1 + \cos(\mu + (\mu' + \delta)(\omega))], \tag{2.12}$$

where $\mu$ is the incident angle, $\mu'$ the diffraction angle of $\omega_0$ and $\delta$ the deviation angle between $\omega$ and $\omega_0$. Furthermore at every groove a phase shift of $-2\pi$ is inferred B. Treacy [1969], but only the difference between the two frequency components is relevant. The acquired total phase shift is described by

$$\phi(\omega) = \frac{\omega}{c} L_{\text{opt}(\omega)} - 2\pi bg \tan((\delta + \mu')(\omega)). \tag{2.13}$$

The second derivative of the spectral phase yields the GDD

$$\frac{\mathrm{d}^2\phi}{\mathrm{d}\omega^2}\bigg|_{\omega_0} = -\frac{\lambda_0^3}{2\pi c^2} g^2 \frac{b}{\sqrt{r}} \frac{1}{r}, \tag{2.14}$$

with the central wavelength $\lambda_0$, c the speed of light and $r = 1 - \left[\frac{2\pi cg}{\omega_0} - \sin\mu\right]^2 = \cos\mu'^2$. The TOD is then given by the third derivative

$$\frac{\mathrm{d}^3\phi}{\mathrm{d}\omega^3}\bigg|_{\omega_0} = -\frac{3\lambda_0}{2\pi cr}[r + \lambda_0 g(\lambda_0 g - \sin\mu)]\frac{\mathrm{d}^2\phi}{\mathrm{d}\omega^2}\bigg|_{\omega_0}. \tag{2.15}$$

A grating pair only generates negative GDD and positive TOD and therefore usually exacerbates present positive TOD. The ratio of TOD over GDD increases with
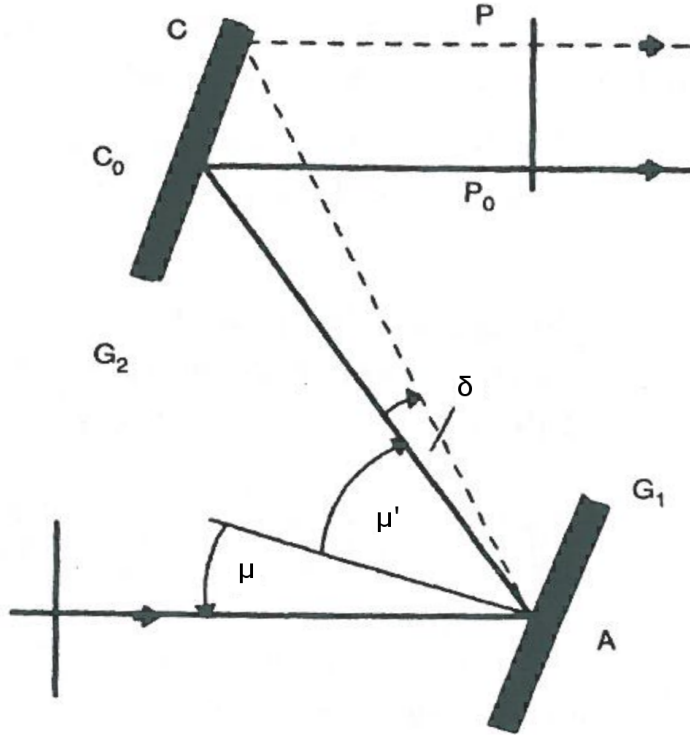
Figure 2.11: Beam path of two frequency components through a parallel grating pair (G1 and G2). The central frequency $\omega_0$ travels along $\overline{AC_0 P_0}$, while the arbitrarily chosen component $\omega$ along $\overline{ACP}$. $\mu$ is the incident angle for both, while $\omega_0$ is diffracted by $\mu'$ and $\omega$ by $\mu' + \delta$.

rising grating constant and it also changes with the incident angle Hemmer [2011]. However, our grating is a volume phase holographic grating and thus underlies the Bragg phase matching condition, which denies this degree of freedom because the grating has to be entered in a specific angle to be diffracted with minimal losses.

## 2.2 Pulse characterization

In this chapter pulse characterization techniques, starting from intensity autocorrelation and evolving into Frequency Resolved Optical Gating (FROG), are presented.

### 2.2.1 Autocorrelation

To measure the duration of a signal, a shorter reference signal is mandatory. However on the femtosecond timescale such a signal is not available since electronic signals are typically much slower. This obstacle is overcome in an autocorrelator, by referencing a signal with itself. The basic principle of an autocorrelator is to check the correlation of the temporal pulse trace with itself. Therefore the pulse is split at a beam splitter, then the two replicas are delayed with respect to each other and overlapped again in a medium with a nonlinear response to the laser-intensity. In an intensity autocorrelator, which is present in our experimental setup, the intensity of the second

harmonic is measured against the time delay $\tau$, which is described by

$$A_{\mathrm{c}}(\tau) = \int_{-\infty}^{+\infty} I_2(t)I_1(t-\tau)\mathrm{d}t, \tag{2.16}$$

where $I_1(t-\tau)$ is the intensity of the pulse delayed by $\tau$ to the other replica with intensity $I_2(t)$. A pulse shape has to be guessed and fitted to the measured data to obtain an estimate for the pulse duration. In a more rigorous fashion, the Fourier transformed intensity autocorrelation has to be computed

$$A_{\mathrm{c}}(\omega) = I_1(\omega)I_2^*(\omega), \tag{2.17}$$

where $I_{(\omega)}$ is the Fourier transform of a pulse

$$\mathcal{F}[I_{\mathrm{j}}(t)] = I_{\mathrm{j}}(\omega) = \int_{-\infty}^{+\infty} I_{\mathrm{j}}(t)\mathrm{e}^{-i\omega t}\mathrm{d}t. \tag{2.18}$$

Then divide this Fourier transformed autocorrelation by the Fourier transform of the reference signal $A_{\mathrm{c}}(\omega)/I_{\mathrm{r}}(\omega) = I_{\mathrm{s}}^*(\omega)$ and inverse-Fourier transform the quotient back into time domain to obtain the desired temporal profile $I_s(t)$. Since the signal is referenced by itself the autocorrelation is always symmetrical. As a result many symmetric and asymmetric pulses may produce the same autocorrelation. An autocorrelation provides an estimate of the pulse length, but information about frequency and phase modulation cannot be obtained.

## 2.2.2 Frequency resolved optical gating

A more sophisticated pulse characterization method called frequency resolved optical gating (FROG) overcomes the shortcomings of an autocorrelation and enables the extraction of pulse energy, duration, spectrum and the spectral as well as temporal phase. Equations of this subchapter are taken from DeLong et al. [1994a], if not referenced otherwise.

FROG consists of two main parts: First an experimental apparatus including an autocorrelator and a spectrometer, as shown in Fig.2.12. After the nonlinear medium spectra are recorded at different time delays between the two replicas of the pulses. Second a phase-retrieval-based algorithm is used to extract the complete intensity and phase evolution from the measured FROG trace. There are several FROG schemes, distinguished by different nonlinearities. The focus in this thesis will be on Second Harmonic Generation (SHG) FROG, because this is the scheme used in our experiment. In SHG FROG the two split pulse replicas are focused non-collinearly into a frequency doubling crystal, which yields a fast nonlinear optical response. This results in an envelope of the signal field obeying

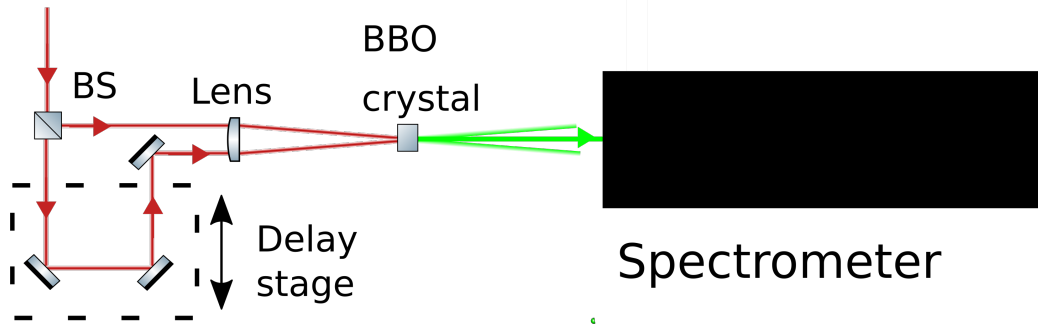$$E_{\mathrm{sig}}(t,\tau) = E(t)E(t-\tau), \tag{2.19}$$

Figure 2.12: Schematic experimental setup for FROG trace measurements. The incoming beam is split at the beam splitter, the split beams are delayed with respect to each other, then focused into a nonlinear medium. Finally the resulting beam is spectrally resolved as a function of time delay.

where $E(t)$ is the complex envelope of the pulse to be measured and $\tau$ is the time delay between the two pulses. Then this signal is spectrally resolved in a spectrometer as a function of time delay $\tau$ and yields a spectrogram, called the FROG trace

$$I_{\text{FROG}}(\omega, \tau) = \left| \int_{-\infty}^{\infty} E_{\text{sig}}(t, \tau) \exp(-i\omega t) \mathrm{d}t \right|^2 . \tag{2.20}$$

Since the signal field of Eq.(2.19) is invariant (except for a temporal offset) with respect to a change of sign of the delay time $\tau$, the SHG FROG trace is always symmetric in time: $I_{\text{FROG}}(\omega, \tau) = I_{\text{FROG}}(\omega, -\tau)$. This results in a temporal ambiguity which is the main shortcoming of SHG FROG compared to a FROG version utilizing a third-order nonlinearity. This ambiguity only affects phase distortions which are even functions of time, like linear chirp. However, a cubic phase in time does not have an ambiguous sign. Furthermore the temporal ambiguity can be eliminated if *a priori* knowledge of the pulse is available. For example, usually positive dispersion is accumulated by propagation through normal optics. Another option is to record two traces. One is recorded just as described above, the other with a piece of bulk glass placed into the beam path which introduces a known amount of dispersion. Then by comparison of the retrieved pulses' phases the sign of linear chirp can be extracted.

The FROG trace expression above needs to be recast into the form of the two-dimensional phase retrieval problem before it can be inverted Trebino and Kane [1993]. Therefore the Fourier transform of $E_{\text{sig}}(t, \tau)$ with respect to $\tau$ is considered, which will be called $E_{\text{sig}}(t, \Omega)$. It suffices to find $E_{\text{sig}}(t, \Omega)$ because the original pulse field is given by $E(t) = E_{\text{sig}}(t, \Omega = 0)$. The FROG trace in terms of $E_{\text{sig}}(t, \Omega)$ is

given by

$$I_{\text{FROG}}(\omega, \tau) = \left| \int_{-\infty}^{\infty} E_{\text{sig}}(t, \Omega) \exp(-i\omega t - i\Omega\tau) \mathrm{d}t \mathrm{d}\Omega \right|^2. \tag{2.21}$$

This shows that the measured FROG trace, $I_{\text{FROG}}(\omega, \tau)$, is the squared absolute value of the 2D Fourier transform of $E_{\text{sig}}(t, \Omega)$. Thus it yields the absolute value, but not the phase of $E_{\text{sig}}(t, \Omega)$. That leaves one with the 2D phase-retrieval problem, which is a solved problem if one has additional information about $E_{\text{sig}}(t, \Omega)$. Fortunately this is the case since the mathematical form of $E_{\text{sig}}(t, \tau)$ is known.

### FROG retrieval algorithm

The algorithm is based on iterative Fourier-transform algorithms used in phase retrieval problems. Several pulse retrieval algorithms have been published Paye et al. [1993], DeLong and Trebino [1994], DeLong et al. [1994c], Kane and Trebino [1993]. Here, the focus will be on the general principal of FROG phase-retrieval algorithms. The goal of the pulse retrieval problem is to find a signal field $E_{\text{sig}}(t, \tau)$ that satisfies the following two constraints: First, the field's FROG trace computed by Eq.(2.20) has to match the experimentally measured trace. Second, it has to obey Eq. (2.19) forming a physically realizable field. In a function space of complex two dimensional functions where each point represents a possible $E_{\text{sig}}(t, \tau)$, the two constraints generate two sets. The intersection of these sets represents the correct solution.
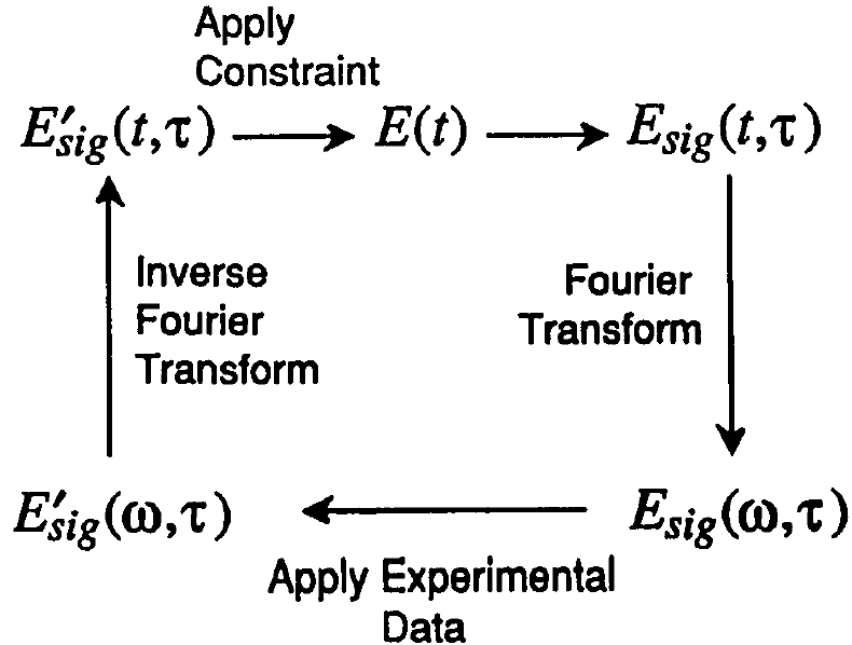The general principle of the algorithm is depicted in Fig. 2.13. An initial guess



Figure 2.13: Sketch of FROG pulse-retrieval algorithm.

for the field $E(t)$ is made, then by applying Eq.(2.19) and a Fourier transform, a signal field is generated. The squared absolute of this frequency domain signal field $E_{\text{sig}}(\omega, \tau)$ yields the trial field's FROG trace. Now the first constraint is applied by limiting the absolute value of $E_{\text{sig}}(\omega, \tau)$ to the measured FROG trace's absolute value. Then an inverse Fourier-transform into the $(t, \tau)$ domain is applied. To implement the other constraint a signal field must be found that satisfies Eq.(2.19) and is closest to $E'_{\text{sig}}(t, \tau)$, where $'$ refers to the absolute value limitation. The metric used to measure this 'closeness' is given by

$$Z = \sum_{t,\tau=1}^{N} \mid E'_{\text{sig}}(t, \tau) - E_{(}t)E(t - \tau) \mid^2 . \tag{2.22}$$

By minimization of Z with respect to $E(t)$ the signal field closest to $E'_{\text{sig}}(t, \tau)$ inside constraint set two is found. Simultaneously this provides the guess for $E(t)$ for the next cycle of the algorithm. The success of a pulse retrieval is quantified by the "FROG error", which is the root mean square difference between the measured trace and the trace computed from the retrieved pulse field. It is given by

$$G = \sqrt{\frac{1}{N^2} \sum_{i,j=1}^{N} \left| I_{\text{FROG}}(\omega_i, \tau_j) - \alpha I^k_{\text{FROG}}(\omega_i, \tau_j) \right|^2}, \tag{2.23}$$

where $\alpha$ is a real scaling parameter to minimize G and $\omega_i$ and $\tau_j$ are coordinates in frequency and time delay axes on a N x N grid. Each trace is put onto such a grid, where each point corresponds to the intensity of the trace at a certain frequency and time delay indicated by $\omega_i, \tau_j$. Furthermore the step sizes on the two axes have to be Fourier related.

Regarding the experimental realization of a FROG setup the frequency doubling crystal's thickness $L$ has to be considered. Since a group velocity mismatch in the crystal between fundamental and second harmonic beams arises, which lowers the retrievals' accuracy if left unregarded. The group velocity mismatch acts as a finite temporal impulse-response function that is convoluted with the second-harmonic signal. The width of this response function is

$$t_\omega = \left( \frac{1}{v_g^{SHG}} - \frac{1}{v_g^{fund}} \right) L, \tag{2.24}$$

where $v_g$ is the group velocity. In the perspective of the frequency domain this acts as a frequency-dependent filter described by

$$F(\omega) = \left( \frac{sin(t_\omega \omega/2)}{t_\omega \omega/2} \right)^2, \tag{2.25}$$

that is multiplied with the emerging SHG signal spectrum. As a result the bandwidth of the retrieved pulse will be narrower than the bandwidth of the actual pulse.

Additionally the phase evolution may be highly distorted. To minimize this effect the crystal thickness should be kept small. It was found by DeLong et al. [1994a] that if the half-width at half-maximum of the spectral filter in Eq.(2.25), which evaluates to $t_\omega/2.78$, is larger than 1.4 times the spectral half-width at half-maximum of the SHG signal, the effects of group-velocity mismatch cause less than 10% error in the retrieved pulse parameters. Moreover when providing experimental data to the algorithm, the size of the increment in time and in wavelength has to be included as well. Inaccuracies in these calibrations translate to errors of the same order of magnitude in retrieved pulse parameters.

An useful feature of FROG is the ability to validate the measurement data. There are two types of feedback. First a probabilistic one, which stems from the fact that the FROG trace is a N x N array of points, used to determine N intensity points and N phase points. This leads to significant overdetermination of the pulse intensity and phase. Consequently it is unlikely that a trace composed of randomly generated points corresponds to an actual pulse. Similarly, the likelihood of a measured trace contaminated by systematic error to correspond to an actual pulse is very small. Thus convergence of the algorithm to a pulse whose trace agrees well with the measured trace suggests that the trace is free of systematic error Trebino et al. [1997]. The other feedback mechanism uses "marginals" of the FROG trace, which are integrals of the trace with respect to delay or frequency. Marginals are a powerful tool since they are related to other independently measurable quantities such as the spectrum and autocorrelation. Therefore measuring the FROG trace and a marginal with independent apparatuses allows to check if the relationship between the two holds. This either confirms a correct calibration of the apparatuses or indicates shortcomings of the measurement setup. The frequency marginal is the integral of the FROG trace along the delay axis and is defined as

$$M_\omega(\omega) = \int_{-\infty}^{\infty} \mathrm{d}\tau I_{\mathrm{FROG}}(\omega, \tau). \tag{2.26}$$

Its form depends on the used nonlinearity and for SHG is given by

$$M_\omega^{SHG}(\omega) = 2I(\omega) * I(\omega), \tag{2.27}$$

where $*$ indicates a convolution. The frequency marginal comparison was found to be useful in checking for sufficient phase-matching bandwidth, crystal angle orientation and for proper calibration of the varying spectral response of spectrometers and CCD detectors Taft et al. [1996].


## FROG traces

SHG FROG traces are unintuitive because of the time ambiguity mentioned earlier. Polarization gate (PG) FROG traces on the other hand use a third order nonlinearity, which does not contain a time ambiguity. Therefore they are usually a good approximation to the instantaneous frequency as a function of time and thus much

easier to understand. For each phase distortion the PG trace will be explained first and then the SHG case.

In the following figures FROG traces are depicted as two dimensional color maps, where the intensity is encoded in the color. White corresponds to low intensities and blue to high intensities. On the x-axis the time delay between pulses in the nonlinear medium is displayed, on the y-axis the resulting signal is spectrally resolved.

The special case of no phase distortion, which means the phase is constant or linear,
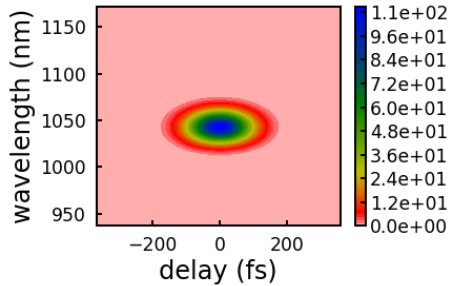


Figure 2.14: PG FROG trace
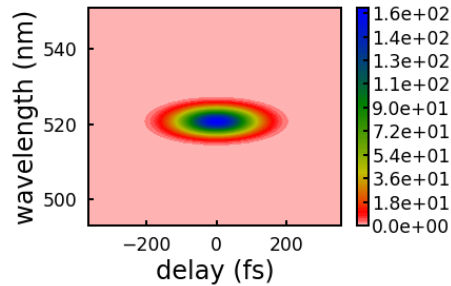
Figure 2.15: SHG FROG trace

Figure 2.16: FROG traces without phase distortion.

will be presented first. The frequency components are evenly distributed over the temporal pulse profile and the trace is shaped like an ellipse for all FROG setup geometries, as shown in Fig. 2.16. When the trailing edges of the pulses overlap in a nonlinearly responding medium, the weak frequency wings are suppressed in comparison to the center of the spectrum in a gaussian spectrum, leading to the elliptic shape.

For positive linear chirp, GDD in other words, which means the phase has a dominant positive second order coefficient, the leading edge of a pulse (negative times) has a lower frequency than the trailing edge. Vice versa for the case of negative linear chirp. This means the instantaneous frequency as a function of time is linear, which results in a tilted PG FROG trace, see Fig. 2.17a. Due to the time ambiguity
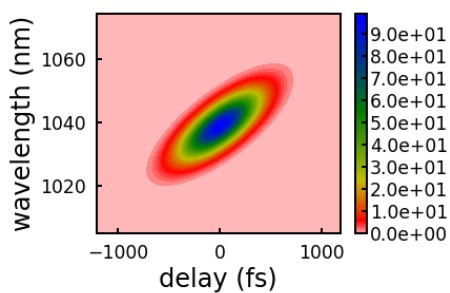


(a) PG FROG trace
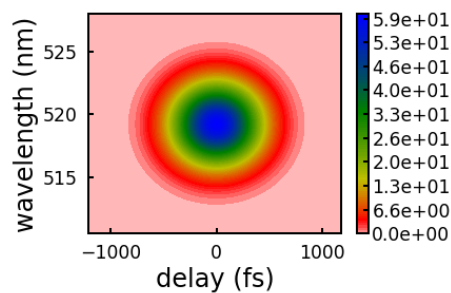
(b) SHG FROG trace

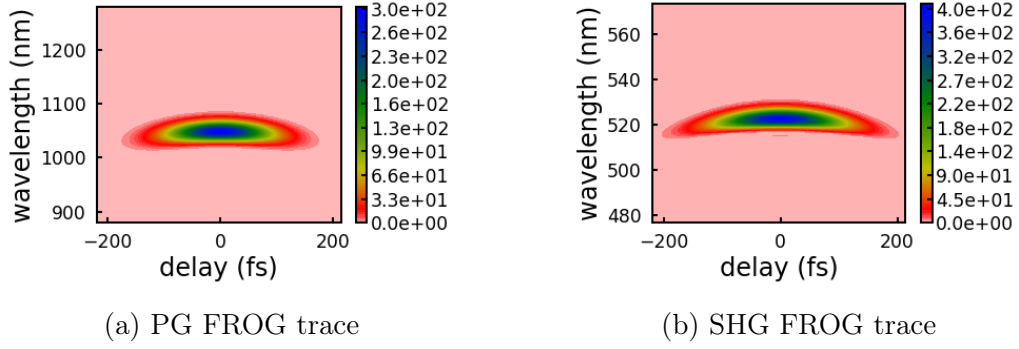Figure 2.17: FROG traces with linear chirp.

(a) PG FROG trace       (b) SHG FROG trace

Figure 2.18: FROG traces with temporal cubic phase.



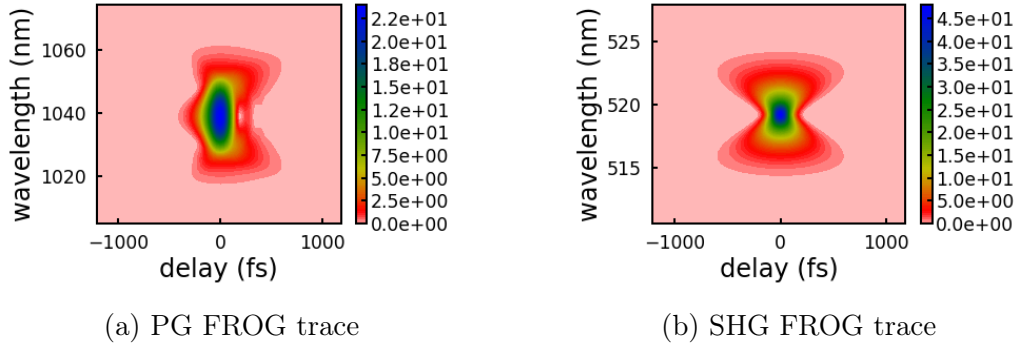(a) PG FROG trace       (b) SHG FROG trace

Figure 2.19: FROG traces with spectral cubic phase.

the sign of the chirp cannot be determined in SHG FROG and therefore the trace in Fig. 2.17b b), does not inhibit a slope. Still the amount of chirp can be estimated by the spectral width of the trace at time delay $\tau = 0$.

The next phase distortion to be investigated is the temporal cubic phase. A pulse with positive temporal cubic phase has higher frequencies in the leading and the trailing edges than the center of the pulse. Therefore the instantaneous frequency has a parabolic shape, that the FROG trace closely follows, see Fig. 2.18b. Since the higher frequencies are present at two different times there is a beating effect, which generates satellite pulses.

A spectral cubic phase (SCP), causes TOD as discussed earlier. High and low frequencies acquire more delay than intermediate frequencies. As a result intermediate frequencies are located in the leading edge and center of the pulse, but both high and low frequencies are in the trailing edge, as shown in Fig.2.19a. The latter leads to a beating phenomenon which causes satellite pulses in time domain. The SHG trace shows a parabolic feature as well, but due to the time ambiguity that feature is symmetric in time. Therefore the SHG FROG trace of dominant SCP as phase distortion is shaped like an hourglass, see Fig 2.19b and the sign of SCP cannot be determined.

An often encountered pair of phase distortions is the combination of linear chirp and spectral cubic phase, which is typical in chirped pulse amplification when the
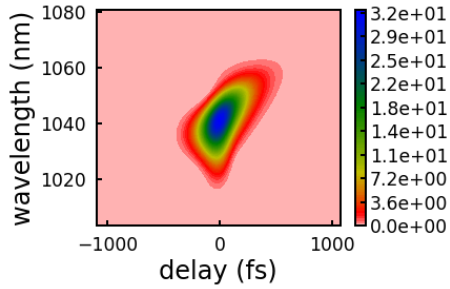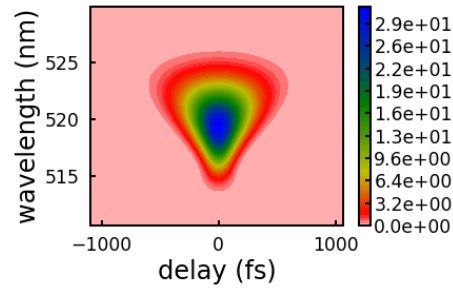
Figure 2.20: PG FROG trace

Figure 2.21: SHG FROG trace

Figure 2.22: FROG traces with linear chirp and spectral cubic phase.

compressor is not adjusted properly. As can be seen in Fig. 2.22 the traces look very similar to the case of only SCP. The difference here is that the amount of SCP is so small, that in the absence of linear chirp the temporal intensity profile of the pulse would not show any satellite pulses. As a consequence the presence of linear chirp amplifies the effects of spectral cubic phase.

## 2.3 High Harmonic Generation

This chapter covers the process of transferring near-infrared (IR) light into the ultraviolet region by generation of high harmonics (HH).

HHG can be explained by the so called three-step model Krause et al. [1992]. In the first step a laser field of the order of the binding electric field of the nucleus, lowers the potential barrier of the atom, which allows a bound electron to tunnel into the continuum. In the second step, the freed electron's movement is now governed by the oscillating laser electric field. Consequently it is accelerated away from the ion and then returns to the ion in the reversed laser field. In the third and last step the electron may recombine with the parent ion, thus releasing acquired kinetic energy and ionization energy in form of an ultraviolet photon. The accumulated kinetic energy depends on the time of release from the parent atom within the phase of the laser cycle and is greatest if the electron is freed just beyond the peak of the pulse. The first step, ionization, is governed by the Keldysh parameter $\gamma = \sqrt{I_{\mathrm{p}}/2U_{\mathrm{p}}}$, where $I_p$ is the binding potential of the nucleus felt by the bound electron and $U_{\mathrm{p}} = e2E_0^2/(4m\omega^2)$ is the ponderomotive potential, where $e$ is the elementary electric charge, $E_0$ is the laser electric field amplitude, $\omega$ its angular frequency and $m$ the mass of the electron. There are three ionization regimes of an atom induced by an optical field. For small fields, i.e. large Keldysh parameters $\gamma > 1$, the ionization rate is described by a power law of the laser intensity. This is called the multiphoton ionization regime, which is not of importance to HHG and will not be discussed further. The regime where $\gamma \leq 1$ but the electric field is still smaller than the binding electric field is of most interest to HHG Attwood and Sakdinawat [2017]. In this

regime the ionization rate follows an exponential dependence on the laser intensity. The third regime is characterized by the lack of an energy barrier separating the electron from free space and thus is called the barrier-suppression regime. It is reached at even stronger fields as in the previous regime, i.e. Keldysh parameters $\gamma \ll 1$. Here the ionization rate has a nearly linear dependency on the incident electric field.

In the second step, after ionization, it is assumed that the electron exits the atom at zero kinetic energy and that the residual field of the ion is negligible. Therefore the electron's movement is dominated by the laser field and can be described purely classically. From numerical calculations the the position of the electron as function of time for different ionization times relative to the phase of the electric field is determined and depicted in Fig. 2.23 a). Right beneath the kinetic energy of the electron upon first encounter with the nucleus is plotted again as a function of ionization times, Fig 2.23 b). A maximum is reached at a phase of 198° and 18°
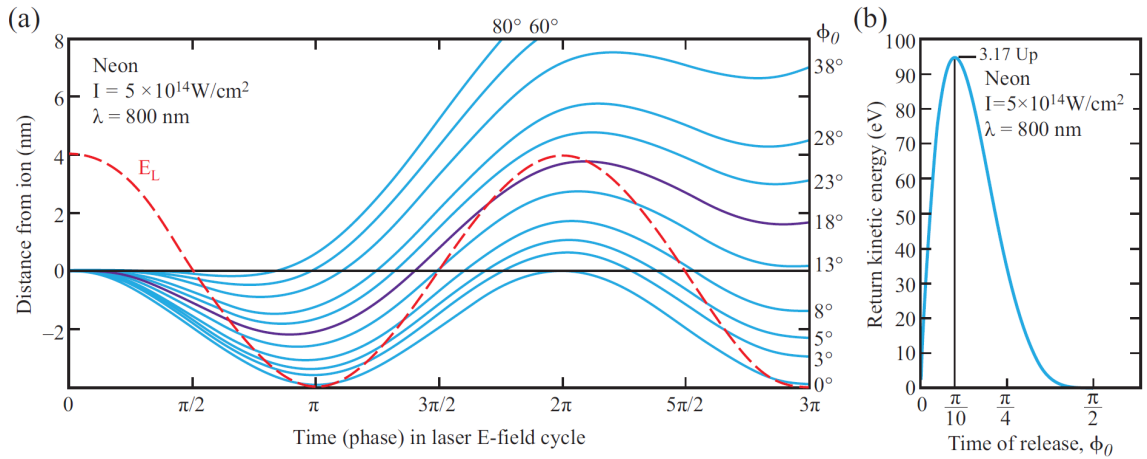


Figure 2.23: a) Electron trajectories for different initial phases (right axis), $\varphi_0 = \omega t_0$, within the cycle of the laser electric field (bottom axis). For $\varphi_0 = 0$ the electron accumulates significant kinetic energy but returns with none. For $\varphi_0 = \pi/10$, or 18° the electron returns with maximum kinetic energy. b) Kinetic energy of electrons upon return to parent ion as a function of emission time in terms of electric field phase. Electrons emitted from $\pi/2$ to $\pi$ never return and thus do not produce photons. The process repeats every half cycle identically except for the electrons propagation direction due to the reversed electric field. Taken from Attwood and Sakdinawat [2017].

corresponding to an energy of 3.17 $U_p$.

The third and last step is the radiative recombination. A photon of energy

$$E_{\text{ph}} = I_{\text{p}} + E_{\text{kin}} \tag{2.28}$$

where $E_{\text{kin}}$ is the kinetic energy of the returning electron, is produced. The efficiency of the whole HHG process is very low due to several reasons. First, the tunneling efficiency is of order $10^{-1}$ to $10^{-2}$. Then, only half of the emitted electrons will return to the parent ion due to their emission time with respect to the electric field phase as discussed earlier. But most significantly is the three dimensional divergence of the electron emission process due to quantum diffusion, amplified by long electron trajectories away from the parent ion. An example calculation by Corkum and Krausz [J2007] estimated relative cross sectional areas of order $10^{-3}$ comparing the atomic radius to the FWHM of the electron's wave packet upon return. All these effects result in HHG efficiencies of order $10^{-5}$ to $10^{-8}$ across the XUV spectrum, decreasing with frequency. There is a necessity of short drive pulses beyond achieving the intensity required to initiate HHG. Long pulses result in depletion of the ground state during previous pulse maxima. If the pulse is too long the ground state will be depleted before the peak of the pulse is reached. This leads to a "waste" of most of a pulse's intensity and an underachievement in photon energies since the highest electric field amplitudes are not used.

# 3 Experimental setup

This chapter covers the description of the experimental setup for generation of an XUV frequency comb, with focus on the compression and pulse characterization assemblies.

## 3.1 Laser

A modelocked Yb-doped fiber laser, commercially available at MenloSystems GmbH, with 14 nm bandwidth centered around 1040 nm is used. The bandwidth corresponds to a minimum pulse duration of 115 fs according to Eq. 2.6. The pulses are produced at a repetition rate of 100 Mhz locked to a 10 MHz GPS disciplined local oscillator, leading to a relative stability of $5 \cdot 10^{-13}$ in 1 s. The laser has two outputs: one, after a Yb-doped amplifier stage and a third order dispersion compressor with 10 W of average output power and a pulse duration of 180 fs which will be referred to by 'precompressed output' in the rest of this thesis. The other output bypasses the compressor, has the same power but yields pulses of 24 ps duration. The first output is used for the development of the cavity inside the vacuum chamber, while a chirped pulse amplification stage is built for the second output to reach 80 W of average power at 200 fs pulse duration.

## 3.2 Chirped pulse amplification stage

In the chirped pulse amplification stage the laser pulses of 24 ps duration at 10 W average power will be enhanced to 80 W average power at 200 fs pulse duration. The pulses are amplified in a 1 m long fused silica fiber doped with Yb, which is pumped by a 250 W average power diode laser. The pump laser light is coupled into the fiber against seed laser direction by a parabolic gold-coated mirror with a hole in its middle in order to allow the seed laser to propagate through it into the further assembly. Using a small fraction of the beam, reflected at a thin glass piece, the light emerging from the end of the amplification fiber is imaged by a camera to monitor the coupling into the fiber. Subsequent to amplification the pulses are led to a compressor. After compression the beam follows the same path as the precompressed output and leads either into the cavity or the pulse characterization assembly. This is realized with a magnetic mirror which is put in and out of place, depending on which output is currently needed. The described beam path is depicted in Fig. 3.1. In this thesis two compressor assemblies are investigated. One is a grating compressor that contains a 800 lines/mm volume phase holographic grating (Wasatch Photonics),
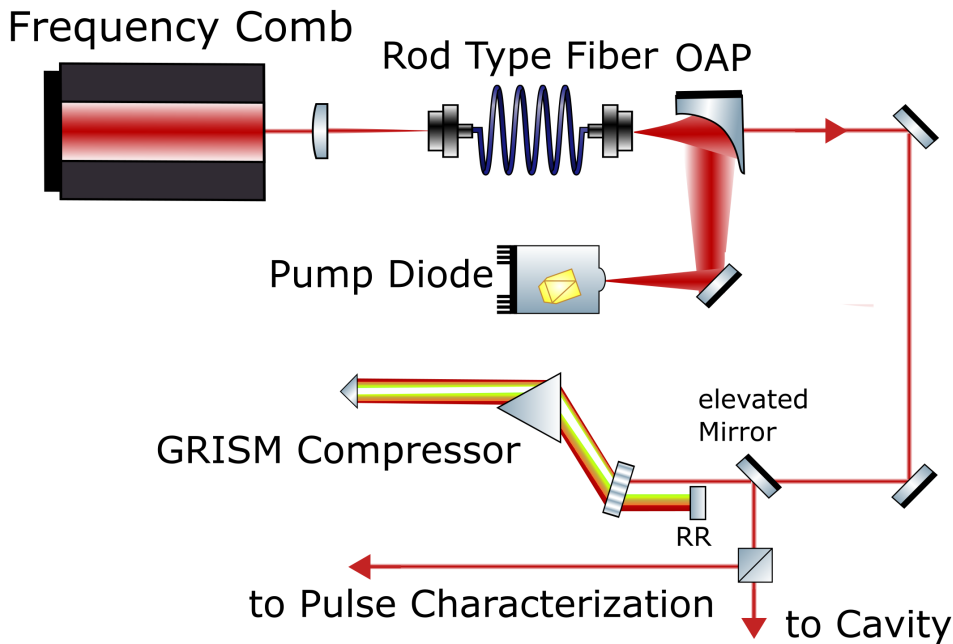
Figure 3.1: In this chirped pulse amplification stage, a 1040 nm central wavelength seed laser is amplified from 10 W to 80 W of average power in a rod-fiber, pumped by a 250 W diode laser at a wavelength of 975.7 nm. The pump light is focused into the rod-fiber by a gold coated off axis parabolic mirror, with a hole in the middle to let the amplified beam pass. In the following the 24 ps long pulses are compressed below 200 fs by a GRISM or alternatively a grating compressor, which contain two retroreflectors (RRs).

which diffracts due to modulation of the refractive index. The grating structure is enclosed by two layers of fused silica, which makes it more robust and allows for easy handling and cleaning. Using s-polarized light the grating reaches a diffraction efficiency above 95%. The whole grating compressor is expected to have an efficiency of approximately 75%. First it was mounted in a kinematic rectangular optic mount with fixed height(KM100SL from Thorlabs), which enables to tip the grating in two directions. One changes the incidence angle in the horizontal plane, the other in the vertical plane. However we discovered that the grating lines were not oriented perpendicular to the optical table surface. Thus the pointing of the beam diffracted in minus first order was altered in vertical direction compared to the undiffracted part. To compensate this the grating was rotated slightly around the perpendicular of a side that faces the beam by putting aluminum foil under one side. Later the mount was replaced by a Gimbaled three-axis optic tilt mount which covered the desired degree of freedom. Besides the grating this compressor consists of two home-built retroreflectors. These are made of two quadratic highly-reflective (HR) mirrors each. The HR mirrors are designed to operate from 1000 to 1100 nm at 45° incidence angle with a reflectivity of more than 99%. One is glued to a home-built mount, the other to a perpendicular oriented compact kinematic mount (KMS by

Thorlabs) that is connected to the home-built mount as well. The retroreflectors were aligned over a distance of approximately 2 m to ensure a 90° angle between the two mirrors. Otherwise the angular dispersion introduced by grating and/or prism cannot be canceled out as intended by fourfold propagation through these elements. Left over angular dispersion leads to undesired spatio-temporal beam distortions like a spatial chirp. For easier alignment a rail for a retroreflector and the grating was built, see Fig. 3.2. The point of incidence of the beam on the
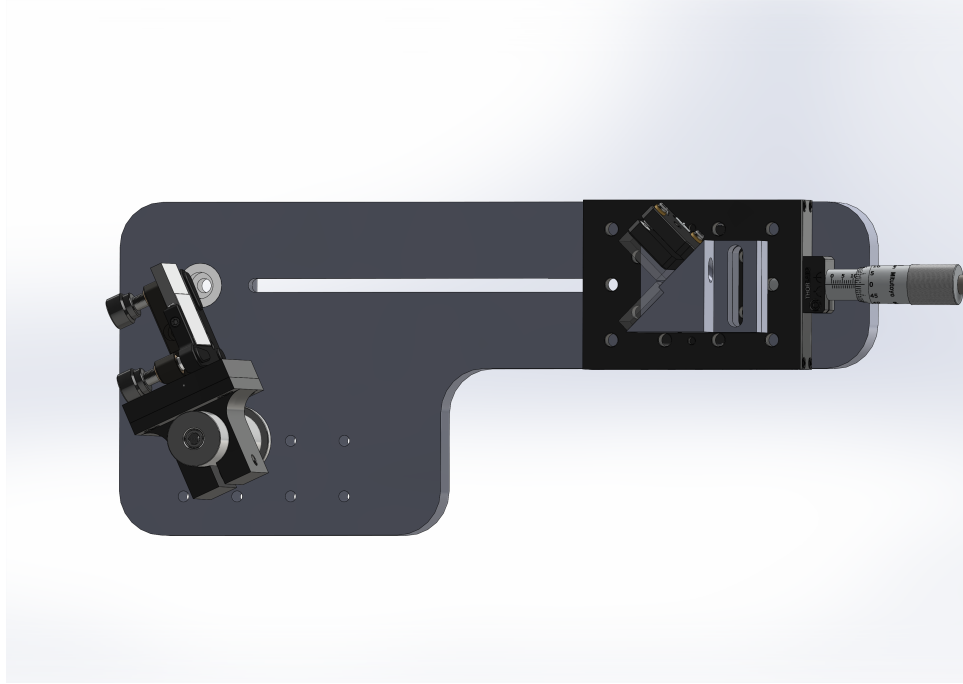


Figure 3.2: Home-built rail allows translation of the RR over a range of 30 cm. The point of incidence of the beam on the grating is located on the rotation axis of the rail which enables iterative adjustment of incidence angle on the grating and RRs for maximum transmission.

grating is located on the rotation axis of the rail. Thereby the beam pointing before the compressor can be kept unchanged during the iterative search for the optimal incidence angle on the grating. This is done by tilting the grating and subsequently adjusting the orientation of the trail iteratively, to ensure a 45° incidence angle on the retroreflector mirrors and maximal transmission of the minus first order.
The second compressor assembly uses the same components as the first one and additionally incorporates a 60 mm side length equilateral prism (EKSMA Optics), made out of SF11. This alters the beam guidance in the following way. First the light is diffracted into minus first order by the grating at a Bragg angle of 24.58°. Then, the beam is refracted twice at the prism surfaces to fan out the frequency components even more. Afterwards the two retroreflectors guide the beam three more times through the assembly to reverse the divergence of the frequency components and recollimate the beam. Due to vertical displacement in one of the retroreflectors

the beam leaves the compressor at a higher elevation. The modeled beam path is also depicted in Fig. 5.1. The prism will be operated close to Brewster angle, which requires p-polarized light, while the grating operates more efficiently with s-polarized light. Therefore a $\lambda/2$-wave plate is put in between the prism and grating. An efficiency of approximately 70% is expected. While a grating compressor can only introduce negative second order and positive third order dispersion, as mentioned in the theory chapter 2.1.3, a GRISM compressor can compensate both positive and negative GDD and TOD.

## 3.3 Cavity

After compression and amplification in the CPA stage the pulses are coupled into an in-vacuum enhancement cavity that consists of four HR mirrors and an in-coupling mirror in order to amplify them further by a factor of approximately 100. A cavity roundtrip is 3 m long, which corresponds to the spatial separation of two consecutive pulses due to the repetition rate of 100 Mhz in order to overlap incoming pulses coherently with stored pulses. The cavity length is locked by the Pound-Drever-Hall technique Black [2001] to compensate length fluctuations due to e.g. vibrations. In the cavity the beam is focused to a waist size of 15 $\mu$m by two concave HR mirrors. At the focus a HHG target gas is injected, to produce collinearly propagating high-order harmonics. The XUV pulses will be coupled out of the resonator by minus first order diffraction off of a shallow 2000 lines/mm grating structure etched into a cavity mirror. The infrared light is reflected in zeroth order, so that additional losses are minimized. Inside the vacuum chamber the cavity is mounted onto a solid rod structure, made out of titanium for low thermal expansion, low weight and high strength, which is depicted in Fig. 3.3. The rod structure is rigidly connected to the optical table, while the vacuum chamber is floating on six membrane air springs (BiAir from Bilz Vibration Technology AG). To decouple the vibrations of the turbomolecular pumps from the optics, flexible connections between the vacuum chamber and rod structure are installed. This way the large mass of the vacuum chamber acts as a low-pass filter for the vibrations and prohibits their transfer to the laser table Nauta et al. [2017].

## 3.4 FROG setup

To characterize and compare the pulses manipulated by the two compressors, a home-built SHG FROG setup is used. It consists of an autocorrelator and a spectrometer, which will be presented in the following. A schematic drawing of the FROG setup is shown in Fig. 3.4.
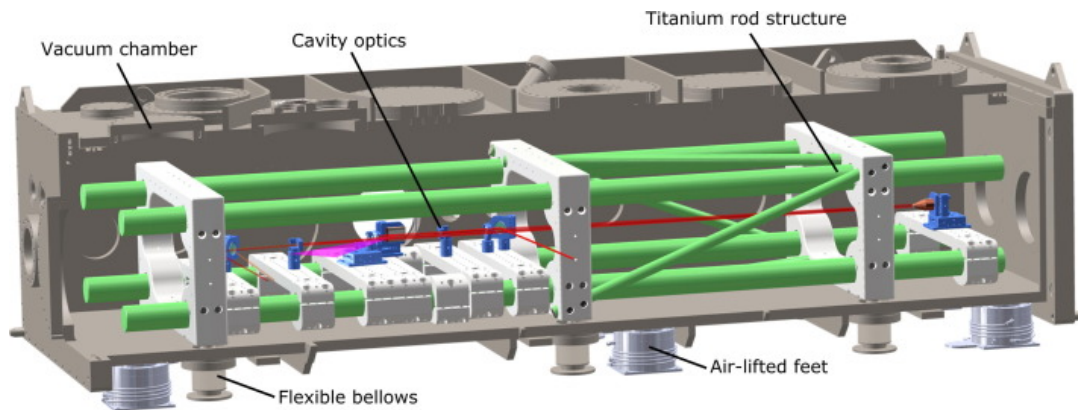
Figure 3.3: Design of the vacuum chamber (dark grey) and rod structure (green and light grey) supporting the mirrors (blue) of the enhancement cavity Nauta et al. [2017].

### 3.4.1 Autocorrelator

The laser beam path follows the red and green line in Fig. 3.4. First the beam is split into two replicas, one part passes the delay stage, inhibiting a displacement stage steered by a stepper motor, to a 10 cm focal length lens, the other part is guided on a path of similar length to that lens. The stepper motor is controlled by an Arduino, following the instructions and using the code of Campbell et al. [2014]. The beam path of the laser in the delay stage has to be perpendicular to the retroreflector prism surface to preserve it's pointing and position after retroreflection. Otherwise the FROG traces are smeared out and distorted. In the other arm a D-shaped mirror is used to facilitate a small displacement between the beams in front of the focal lens. This leads to a small crossing angle inside the SHG crystal and prevents geometrical smearing of the trace Trebino et al. [1997]. To ensure similar conditions in the measurement of FROG traces the following is done. The autocorrelator is aligned once, in the manner stated above, using the precompressed output, that has a fixed and stable beam path leading to the cavity and autocorrelator. Afterwards this alignment remains unchanged and the beam position of the precompressed output is measured at two points along its path, using either a beam profiler or cameras which observe the transmission of cavity mirrors. In the following in order to couple into the autocorrelator the path of the other output is aligned to match the saved beam positions of the precompressed output.

The SHG crystal inside the autocorrelator is made out of Beta-Barium Borate. It has a length of $100\,\mu$m to minimize the impact of group velocity mismatch, as discussed in Chapter 2.2.2. After SHG the middle beam is selected by apertures and IR light is filtered out by a 10 nm bandwidth filter centered at 520 nm. Finally, the SH light is coupled into a telecommunication single-mode fiber, which leads to the spectrometer.
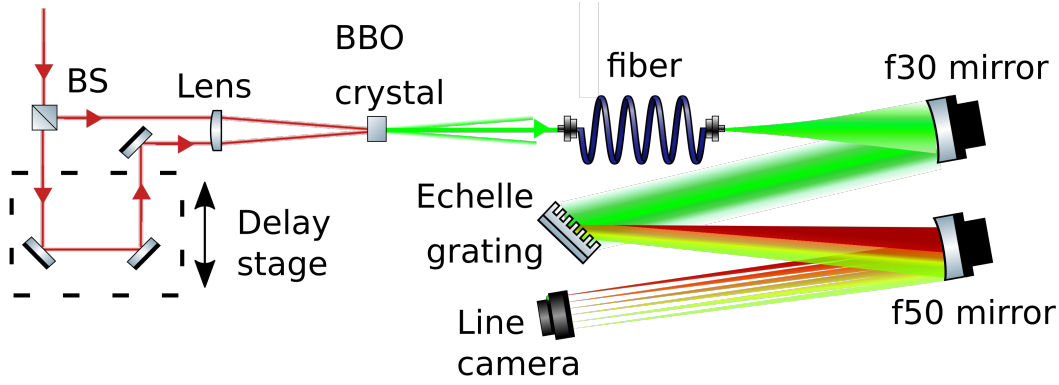
Figure 3.4: Schematic experimental setup for FROG trace measurements. The incoming infrared beam is split at the beam splitter, the split beams are delayed with respect to each other, then focused into a $100\,\mu m$ long BBO crystal, where the SH is produced. Then the resulting beam is coupled into a fiber that leads to a home-built spectrometer where it is spectrally resolved. f30 and f50 refer to the focal lengths of the focus mirrors in mm. The spread into new colors behind the grating is exaggerated to display the angular dispersion.

## 3.4.2 Spectrometer

The spectrometer consists of an $79\,\text{lines/mm}$ Echelle grating and a sensitive 2048-pixel line camera (LC100 from Thorlabs). The beam enters the spectrometer by a fiber acting as a slit. This improves the versatility, since beams from all points in the laboratory can be coupled into a fiber and therefore also into the spectrometer without requiring several additionl optics.

An Echelle grating obeys the general grating equation

$$n\lambda = d(sin(\theta) + sin(\theta')), \tag{3.1}$$

where $n$ is diffraction order, $\theta$ incidence angle, $\theta'$ diffracted angle, $d$ grating period (distance between grooves). It is characterized by a low groove density and a design to produce maximum efficiency at high diffraction orders. At these high diffraction orders angular separation is stronger

$$sin(\theta') = n\lambda/d, \tag{3.2}$$

resulting in a higher spectral resolution than in low diffraction orders. As a trade off the free spectral range

$$\lambda_{free} = \lambda_{central}/n \tag{3.3}$$

as well as the angular separation between diffraction orders are reduced. For all these properties Echelle gratings usually find application as cross dispersers behind another grating operating at the first diffraction order. Since we intend to use the

29

spectrometer mainly for spectrally resolving the second harmonic of our laser with a bandwidth of roughly 14 nm, introducing further separation between diffraction orders with a second grating is unnecessary. Hence, the Echelle grating is utilized solely. The calibration of the pixel-wavelength mapping of the spectrometer's camera is performed with a FeNe hollow cathode lamp. This lamp's spectra as well as the transmission of the bandpass filter are characterized by a second spectrometer with larger bandwidth, a Model 2062 Czerny-Turner Monochromator from McPherson Bekker et al. [2018]. The transmitted spectral lines used for calibration are three Ne I transitions. The first from $2s^22p^5(^2P^o_{3/2})3p$ to $2s^22p^5(^2P^o_{3/2})4d$ at 533.07771 nm and then two very close lines, one from $2s^22p^5(^2P^o_{3/2})3p$ to $2s^22p^5(^2P^o_{3/2})4d$ at 534.10932 nm, the other from $2s^22p^5(^2P^o_{3/2})3p$ to $2s^22p^5(^2P^o_{3/2})4d$ at 534.3282 nm. All transitions are referenced by the Line reference L3451. At the diffraction orders of highest efficiency the spectrometer covers a spectral range of approximately 12 nm corresponding to a resolution of roughly 6 pm/pixel. Consequently calibrating at highest efficiency diffraction orders leads to a spectral window on the line camera from 521 nm to 533 nm, which does not include the second harmonic spectrum of our laser. Therefore the grating has to be used at less efficient and less dispersing diffraction orders.

Fig. 3.5 shows the calibration spectrum. The two close transitions at 534.10932 nm
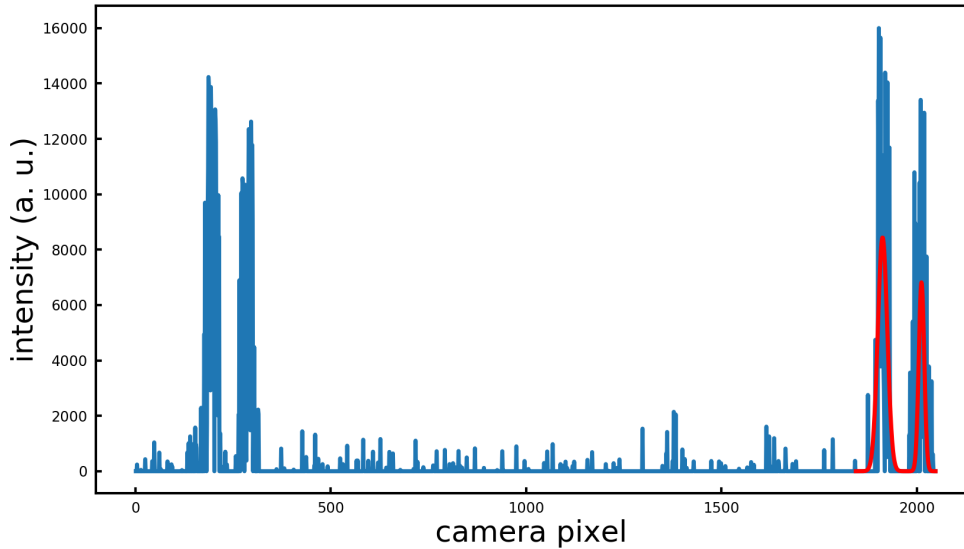


Figure 3.5: Uncalibrated spectrum of a FeNe hollow cathode lamp with a 10 nm bandpass filter at 530 nm. The two pairs of peaks are two different diffraction orders of the same three Ne I transitions at 533.0771 nm, 534.10932 nm and 534.3282 nm, of which the latter two cannot be distinguished and appear as one peak (right one). Measured in a home-built Echelle grating spectrometer.

and 534.3282 nm appear as one peak; the right one of each pair. Therefore the mid-

dle wavelength of the two was mapped to it's position at pixel 2012.16 determined by the gaussian fit in red. The same was done for the peak to the left at pixel 1912.46 and the transition at 533.07771 nm, which leads to a wavelength to pixel mapping constant, referred to as wavelength increment, of 0.011445 nm/pixel and a wavelength offset of pixel 1 of 511.1891 nm. By mistake a wrong wavelength difference between the first line and the double line was calculated previously. Initially the camera was controlled by a merchant-supplied software, called SPLICCO. While the stepper motor is controlled by python, this means that the camera measurement has to be triggered externally. However this function is unreliable and would miss many triggers, leading to incomplete FROG traces. Also it is inconvenient to use two different softwares for measurement. Therefore a example script, capable of taking scans and saving them to a .txt-file, written in the programming language C, is extended to receive parameters from python. Those parameters are the number of scans to average over, the integration time per scan and the path to the directory where the scans shall be saved. This allows to control the stepper motor and the camera using a single python program and ensures reliable measurements.

# 4 Performance of FROG phase retrieval algorithm

This chapter examines the performance of the retrieval algorithm in two different scenarios. First noise-free virtual traces are retrieved, then additive gaussian noise at different signal to noise ratios is applied to one of the previous traces. Especially the consistency of the spectral phase retrieval will be investigated in order to extract an accuracy limit for the retrieval parameters of following experimental traces.

## 4.1 Performance on noise-free virtual traces

For generation and retrieval of virtual pulses the program "FROG" Version 3.2.4 from Femtosoft Technologies, is used. For each pulse the central wavelength and bandwidth in nm and the dispersion parameters GDD and TOD in $\text{fs}^2$ and $\text{fs}^3$, respectively, are put in by the user and a trace as well as a temporal and spectral electric field are generated. Later in this thesis the dispersion of experimental pulses will be determined quantitatively. According to 2.7, the spectral phase can be described by a Taylor series, which contains the GDD and TOD as coefficients of second and third order in angular frequency, respectively. Therefore the coefficients of a polynomial fit to the spectral phase, represent the desired dispersion parameters.

First the described procedure of determining the dispersion from the spectral phase is tested on virtual pulses. The procedure will be verified by using it on virtual pulses with known properties. It was found that the third order coefficient of a third order polynomial fitted to the spectral phase matches the TOD of the pulse, but the second order coefficient does not match the GDD. Though the second order coefficient of a separate fit with a polynomial of second order yields the correct GDD. So, in the following to extract the second order dispersion a polynomial of second order is fitted to the spectral phase, while a third order polynomial is used for the third order dispersion.

The performance of this procedure was tested over a range of dispersion parameters up to $10^5\,\text{fs}^2$ of GDD and $10^7\,\text{fs}^3$ of TOD. The results are listed in Tab. 4.1.

The first generated pulse is transform-limited, i.e. GDD and TOD are zero. While the fit includes $0\,\text{fs}^2$ of GDD within $1\,\sigma$, the fitted TOD assumes a value of $2 \cdot 10^3$, which obviously differs significantly from zero. However, this amount of left over TOD does not alter the pulse duration, see pulse No .2 in 4.1, nor the FROG trace visibly, see 4.1. The same holds for pulse No. 8, the deviation of the TOD of the fit amounts to $40\,\sigma$, but this difference does not manifest in a change of pulse

Table 4.1: Results of fitting polynomials to the spectral phase of virtual noise-free pulses with 1040 nm central wavelength and 11 nm bandwidth for varying amounts of second and third order dispersion.

| No. | GDD [fs$^2$] | GDD$_{\mathrm{fit}}$ [fs$^2$] | TOD [fs$^3$] | TOD$_{\mathrm{fit}}$ [fs$^3$] | $\tau$ [fs] |
|---|---|---|---|---|---|
| 1 | 0 | $3.5 \pm 3.5$ | 0 | $(2.14 \pm 0.02) \cdot 10^3$ | 144.7 |
| 2 | 0 | $(2.6 \pm 3.3)$ | $2 \cdot 10^3$ | $(2.00 \pm 0.0002) \cdot 10^3$ | 144.7 |
| 3 | 0 | $-49 \pm 66$ | $5 \cdot 10^4$ | $(5 \pm 0.00001) \cdot 10^4$ | 149.71 |
| 4 | 500 | $500 \pm 0.006$ | 0 | $0.4 \pm 0.5$ | 146 |
| 5 | $2 \cdot 10^3$ | $(1.99 \pm 0.02) \cdot 10^3$ | 0 | $1.98 \pm 3.72$ | 163.8 |
| 6 | $5 \cdot 10^3$ | $(4.98 \pm 0.05) \cdot 10^3$ | 0 | $(6.3 \pm 9.0)$ | 240 |
| 7 | $3 \cdot 10^4$ | $(3 \pm 0.00003) \cdot 10^4$ | 0 | $8 \pm 28$ | 1160 |
| 8 | 500 | $499 \pm 1$ | $10^3$ | $(1.02 \pm 0.0005) \cdot 10^3$ | 146 |
| 9 | 500 | $497 \pm 3$ | $2 \cdot 10^3$ | $(2.00 \pm 0.00005) \cdot 10^3$ | 146 |
| 10 | $5 \cdot 10^3$ | $(-5.0 \pm 0.003) \cdot 10^3$ | $2 \cdot 10^3$ | $(2.0 \pm 0.004) \cdot 10^3$ | 240 |
| 11 | $5 \cdot 10^3$ | $(-4.87 \pm 0.2) \cdot 10^3$ | $10^5$ | $(1.0 \pm 0.00004) \cdot 10^5$ | 210 |
| 12 | $5 \cdot 10^3$ | $(4.35 \pm 0.85) \cdot 10^3$ | $5 \cdot 10^5$ | $(5.0 \pm 0.0001)$ | 216.1 |
| 13 | $10^4$ | $(9.54 \pm 0.7) \cdot 10^3$ | $5 \cdot 10^5$ | $(5 \pm 0.0008) \cdot 10^5$ | 223.2 |
| 14 | $10^4$ | $(9.5 \pm 1.0) \cdot 10^3$ | $10^6$ | $(1.0 \pm 0.00002) \cdot 10^6$ | 258.3 |
| 15 | $10^4$ | $(8.43 \pm 2.2) \cdot 10^3$ | $2 \cdot 10^6$ | $(2 \pm 0.0001) \cdot 10^6)$ | 313.2 |
| 16 | $10^4$ | $(-1 \pm 0.4) \cdot 10^4$ | $5 \cdot 10^6$ | $(5 \pm 0.0002) \cdot 10^6$ | 413.6 |
| 17 | $10^4$ | $(-1.32 \pm 0.68) \cdot 10^4$ | $10^7$ | $(1.06 \pm 0.0007) \cdot 10^7$ | 1017 |
| 18 | $5 \cdot 10^4$ | $(5.00 \pm 0.05) \cdot 10^4$ | $5 \cdot 10^5$ | $(5 \pm 0.0007) \cdot 10^5$ | 1863 |
| 19 | $8 \cdot 10^4$ | $(8.00 \pm 0.04) \cdot 10^4$ | $5 \cdot 10^5$ | $(5 \pm 0.0008) \cdot 10^5$ | 3035 |
| 20 | $10^5$ | $(1 \pm 0.004) \cdot 10^5$ | $5 \cdot 10^5$ | $(4.94 \pm 0.001) \cdot 10^5$ | 3808 |

duration or trace shape. For all other pulses, except pulses No. 18 and No. 20, the fit and start values of dispersion agree within $1\,\sigma$. For pulses up to 1 ps pulse duration retrievals are fast and converge to errors below $10^{-6}$ or even lower if the algorithm is given time to do so. For reference, retrievals of experimental traces are considered accurate at FROG errors on the order of $10^{-3}$ FRO. The first six pulses inhibit either no TOD or GDD at all and should give an overview about the orders of magnitude necessary to cause changes in pulse duration. Hundreds of fs$^2$ of GDD already widen the Temporal FWHM, while TOD alone does not alter the pulse duration at 2000 fs$^3$. Pulses 8 and 9 show that even when GDD is present, this amount of TOD does not introduce any changes. Even though theory describes that the presence of GDD should amplify the effects of TOD in the theory chapter 2.2.2. Consequently TOD on the order of $10^3\,\mathrm{fs}^3$ is negligible. Only at $5 \cdot 10^4\,\mathrm{fs}^3$ the dispersion becomes more significant and the pulse is widened by 5 fs, see pulse No. 3.

With constant GDD and increasing third order dispersion, see pulses No. 13 to 16, the relative error of GDD increases, while the third order dispersion is determined very precisely. FROG traces and spectral electric fields in Fig. 4.2 show that the
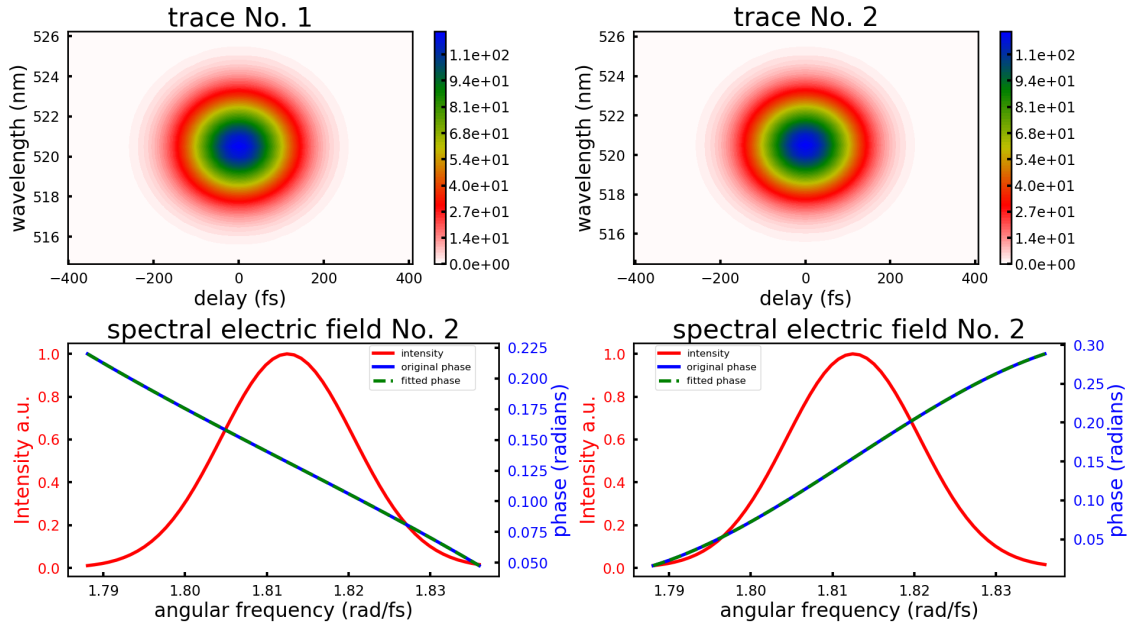
Figure 4.1: Left: Trace of a transform limited pulse. Right: Trace of a pulse without GDD but $2000\,\mathrm{fs}^3$ of TOD.
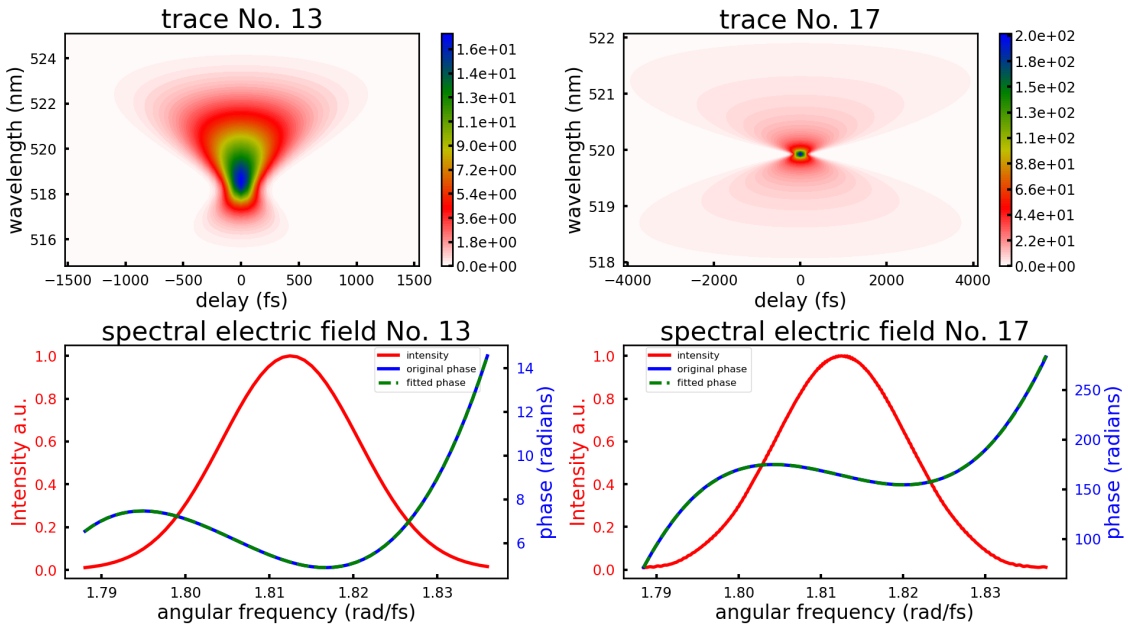


Figure 4.2: TOD dominated traces. GDD is constant at $10^4\,\mathrm{fs}^2$, while the TOD increases from $5 \cdot 10^5\,\mathrm{fs}^3$ to $\cdot 10^7\,\mathrm{fs}^3$.

TOD dominates the shape of the traces, which makes them hourglass shaped. So, the retrieval is able to accurately reconstruct the dominating orders of the spectral phase while it loses precision for the less significant orders. At least, until that re-

lationship breaks down at $10^7 \, \text{fs}^3$, in pulse No. 17. The loss of accuracy in GDD can be understood by considering that the spectral phase is dominated by its third order, while a second order polynomial is fit to it to determine the GDD.

At dispersion values resulting in pulse durations on the order of picoseconds, pulses No. 17 to 20, the traces get very big because their area is proportional to the time-bandwidth product of their corresponding pulses. Therefore a bigger grid is needed, which slows the retrieval down significantly. Also the retrieval starts to stagnate at FROG errors on the order of $10^{-4}$ or even higher for these traces.

Increasing the GDD while leaving the TOD constant, see pulses No. 18 to 20, supports the retrieval of pulses up to roughly $4 \, \text{ps}$ with errors below $10^{-5}$ before the accuracy in determining the TOD suffers. In that regime the GDD is dominant and still accurately reconstructed, just like the TOD before, when it was the dominant form of dispersion. When increasing the GDD further, around $10^6 \, \text{fs}^2$ the program runs out of memory.

In conclusion, the program is able to reconstruct the spectral phase and pulse duration of pulses from the transform-limit up to several picoseconds accurately with exceptions at high TOD to GDD ratios and pulse durations beyond $3 \, \text{ps}$. Compressed pulses in this experiment will possess smaller GDD than $5 \cdot 10^4 \, \text{fs}^2$ and $10^6 \, \text{fs}^2$ of TOD, hence the relevant range of dispersion values is covered by the algorithm.

## 4.2 Performance on virtual pulses with noise

In this section the retrieval of the spectral phase from virtual FROG traces with additive gaussian noise is investigated to determine an uncertainty based on the noise present in the experiment. Pulses are generated as before. The noise is produced according to a random gaussian distribution, where the mean corresponds to the average background power, quantified by the peak signal to average background power ratio PSNR. The peak signal is set according to the maximum intensity of the investigated trace. In contrast to the average signal to average noise power ratio SNR, the PSNR does not take areas of the trace into account that do not contain any measurable pulse signal. In other words the SNR is related to the ratio of pulse area to total trace area, while the PSNR is independent of that and thus is a more meaningful measure of the quality of the FROG trace. Furthermore, it is not necessary to align delay and frequency step sizes of grids of virtual and experimental traces to compare them in regards to noise level.

The fluctuations of the mean background, the noise, correspond to the width of the gaussian distribution, according to a chosen peak signal to standard deviation ratio PSSDR. Additionally, since around zero delay a pulse pedestal along the frequency axis is observed in actual measurements, the added mean background is increased across the whole spectral range around delay zero, to mimic this feature. To quantify the power of the pedestal the peak signal to average pedestal power ratio PSPR is used. The width of this pedestal is set equal to two times the temporal FWHM of the corresponding virtual pulse.

Pulses with 14 nm bandwidth centered around 1040 nm and dispersion values corresponding to upcoming experimental measurements are generated. Then, using the FROG program's noise subtraction tools, the traces are corrected for noise. The software offers following tools:

- full spectrum, which subtracts the average spectrum, that is calculated by taking the average at the two smallest and the two largest delays, from the trace at every time delay.

- edge, which takes an average value of every data value within two pixels of the edge of the data set on all four sides and subtracts this from every data point on the trace.

- cleanup pixels, is a filter that removes stray pixels

- extract, where the user can draw a window onto the trace that will cut out everything outside the window

Table 4.2: Comparison of noise subtraction tools regarding the retrieval of virtual pulses with additive gaussian noise at a PSNR of 100, PSSDR of 100 and PSPR of 35 and subsequent polynomial fit to the spectral phase. All parameters are averaged over 10 similar traces, differing by the randomness of the generated noise. 'Edge FS' and 'FS Edge' means that the noise removal tools edge then full spectrum or vice versa were applied before the retrieval, respectively. The first error stems from the fit, the second corresponds to the standard deviation over the 10 traces.

| parameter | theoretical | 2 Edge | 2 FS |
|---|---|---|---|
| GDD $[\text{fs}^2]$ | $1.1 \cdot 10^3$ | $(5.9 \pm 12.7 \pm 3.3) \cdot 10^2$ | $(1.4 \pm 1.3 \pm 0.9) \cdot 10^3$ |
| TOD $[\text{fs}^3]$ | $8.4 \cdot 10^5$ | $(8.8 \pm 0.1 \pm 0.2) \cdot 10^5$ | $(9.2 \pm 0.1 \pm 0.5) \cdot 10^5$ |
| $\tau$ [fs] | 236 | $231 \pm 11$ | $236 \pm 7$ |
| Bandwidth [nm] | 14.0 | $12.9 \pm 0.8$ | $13.2 \pm 0.6$ |
| FROG error | - | 0.0064 | 0.0079 |
| GDD $[\text{fs}^2]$ | $1.55 \cdot 10^4$ | $(1.1 \pm 0.1 \pm 0.1) \cdot 10^4$ | $(9.8 \pm 1.3 \pm 2.1) \cdot 10^3$ |
| TOD $[\text{fs}^3]$ | $8.3 \cdot 10^5$ | $(8.7 \pm 0.1 \pm 0.3) \cdot 10^5$ | $(8.9 \pm 0.1 \pm 0.6) \cdot 10^5$ |
| $\tau$ [fs] | 238 | $233 \pm 5$ | $237 \pm 4$ |
| Bandwidth [nm] | 13.9 | $13.1 \pm 0.4$ | $12.9 \pm 0.8$ |
| FROG error | - | 0.0079 | 0.0088 |
| GDD $[\text{fs}^2]$ | $2.9 \cdot 10^2$ | $(4.0 \pm 0.3 \pm 1.7) \cdot 10^2$ | $(5.5 \pm 0.3 \pm 1.5) \cdot 10^2$ |
| TOD $[\text{fs}^3]$ | $4.4 \cdot 10^4$ | $(1.6 \pm 0.1 \pm 1.2) \cdot 10^4$ | $(1.5 \pm 0.2 \pm 1.1) \cdot 10^4$ |
| $\tau$ [fs] | 123 | $132 \pm 10$ | $136 \pm 12$ |
| Bandwidth [nm] | 14.1 | $14.7 \pm 0.2$ | $14.1 \pm 1.3$ |
| FROG error | - | 0.0043 | 0.0049 |

Table 4.3: Comparison of noise subtraction tools regarding the retrieval of virtual pulses with additive gaussian noise at a PSNR of 100, PSSDR of 100 and PSPR of 35 and subsequent polynomial fit to the spectral phase. All parameters are averaged over 10 similar traces, differing by the randomness of the generated noise. 'Edge FS' and 'FS Edge' implies that the noise removal tools edge then full spectrum or vice versa were applied before the retrieval, respectively. The first error stems from the fit, the second corresponds to the standard deviation over the 10 traces.

| parameter | theoretical | Edge FS | FS Edge |
|---|---|---|---|
| GDD $[\mathrm{fs}^2]$ | $1.1 \cdot 10^3$ | $(9.1 \pm 12.7 \pm 6.7) \cdot 10^3$ | $(9.5 \pm 12.1 \pm 7.5) \cdot 10^3$ |
| TOD $[\mathrm{fs}^3]$ | $8.4 \cdot 10^5$ | $(8.8 \pm 0.1 \pm 0.3) \cdot 10^5$ | $(9.0 \pm 0.1 \pm 0.1) \cdot 10^5$ |
| $\tau\,[\mathrm{fs}]$ | 236 | $229 \pm 6$ | $232 \pm 7$ |
| Bandwidth $[\mathrm{nm}]$ | 14.0 | $13.0 \pm 1.0$ | $12 \pm 1.3$ |
| FROG error | - | 0.0066 | 0.0072 |
| GDD $[\mathrm{fs}^2]$ | $1.55 \cdot 10^4$ | $(1.0 \pm 0.1 \pm 0.1) \cdot 10^4$ | $(1.0 \pm 0.1 \pm 0.1) \cdot 10^4$ |
| TOD $[\mathrm{fs}^3]$ | $8.3 \cdot 10^5$ | $(8.9 \pm 0.1 \pm 0.5) \cdot 10^5$ | $(9.0 \pm 0.1 \pm 0.5) \cdot 10^5$ |
| $\tau\,[\mathrm{fs}]$ | 238 | $236 \pm 6$ | $238 \pm 5$ |
| Bandwidth $[\mathrm{nm}]$ | 13.9 | $13.1 \pm 0.6$ | $13.0 \pm 0.6$ |
| FROG error | - | 0.0078 | 0.0086 |
| GDD $[\mathrm{fs}^2]$ | $2.9 \cdot 10^2$ | $(3.7 \pm 0.3 \pm 2.0) \cdot 10^2$ | $(3.6 \pm 0.4 \pm 2.0) \cdot 10^2$ |
| TOD $[\mathrm{fs}^3]$ | $4.4 \cdot 10^4$ | $(1.3 \pm 0.1 \pm 0.7) \cdot 10^4$ | $(1.7 \pm 0.1 \pm 1.2) \cdot 10^4$ |
| $\tau\,[\mathrm{fs}]$ | 123 | $134 \pm 11$ | $132 \pm 9$ |
| Bandwidth $[\mathrm{nm}]$ | 14.1 | $14.8 \pm 0.4$ | $14.3 \pm 0.9$ |
| FROG error | - | 0.0044 | 0.0047 |

For comparison of the different noise subtraction tools and for investigation of the influence of heavy noise at different dispersion values, pulses are generated by three different sets of dispersion values but the same PSNR of 100, PSPR of 35 and PSSDR of 100. Then twice full spectrum, or twice edge, or once full spectrum and edge or vice versa are applied. Afterwards three times clean up pixels and extract are used to slice out values belonging to frequencies without signal of the pulse. Per set of dispersion values each procedure is tested on 10 traces that differ by the randomness of the noise. The averaged retrieval and fit parameters are displayed in Tab. 4.2 and 4.3. An example trace is depicted in Fig. 4.3. For the first dispersion set fit errors of the GDD are on the order of the mean value, which makes these values meaningless. However the GDD is so low that it would not make a significant difference in pulse duration, if it were actually zero instead. Therefore it makes sense that the algorithm struggles to retrieve it accurately. For the second dispersion set all procedures fail and underestimate the GDD by approximately $0.5 \cdot 10^4\,\mathrm{fs}^2$, which corresponds to 50% or approximately $5\,\sigma$. The big uncertainties show that the fit of a second order polynomial to a third order dominated spectral phase that is distorted by noise can give only a rough estimate of the present GDD. On the other hand, for the third dispersion set the GDD is overestimated. The standard deviation here amounts

to up to approximately 54% of the mean value, which implies that the values are scattered heavily.

The algorithm fails to determine the small amount of left over GDD in the presence of this much noise.

For the first and second set of dispersion values all background subtraction procedures and subsequent retrievals lead to an overestimation of the TOD by roughly 5% to 10%. For the third dispersion value set the results of the TOD are similar to the GDD results. A standard deviation between 54% and 75% indicate that the correct TOD value is obscured by the present noise for the retrieval algorithm.

In sets one and two the bandwidth is underestimated independently of the procedure by approximately 1 nm except for FS Edge of the first set where it differs by even 2 nm and are scattered by similar amounts around this mean value. In the third set the bandwidth are overestimated when edge is used first (or twice) by up to 0.6 nm, when full spectrum is used first (or twice) the mean bandwidth is accurate but less precise and fluctuates by more than 1 nm according to the standard deviation.

The pulse duration agrees within $1.2\,\sigma$ with the theoretical value for all procedures applied to all three sets. However the pulse duration reconstruction is least precise in the third set, close to the transform limit.

To summarize, at the transform limit the algorithm fails to precisely retrieve dispersion values in the presence of strong noise. It tends to overestimate GDD and underestimate TOD. In the first dispersion set the GDD cannot be predicted accurately, but has nearly no influence compared to the TOD, which is overestimated. In the second set the GDD uncertainties are small even though the mean values deviate by approximately 50%, however the difference on the pulse duration is small. The TOD is overestimated in a similar manner as before.

Regarding the noise subtraction procedures, in general the average dispersion values of either of the FS and Edge combinations tend to be more accurate than using one tool twice. However, the difference could stem from the nature of the simulated noise and the behavior may differ for pulses containing actual experimental noise and other distortions. Consequently none of the tested combinations seems to outperform the others. Hence, the choice of the subtraction tool to be applied, will be based on each experimental trace individually.

# 4.3 Determination of spectral phase uncertainty in the experiment

In this section the process of extracting the various noise parameters of the previous section from experimental traces will be explained. Then the composition of the resulting spectral phase uncertainty will be described.

Utilizing the FROG program raw experimental traces, without the application of any noise subtraction tools, are put onto a grid. Then the traces, where the background and noise was removed, are subtracted from the raw traces, to yield the

experimental background signal. Since the spectral range of the camera exceeds the spectral FWHM of the pulses and usually bigger delay ranges than needed were chosen to gather the whole trace, 'extract' is used on all experimental traces to cut out edges without pulse signal. Therefore the full noise and no signal should be contained in these edges. Subsequently the standard deviation of the intensity located in these edges is taken to calculate the PSSDR.

The average noise power of the PSNR is calculated by averaging over the experimental background signal. Lastly, the average pedestal power is calculated by averaging over values of the first ten frequency rows at the top of a trace that correspond to either delay zero or one delay step further in both directions.

After determination of the noise parameters a virtual trace is generated according to the reconstructed dispersion values of the measured trace. Then the noise is produced with the aid of the noise parameters and added to the virtual trace, as previously done in Fig. 4.3. Subsequently ten noisy traces are constructed and retrieved. The difference between the mean dispersion values from virtual traces and those of the measured trace is treated as a one sided systematical error. To this error the fit uncertainties of the experimental and virtual trace will be added as follows

$$\mathrm{Er_{sys,\pm}} = \sqrt{(\mathrm{Er_{fit,theo}^2 + Er_{fit,exp}^2 + Er_{exp,theo}^2})} \tag{4.1}$$

or

$$\mathrm{Er_{sys,\mp}} = \sqrt{(\mathrm{Er_{fit,theo}^2 + Er_{fit,exp}^2}}, \tag{4.2}$$

where $\mathrm{Er_{fit,theo}}$ is the averaged error of fits to virtual retrieved spectral electric fields with noise, $\mathrm{Er_{fit,exp}}$ is the error of the fit to the spectral electric field retrieved from experimental data and $\mathrm{Er_{exp,theo}}$ is the difference between the virtual mean dispersion parameter and the one reconstructed from experimental data. If the virtual mean dispersion parameter is the larger one of both the virtual traces suggest that due to noise the dispersion parameter will be overestimated in the experiment. This indicates that the true value is smaller than the measured one. Therefore, the negative systematic error will be calculated according to Eq. 4.1 and contain $\mathrm{Er_{exp,theo}}$ to represent this. Consequently, The positive systematic error is calculated by Eq. 4.2.

The standard deviation of the dispersion parameters of the ten virtual pulses will be handled separately as statistical error.
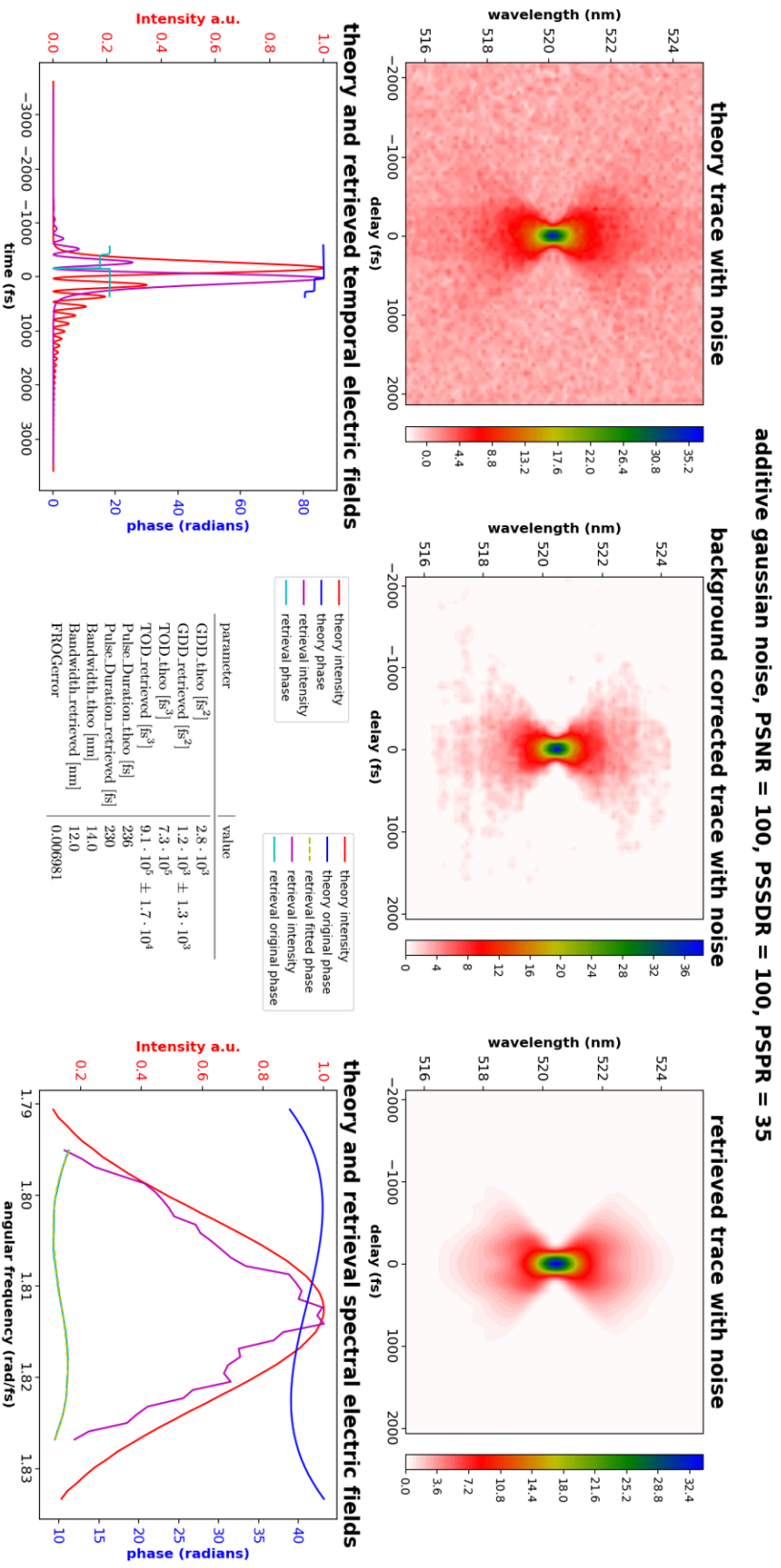
Figure 4.3: Example of retrieval of virtual trace with with heavy additive gaussian noise at a peak signal to standard deviation ratio of 100. Experimental noise is mimicked by a stripe of increased intensity at zero delay stretching over the whole spectral range.

# 5 GRISM compressor

This chapter gives an overview of the modeling, building and commissioning of a compressor, consisting of a prism, a grating and two retroreflectors (RRs), referred to as GRISM. First a ray tracing model will be introduced to describe the dispersive behavior and to find a set of parameters capable of compensating the dispersion present in the laser pulses. Afterwards the performance of the compressor in practice will be investigated.

## 5.1 Ray tracing model

A ray tracing model, written in Mathematica, which calculates the optical path length as a function of frequency, is used to find an alignment of the compressor components for dispersion compensation. By propagation through 60 m of fused silica fiber during generation of the seed laser it was estimated that a GDD of $+1.77 \cdot 10^6 \, \text{fs}^2$ and a TOD of $+2.86 \cdot 10^6 \text{fs}^3$ of is present in the pulses.

The model has 11 free parameters to describe the position of all components. The point of incidence on the grating is set as the reference point, the grating plane is set as the reference plane for angles. The position of the prism is determined by four parameters. These are $x_{\text{apex}}$ and $y_{\text{apex}}$, which represent the position of the prisms' apex point, $\alpha$ the apex angle and $\beta$ the angle of the prism surface facing the grating relative to the grating plane, as shown in Fig. 5.1. Both RRs are represented by two crossing lines, acting as mirrors. They are described by three parameters, $x_{\text{rr}}$ and $y_{\text{rr}}$ determine the position of the mentioned crossing point, while $\gamma$ describes the angle between the RR and the gratings' perpendicular. These are the parameters of the first RR, the parameters of the second RR are omitted. Between the grating and the second RR all frequency components propagate parallel to each other, thus the distance traveled does not affect the dispersion. The angle of the second RR is set to retroreflect the incoming beam. The grating position is fixed, since it is a reference point, however its grating constant $g$ is variable. The incidence angle of the laser beam on the grating $\theta_{\text{g,i}}$ is derived from the grating constant by Bragg's law to ensure optimal diffraction efficiency into the minus first order. The beam path is calculated starting from the point of incidence on the grating. The grating equation 2.11 and Snell's law of refraction are utilized to determine the direction of the beam and then it's next crossing point with a component surface. All parameters and intersections of the beam path with component surfaces are depicted in Fig. 5.1. First the beam is diffracted by the grating, then refracted twice at the prism surfaces and fanned out further by material dispersion inside the prism. Then it is reflected back by the first RR for a second transit, with a horizontal shift, to compensate the previously

introduced angular dispersion of the beam. After a second transit of the grating all frequency components travel in parallel and are guided back into the assembly with a vertical shift by the second RR. After grating and prism are passed four times in total and the beam is collimated again, the beam leaves the compressor due to the vertical shift. A deeper insight into the model is given in Ackermann [2017]. In that work, simpler versions of the model were compared to theoretical formulas of grating and prism pair compressors and were found to be correct.

To extract the dispersion introduced by the compressor the optical path length is calculated by

$$L_{\text{opt}} = \sqrt{x_B^2 + y_B^2} + \sqrt{(x_C - x_B)^2 + (y_C - y_B)^2} n_P + ... + \sqrt{(x_H - x_G)^2 + (y_H - y_G)^2}, \tag{5.1}$$

where $x_i$ and $y_i$, $i$ ranging from A to I, are coordinates of the points in figure 5.1. Then the grating phase shift B. Treacy [1969] is added to determine the total phase shift acquired in the compressor

$$\phi_K(\omega) = \frac{\omega}{c} L_{\text{opt}} - 4\pi g \sqrt{x_H^2 + y_H^2}, \tag{5.2}$$

where $c$ is the speed of light. The refractive index of the prism material is modeled by the Sellmeier equation

$$n_P = 1 + \frac{B_1 \lambda^2}{\lambda^2 - C_1} + \frac{B_2 \lambda^2}{\lambda^2 - C_2} + \frac{B_3 \lambda^2}{\lambda^2 - C_3}, \tag{5.3}$$

that includes material specific coefficients $B_1$, $B_2$, $B_3$, $C_1$, $C_2$, $C_3$. The k-th derivative yields the k-th order of dispersion as explained in Chapter 2.1.2. The parameters found to compensate the dispersion are listed in Tab. 5.2. The choice of components is determined by the parameters found to compensate the dispersion. The prism is an equilateral SF10 prism of 60 mm side length, to provide enough material dispersion while it is ensured that the beam coming into the compressor and the beam at the second RR are separated sufficiently to not lose any parts of the beam. Since the prism will be operated at 56.6°, which is closely below the Brewster angle of 60.3°, at the prism side facing RR1, the losses amount to less than 0.2%. Therefore it is unnecessary to apply an anti-reflective coating on this prism side. On the other side the beam will be incident at 66.8°, where the surfaces' reflectivity rises amounts to approximately 1.1%. Consequently one side of the prism is coated. The optimal parameters suggest a 800 lines/mm grating with a length of at least 1.2 cm, according to the distance between the passages of the beam. Furthermore, RRs are required that enable 1.69 cm of displacement, which corresponds to a side length of at least 1.2 cm.
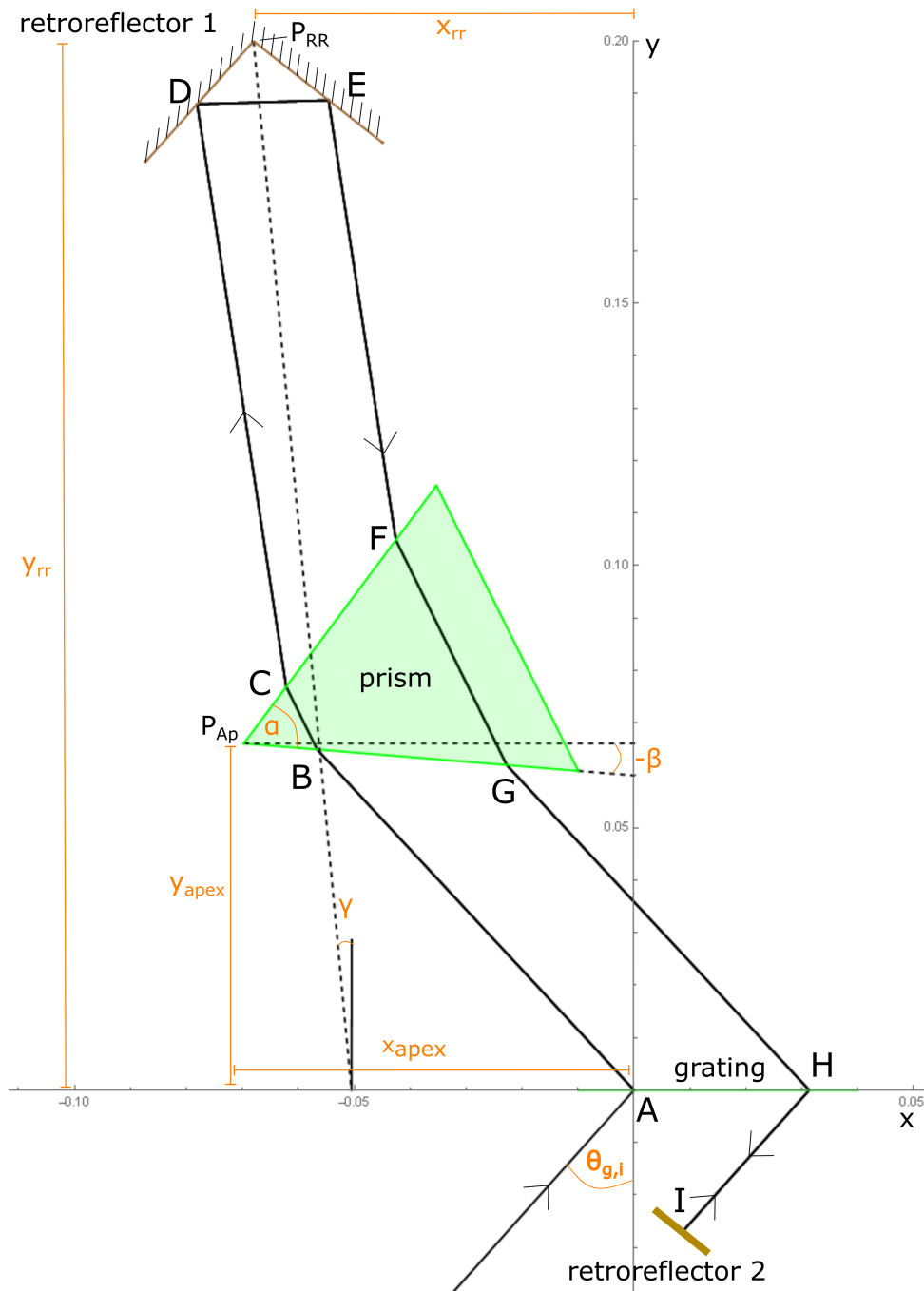
Figure 5.1: The beam path through the GRISM compressor follows points A to I. At I the beam is reflected in RR 2 to traverse the assembly again. Free parameters of the model (orange): $\theta_{g,i}$ incident angle on the grating, $\beta$ prism-grating angle, $x_{apex}$ and $y_{apex}$ are x and y coordinates of the apex point $P_{Ap}$, $\alpha$ is the prism's apex angle, $\gamma$ is the angle between RR 1 and the grating, $x_{RR}$ and $y_{RR}$ are x and y coordinates of $P_{RR}$

Figure 5.2: Set of parameters compensating the estimated dispersion parameters and Sellmeier coefficients of SF11-prism.

| free parameters | | SF11-sellmeier coefficients | |
|---|---|---|---|
| g [lines/mm] | 800 | $B_1$ | 1.62153902 |
| $\theta_{\mathrm{g,i}}$ [°] | 24.58 | $B_2$ | 0.256287842 |
| $x_{\mathrm{apex}}$ [cm] | -4.59 | $B_3$ | 1.64447552 |
| $y_{\mathrm{apex}}$ [cm] | 8.09 | $C_1$ | $0.0122241457 \cdot 10^{-12}$ |
| $\alpha$ [°] | 60 | $C_2$ | $0.0595736775 \cdot 10^{-12}$ |
| $\beta$ [°] | -42.3 | $C_3$ | $147.468793 \cdot 10^{-12}$ |
| $y_{\mathrm{RR}}$ [cm] | 18.20 | | |
| $x_{\mathrm{RR}}$ [cm] | 6.20 | | |

## 5.2 Performance measurements

This section provides information about the compression performance of the modeled GRISM compressor, which is examined utilizing the FROG setup described in Chapter 3.4. Also beam profiles and transmission efficiency will be examined.

### 5.2.1 Compression

Before investigating the compression performance, the feedback signal used while aligning the compressor is shortly reviewed. In order to find a compressor alignment for optimal compression the SHG signal of both autocorrelator arms is used as a feedback signal. The SHG yield is proportional to the intensity of the laser. Compression of the pulses does not affect the average laser intensity but the peak intensity is increased. This increases the SHG yield due to its nonlinear nature, which makes it a suitable feedback signal. In contrast to using the autocorrelation this method is practically insensitive to beam path changes behind the compressor which may arise from movement of the optical elements inside the compressor. Also it is faster than waiting for the stepper motor to scan over the pulse to measure an autocorrelation. Since SHG is intensity dependent it's signal will drop if the transmission of the compressor drops as well. This is of course undesired for sole compression purposes, because the alignment for perfect compression may lie in a parameter range of suboptimal transmission and will not be found this way. But, since the goal is to compress the pulses at the highest possible power, this is actually a useful characteristic.

First, the compressor was aligned according to the found parameters in Tab. 5.2. But maximum compression was not achieved in this configuration. Changing mainly the prism angle $\beta$ leads to an autocorrelation pulse duration of 240 fs at $I_{\mathrm{comb}} = 6\,A$. In the same configuration at $I_{\mathrm{comb}} = 6\,A$ and $I_{\mathrm{amp}} = 10\,A$ the minimum pulse duration achieved was 330 fs. Due to the change of the prism angle $\beta$, the laser was no longer incident at Brewster angle which caused the transmission to decrease. Apparently, the given dispersion values that the compressor was designed for were

not correct. This will be investigated further in the next chapter about the grating compressor.

With the use of a custom-made rail, presented in Chapter 3.2, which allows to change the position of the first RR by up to 25 cm along a chosen direction, and the prism operated at Brewster angle, different compressor arrangements are found, that compress the pulses while also providing a high transmission of approximately 70%.

Using only the seed laser, not pumping the rod-fiber, at an input power of 9.55 W to the compressor the trace in Fig. 5.3 was measured over 119 5 $\mu$m long delay steps each corresponding to 33.33 fs in time delay. The retrieval algorithm only appends a phase value to points above a threshold intensity of 0.01%. The dip in temporal phase is caused by this.
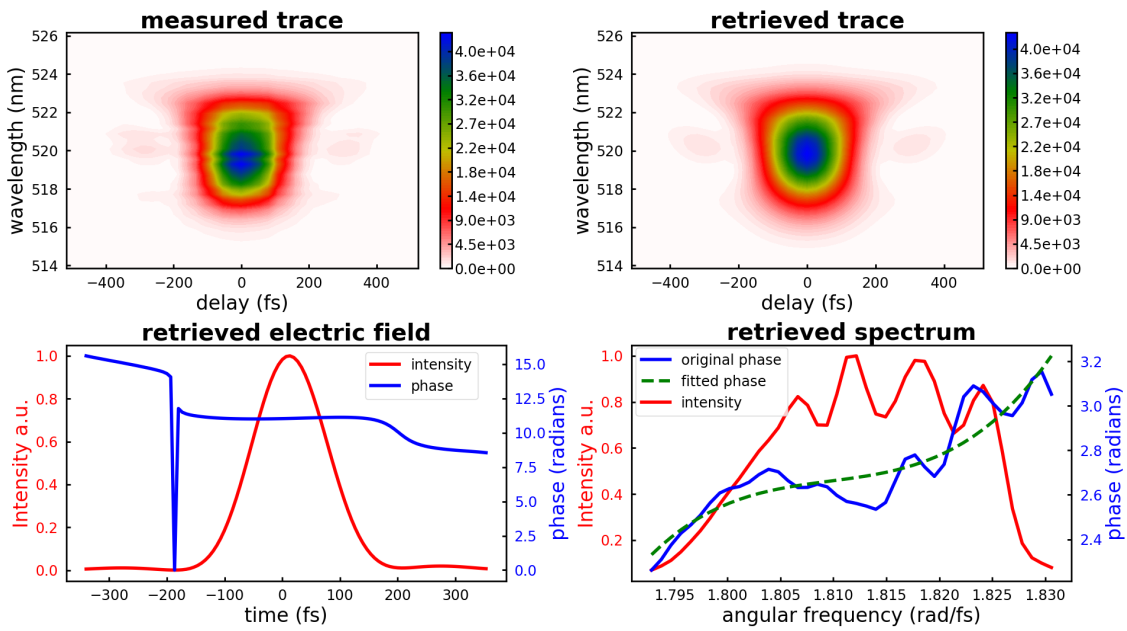


Figure 5.3: Retrieval of 150 fs temporal FWHM pulses compressed by a GRISM compressor at 6.4 W transmitted power. The spectral electric field has a 3rd order polynomial fit to the spectral phase at points corresponding to 6% of the maximum intensity.

The retrieved parameters are listed in Tab. 5.1.

Table 5.1: Results of retrieval and subsequent polynomial fit to the spectral phase of GRISM compressed pulses at 6.4 W, see Fig. 5.3. $\tau$: pulse duration, BW: bandwidth as spectral FWHM.

| GDD$_{\text{fit}}$ [$10^2$ fs$^2$] | TOD$_{\text{fit}}$ [$10^4$ fs$^3$] | $\tau$ [fs] | BW [nm] | FROG error |
|---|---|---|---|---|
| $(2.9 + 2.0 - 1.6 \pm 1)$ | $(4.8 + 2.1 - 1.3 \pm 0.6)$ | 150 | 14.2 | 0.00717 |

For comparison a trace of the precompressed output was measured and is depicted in Fig. 5.4. The retrieved parameters are listed in Tab. 5.2 and the error budget as well as noise parameters are listed in Appendix Fig. A.5. For the fit to the spectral phase an intensity threshold value of 10% is used in the rest of this thesis if not stated otherwise. This means only spectral phase points corresponding to an intensity of at least 10% of the maximum intensity are considered during the fit. Comparing
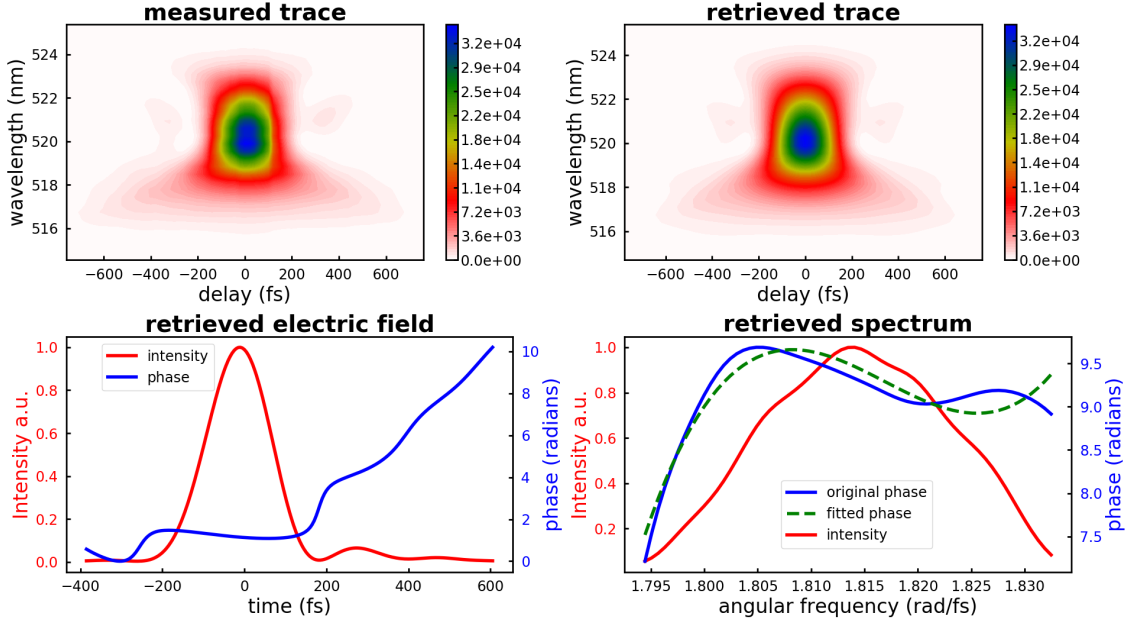


Figure 5.4: Retrieval of 180 fs temporal FWHM pulses of the seed laser at 10.3 W. The spectral electric field has a 3rd order polynomial fit to the spectral phase at points corresponding to 6% of the maximum intensity.

Table 5.2: Results of retrieval and subsequent polynomial fit to the spectral phase of pulses from the precompressed output at 10.3 W in Fig. 5.4. $\tau$: pulse duration, BW: bandwidth as spectral FWHM.

| $GDD_{fit}$ [$10^3$ fs$^2$] | $TOD_{fit}$ [$10^5$ fs$^3$] | $\tau$ [fs] | BW [nm] | FROG error |
|---|---|---|---|---|
| $(-2.9 + 0.6 - 0.5 \pm 0.02)$ | $(2.8 + 0.2 - 0.2 \pm 0.01$ | 181 | 13.4 | 0.00477 |

the retrieved parameters, it is evident that the GRISM compressor achieves a better compression of the pulses than the precompressed output at this power. Both GDD and TOD are compensated by one order of magnitude further. The asymmetry of the error indicates that the retrieval of theoretical pulses with a similar noise and dispersion as the measured ones, in this case, underestimated the dispersion values. This suggests that the present noise worsened the retrieval performance. Furthermore, the relative uncertainty of the GDD and TOD is much higher compared to the precompressed retrieval. This is caused by the non-polynomial behavior of the

46

retrieved spectral phase and the accordingly poor fit. Thus the dispersion values are not accurate and can only give a rough estimate in this case. Using these boundary dispersion values to generate pulses from theory yields traces that look similar to the measured trace but the pulses have a shorter temporal FWHM of 120.8 to 128.4 fs. To check if 4th order dispersion (FOD) may be the cause of this discrepancy, a fourth order polynomial is fitted to the spectral phase. The FOD was found to be $2 \cdot 10^4 \, \mathrm{fs}^4$. Adding this amount of FOD in the pulse generation did not influence the pulse duration at all nor did the shape of the trace change visibly, see Appendix Fig. A.1. Since the algorithm is accurate if the spectral phase follows a well-defined polynomial behavior, see Chapter 4.1, the discrepancy must stem from other phase distortions maybe linked to propagation through the not pumped rod-fiber or the compressor or noise. For comparison, plugging the reconstructed dispersion parameters of the precompressed pulses into the pulse generator, yields the trace in the Appendix Fig. A.2, that has a temporal FWHM of 175.4 fs, which is much closer to the retrieved trace's temporal FWHM compared to the GRISM compressed case. Also the retrieved spectrum is much smoother. All this together suggests that either the rod-fiber or the GRISM compressor causes additional non-polynomial spectral phase distortions. The wings at the bottom of this trace and at the top of the GRISM compressed trace are often encountered in pulse compression and point to imperfect pulse compression, according to DeLong et al. [1994b]. They cause the small satellite pulses visible in the retrieved temporal electric fields. At an input average power of 41.5 W and transmitted power of 30 W a FROG trace is measured over 60 delay steps of 4 $\mu$m length each, which is equal to 26.67 fs time delay per step. The trace and retrieved electric fields are presented in Fig. 5.5. The reconstructed

Table 5.3: Retrieval parameters of Fig. 5.5.

| GDD$_{\mathrm{fit}}$ [$10^3 \, \mathrm{fs}^2$] | TOD$_{\mathrm{fit}}$ [$10^5 \, \mathrm{fs}^3$] | $\tau$ [fs] | BW [nm] | FROG error |
|---|---|---|---|---|
| $(4.8 \pm 0.3 \pm 0.02)$ | $1.0 \pm 0.3 \pm 0.01$ | 192 | 11.5 | 0.00661 |

parameters are listed in Tab. 5.3, the error budget and noise parameters are shown in the Appendix Fig. A.4. Compared to its counterpart at lower power the trace is wider in time and the flair-out at high and low frequencies, caused by TOD is much more pronounced. Both observations are confirmed by the reconstructed dispersion values in Tab. 5.3. Compared to the low power trace the GDD is 20 times higher and the TOD is doubled at high power. Therefore the pulses are 40 fs longer in time. Besides, the spectral FWHM is 2.5 nm smaller than at low power. This is at least partially caused by gain narrowing in the amplification fiber. Due to a limited gain bandwidth of the gain medium, the center of a broad optical spectrum is amplified stronger than its spectral wings, which results in a narrower laser spectrum Diels and Rudolph [1996].
A problem of the optimization of the SHG yield in order to compress the pulses is the potential to be stuck in a local minimum of pulse duration. The pulse duration at a constant value of GDD may be lowered by introducing more TOD, which can
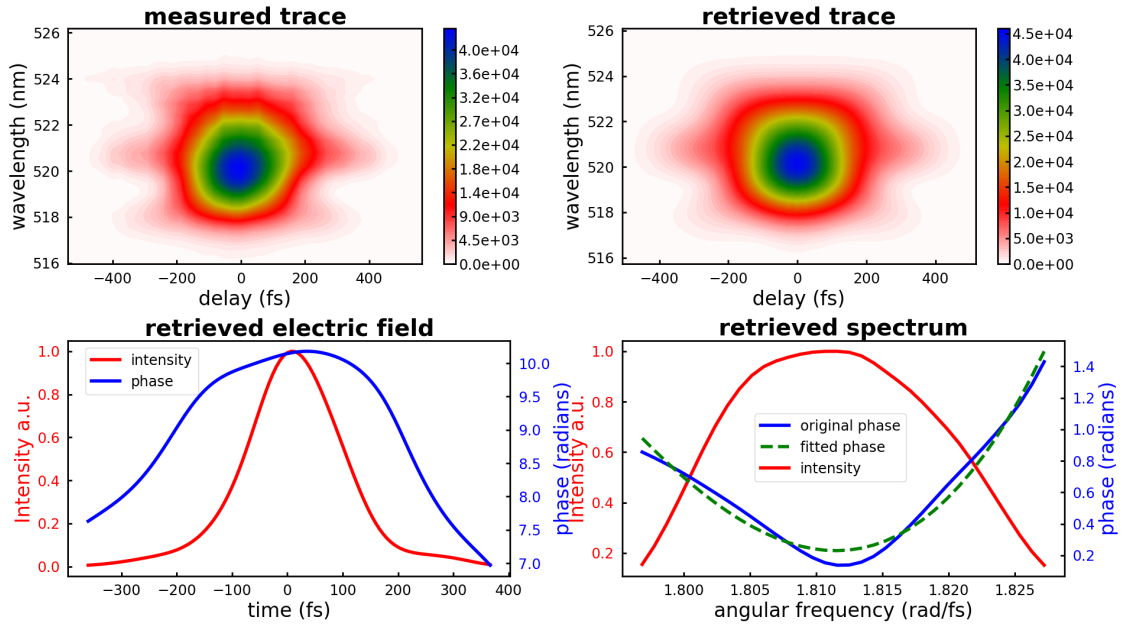
Figure 5.5: Retrieval of 192 fs temporal FWHM pulses of the amplified seed laser at a transmitted average power of 30 W. A 3rd order polynomial fit is carried out on the phase of the retrieved spectrum.

be observed in the previous Chapter 4.1 Tab. 4.1. From pulse No. 9 to No. 10 the TOD is increased by two orders of magnitude, while the GDD is kept constant at $5 \cdot 10^3 \, \text{fs}^2$. At the same time, the pulse duration drops from 240 fs to 210 fs. The same can happen in a GRISM compressor because the ratio of TOD over GDD can be manipulated freely. Coincidentally the reconstructed dispersion values of this trace are on the order of the dispersion values used for the example.

Due to the numerous free variables in a GRISM compressor, which generate a vast parameter space and the just highlighted local minima of pulse duration, a more sophisticated feedback signal than the SHG yield is required. A possible solution is a single shot version of FROG. Single shot FROG would allow to see the effects of moving elements in the compressor in real time with the aid of a trace. That way it would be evident immediately how the dispersion is manipulated by changing one of the free parameters. Hence, the TOD can be eliminated first and subsequently the GDD. If some of the TOD is reintroduced in the process of minimizing the GDD, its effect would be magnified by the present GDD, as mentioned in Chapter 2.2.2.

Due to severe distortions in the beam profile, which will be discussed in 5.2.2, no trace was measured at full power.

## 5.2.2 Beam profiles

The following spatial beam profiles are measured with a scanning-slit optical beam profiler (BP209-VIS from Thorlabs). All cross sections are measured roughly 3 m

(a) Position A         (b) Position B
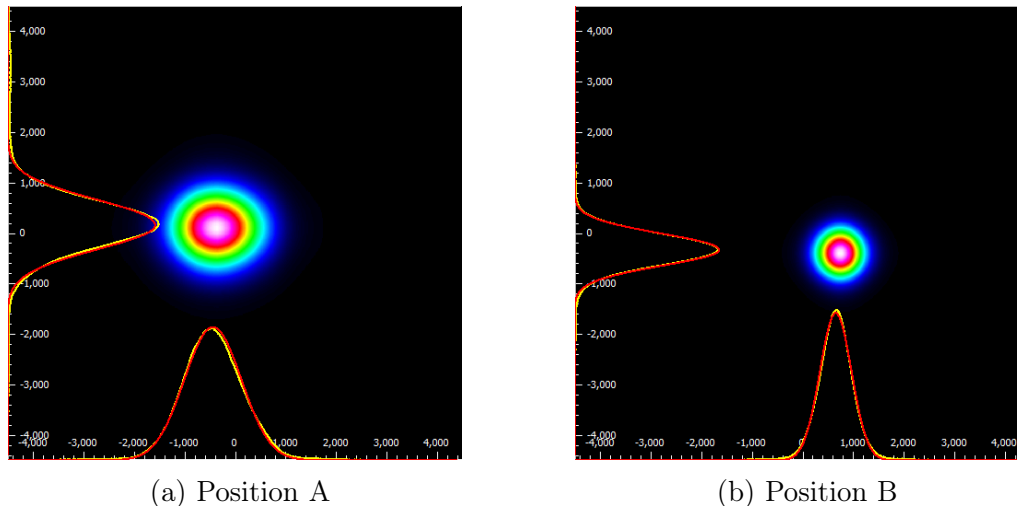
Figure 5.6: Twodimensional beam profiles behind GRISM compressor at 6.4 W transmitted power. Spatial intensity profile in x- and y-direction in yellow, gaussian fit in red

behind the GRISM compressor at two positions, A and B, 80.5 cm apart. Profiles measured at position A are closer to the compressor. The measured profiles are depicted in Fig. 5.6, Fig. 5.7 and Fig. 5.8.

Clearly, with increasing power the beam profiles at A broaden in x-direction to the point at 57 W, where the profile is shaped like an ellipse with a very long major axis, see Fig. 5.8. Simultaneously the beam profile at B is diamond shaped at 30 W and becomes slightly asymmetric at 57 W. At both positions at 57 W the profile has a trailing end to the left in x-direction. This feature can be manipulated by translating the prism. The intensity could be moved inside the profile, i.e. its peak was shifted to the right or left. Also these shifts diminished over time, but the profile never went back to its prior shape, unless the old prism position was assumed. This suggests a thermal origin of the observed behavior. Similar behavior cannot be observed for the grating, due to it's fixed mount. It is not possible to change its position while operating the laser at high power. The profiles in Fig. 5.6 and Fig. 5.7 correspond to the traces Fig. 5.3 and 5.5, respectively. Due to the wide beam profile high losses would arise in the cavity, therefore no trace was measured at the highest power using the GRISM.

The divergence of the beam over the translation range of 805 mm of the beam profiler was also measured, to complement the beam profiles with quantitative data. As a reference, the precompressed output at 10 W is convergent with an angle of 0.02° in x-direction and 0° in y-direction. The output passing the CPA stage starts with a convergence of 0.03° in x-direction and 0.02° in y-direction at 6.4 W of transmitted power. When increasing the transmitted average power to 30 W, the convergence rises to 0.09° in x-direction and stays at 0.02° in y-direction. At full power the convergence reaches 0.14° in x-direction and still remains constant in y-direction.
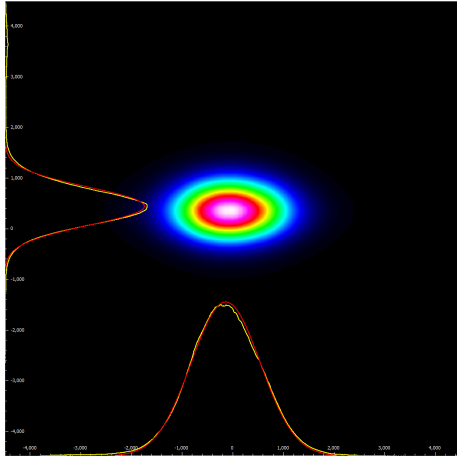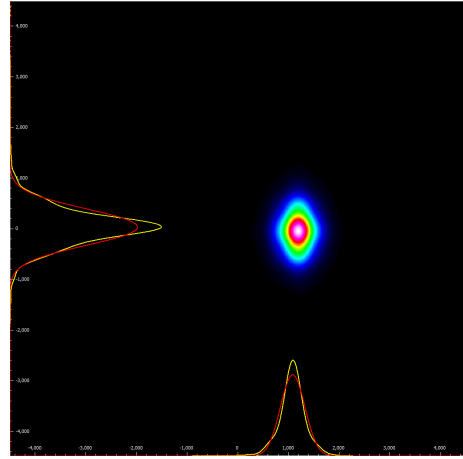
(a) Position A       (b) Position B

Figure 5.7: Two dimensional beam profiles behind GRISM compressor at 30 W transmitted power. Spatial intensity profile in x- and y-direction in yellow, gaussian fit in red.
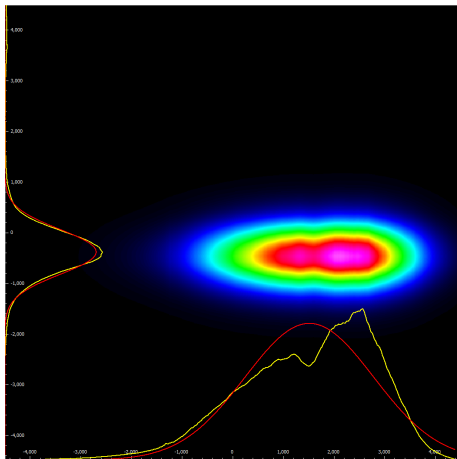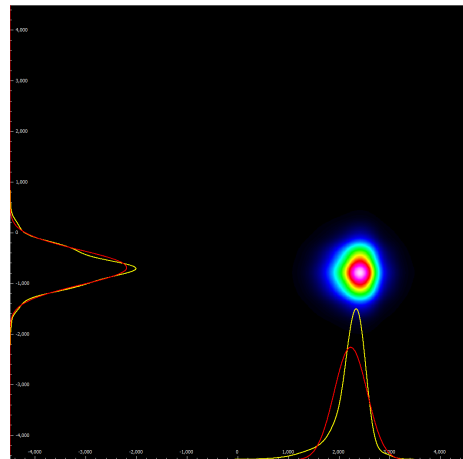


(a) Position A       (b) Position B

Figure 5.8: Two dimensional beam profiles behind GRISM compressor at 57 W transmitted power. Spatial intensity profile in x- and y-direction in yellow, gaussian fit in red.
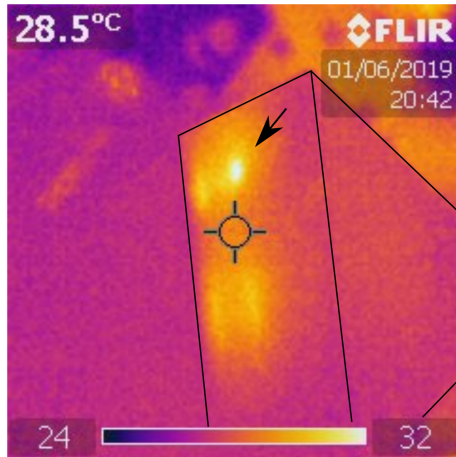
(a) prism: the bright spots show the passages of the beam. Maximal temperature of 32°C reached at last passage (arrow) before leaving the compressor.
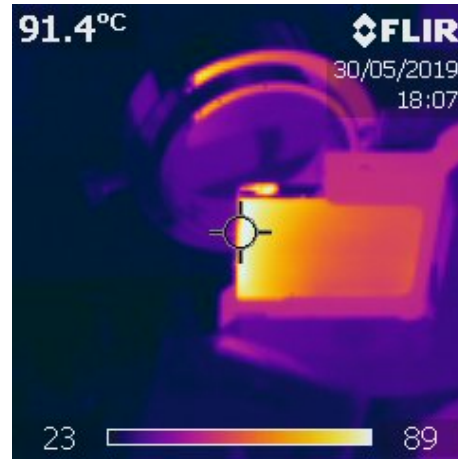


(b) grating: temperature gradient from side to side of grating from 91.4°C to 58.3°C.

Figure 5.9: Heat images of grating and prism at full power (83 W incoming, 57 W transmitted).

While the convergence is caused by mode matching lenses on the path to the beam profiler, it is exaggerated by the spread of the beam profile in x-direction that is caused by the compressor.

The convergence present even at 30 W of transmitted power, prohibits cavity operation. A collimated beam profile is mandatory for a pulse to circulate hundreds of times in a cavity with minimal losses.

The thermal origin of the beam profile distortions is confirmed by taking images with a thermal camera at several laser powers. A heat up dependent on the laser power was observed. Heat images at maximal power are depicted in Fig. 5.9. In picture a) the four beam passages through the prism are clearly visible. The maximum temperature of 32°C is reached at the last passage before the beam leaves the compressor (upper right spot). During this passage the beam should have the same diameter as on the first passage but is less intense due to reflection and absorption losses. Apparently, the temperature is still higher than for the first passage. This may be caused by thermal lensing due to prior passages. On the grating, the beam passages are not visible, rather a temperature gradient is established from one side to the other side. On the left side where the beam enters and leaves the compressor the grating heats up to 91.4°C. Then the temperature drops continuously down to 58.3°C on the other side. The right side is in direct contact with the aluminum mount which is a much better heat conductor than the air on the left side, resulting in the observed gradient. The broadening of the beam profile in x-direction can be explained by thermal lensing. Inside the compressor the beam is broadened along the x-axis of the beam profiler, due to angular dispersion. Thus the intensity profile

along the x-axis is a broadened gaussian. Consequently a heat gradient sand thus a thermal lens of the same shape is established at the prism passages.

# 6 Grating compressor

In this chapter, the commissioning of a compressor consisting of a $800\,\text{lines/mm}$ grating and two retroreflectors, with two quadratic HR mirrors, is covered. The goal of this assembly is to investigate the compression performance of a compressor that omits the compensation of third order dispersion. Furthermore, a quantitative dispersion measurement with comparison to the theory will be carried out.

## 6.1 Compression performance

The SHG signal of both autocorrelator arms was optimized to find the optimum distance between grating and the retroreflector on the home-built rail. A trace that matches the shape of the spectral cubic phase (SCP) trace in the theory section Fig. 2.19b, is measured over 82 delay steps with a temporal spacing of $26.67\,\text{fs}$ which corresponds to $4\,\mu\text{m}$ in space. The laser is operated at full power with a output average power of $69\,\text{W}$ behind the compressor. The trace is shown in Fig. 6.1, retrieval parameters in Tab. 6.1 and the full error budget in the Appendix in Fig. A.6. The GDD absolute value is pretty low compared to the TOD, as in the

Table 6.1: Retrieval parameters of grating compressed pulses at $69\,\text{W}$ transmitted power. Optimized SHG signal of both autocorrelator arms.

| $\text{GDD}_{\text{fit}}\,[\text{fs}^2]$ | $\text{TOD}_{\text{fit}}\,[\text{fs}^3]$ | $\tau\,[\text{fs}]$ | BW [nm] | FROG error |
|---|---|---|---|---|
| $(2.9 + 1.8 - 1.6 \pm 0.03)$ | $(7.5 + 0.1 - 1.6 \pm 0.03)$ | 223 | 10.6 | 0.00516 |

previous chapter's Tab. 4.3. As discussed in the previous chapter the GDD cannot be determined precisely in this regime. Therefore it's value should be considered as a rough estimate, which shows that the GDD is almost fully compensated. The TOD has a surprisingly big uncertainty when compared to the difference of true and retrieved value of the first dispersion value set in Tab. 4.3. Especially considering that the PSSDR amounts to 4405 here compared to a PSSDR of 100 corresponding to the values in the referred table.

Besides, the reconstructed dispersion parameters as well as the trace concur that TOD is the dominant remaining form of dispersion. It was estimated that the uncompressed $24\,\text{ps}$ pulses have positive GDD and TOD caused by propagation through $60\,\text{m}$ of fused silica fiber during their generation. Also a grating compressor infers only negative GDD and positive TOD as mentioned in Chapter 2.1.3. Consequently, while the GDD can be compensated, the TOD will even be amplified by a grating compressor. Thus at this grating constant and diffraction efficiency, perfect compression is not achievable. Since the TOD over GDD ratio rises with the groove
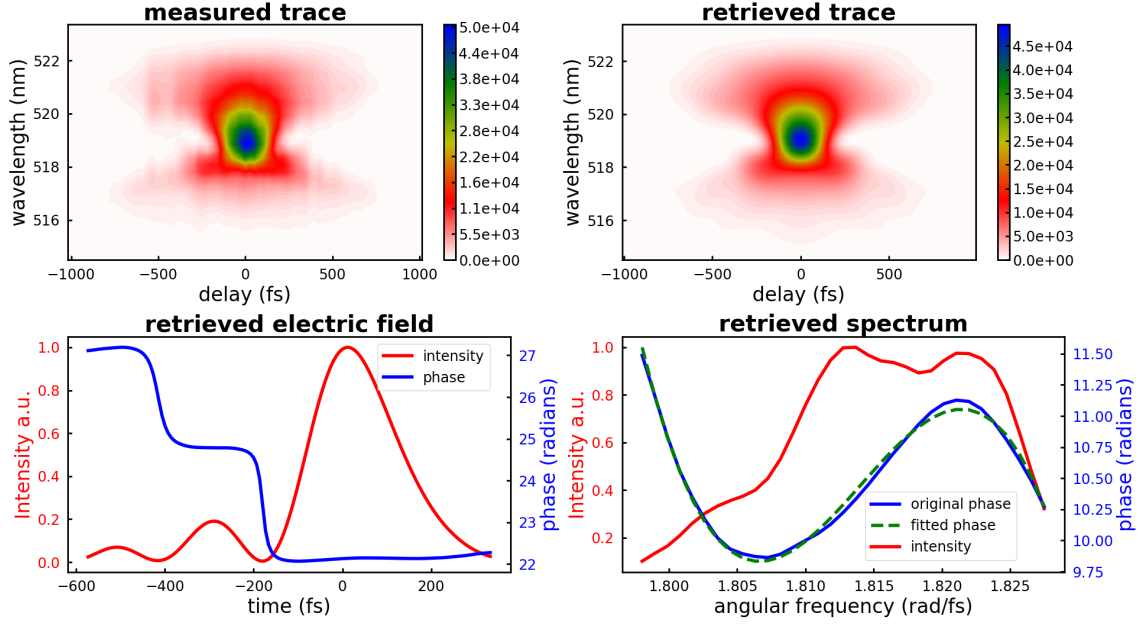
Figure 6.1: Retrieval of 222 fs pulses compressed by a grating compressor at 69 W transmitted power. A 3rd order polynomial was fit to the phase of the spectral electric field.

density Hemmer [2011], a grating of lower groove density is necessary to introduce the same amount of GDD and simultaneously less TOD.

## 6.2 Quantitative dispersion measurement by FROG

In this section, the dispersion prediction performance of the experimental setup coupled with the FROG retrieval algorithm is tested. This is done by measuring FROG traces at various retroreflector positions and reconstructing the dispersion values by fitting polynomials to the retrieved spectral phase in the same manner as in previous chapters. Then the difference between these dispersion values per distance is calculated and compared to the theoretically expected values determined by the equations 2.14 and 2.15 at the same distance.

The laser is operated at full power to test the performance under the most extreme conditions in the laboratory. The average power after the amplifier amounts to 80 W of which 60 W are transmitted by the grating compressor. The stage holding the retroreflector is moved over a range of 15 mm in steps of 1.5 mm or 3 mm, equal to 3 or 6 revolutions of the translation stage micrometer screw, respectively. However, in the grating compressor not the distance between the gratings along the beam path but the perpendicular grating separation is the parameter of interest. The shift of the translation stage actually applies twice, since the beam has to travel the

distance back and forth. Then, the diffraction angle has to be taken into account to calculate the shift along the perpendicular of the grating surface rather than along the beam direction. FROG traces are measured back to back without adjusting the beam path onto previously measured positions using the beam profiler. The noise of the measured traces was removed using either two times 'edge', two times 'full spectrum' or both tools once to achieve the best noise reduction.

Afterwards the retrieved spectral phase was considered at points corresponding to a threshold intensity value of 10% of the maximum intensity. Subsequently polynomials of 2nd and 3rd degree were fit to it. The reconstructed dispersion values are plotted against the perpendicular grating separation in Fig. 6.2 and Fig. 6.3. The noise parameters and error budgets of all used traces are presented in the Appendix from Fig. A.7 to Fig. A.15. A linear fit to the experimental data has been car-
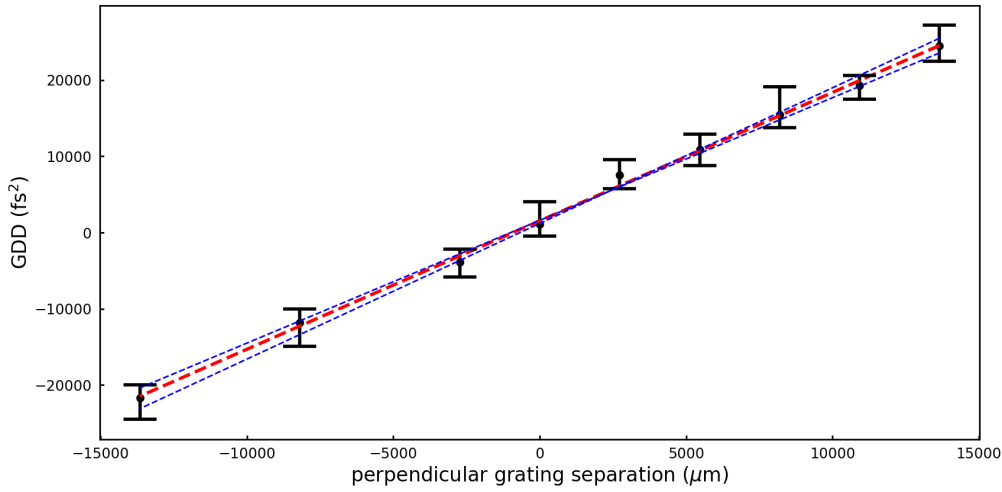
Figure 6.2: GDD as a function of the grating separation (black). The GDD was reconstructed from the spectral phase of retrieved SHG FROG traces, measured at an average output power of 65 W at various positions. The asymmetric error derives from the deviation of experimental and virtual pulses according to 4.3. The red dashed line is a linear fit to the data, the blue dashed lines are manually (due to asymmetric error) fitted lines for $1\sigma$ error estimation.

ried out (red dashed line) to determine the dispersion per distance by its slope and compare that to the dispersion per distance calculated from theory. Additionally, since the error bars are asymmetric two manual fits were carried out (blue dashed lines) to determine the $1\sigma$ uncertainty. For both forms of dispersion all values are within $2\sigma$ of the fitted line, most within $1\sigma$, which means that the accuracy within the error bars is good. However, while for the GDD the bare values form a clear line with positive slope, the bare values of TOD are more scattered and would even allow negative slopes in small subsets of the presented data. Therefore a single measurement is very accurate and precise in regards to the GDD but not in the same
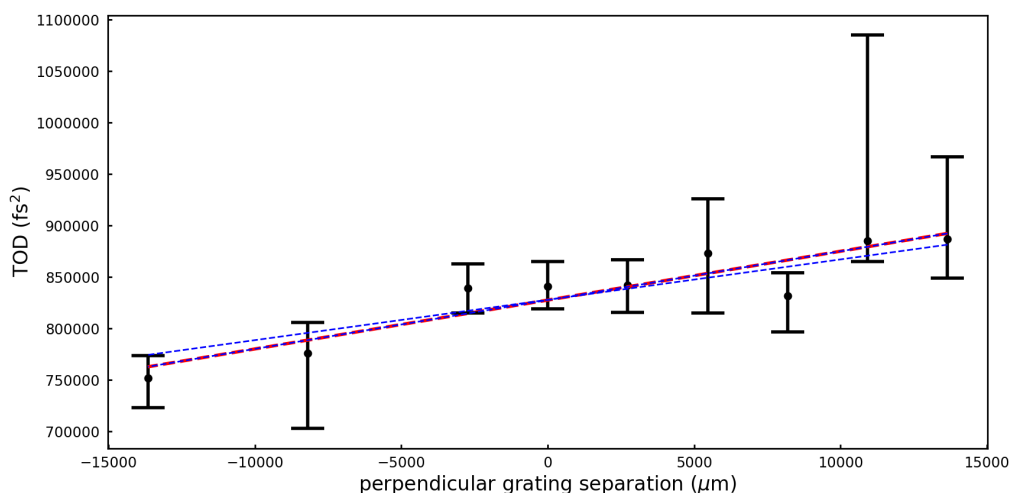
Figure 6.3: TOD as a function of the grating separation (black). The TOD was reconstructed from the spectral phase of retrieved SHG FROG traces, measured at an average output power of 65 W at various positions. The asymmetric error derives from the deviation of experimental and virtual pulses according to 4.3. The red dashed line is a linear fit to the data, the blue dashed lines are manually (due to asymmetric error) fitted lines for $1\,\sigma$ error estimation.

amount to the TOD. The high uncertainty of the TOD value at $11000\,\mu$m stems from very high background, see Appendix Fig. A.14. The results of the linear fit are presented in Tab. 6.2. Similarly to the previous discussion, the GDD per distance

Table 6.2: GDDpd and TODpd are GDD and TOD per distance, determined by theory or a fit to experimental data. The experimental data is plotted in Fig. 6.2 and 6.3.

| GDDpd$_{\text{fit}}$ $[\frac{\text{fs}^2}{\mu\text{m}}]$ | GDDpd$_{\text{theo}}$ $[\frac{\text{fs}^2}{\mu\text{m}}]$ | TODpd$_{\text{fit}}$ $[\frac{\text{fs}^3}{\mu\text{m}}]$ | TODpd$_{\text{theo}}$ $[\frac{\text{fs}^3}{\mu\text{m}}]$ |
|---|---|---|---|
| 1.7 + 0.2 - 0.1 | 1.68 | 4.7 + 0.0 - 0.8 | 3.94 |

(GDDpd) from experimental data is in very good agreement with the theory and the TODpd also agrees within $1\,\sigma$ with the theory although the error is larger here. In conclusion, the quantitative determination of dispersion by the home-built FROG setup is successful.

Now, after verification of this relative dispersion measurement, an absolute determination of the dispersion of the uncompressed pulses can be carried out. Therefore the grating to RR distance is measured at position $0\,\mu$m and converted to perpendicular grating separation which amounts to 47 cm. By subtraction of the grating dispersion parameters from those of the pulse the total dispersion is calculated, see Tab. 6.3.

Table 6.3: Total dispersion of the uncompressed pulses, determined by measurement of the perpendicular grating separation and the reconstructed dispersion parameters of a measured pulse.

| parameter | value |
|---|---|
| $GDD_{pulse}\,[fs^2]$ | $1.1 \cdot 10^3$ |
| $GDD_{grating}\,[fs^2]$ | $-7.2 \cdot 10^5$ |
| $TOD_{pulse}\,[fs^3]$ | $8.4 \cdot 10^5$ |
| $TOD_{grating}\,[fs^3]$ | $1.7 \cdot 10^6$ |
| $GDD_{total}\,[fs^2]$ | $7.2 \cdot 10^5$ |
| $TOD_{total}\,[fs^3]$ | $-0.84 \cdot 10^6$ |

## 6.3 Grating heat up

As shown in the previous chapter, the grating and prism heat up when operating at a high laser power beyond 10 W. In this section the grating heat up will be investigated further.

The temperature of the grating mounted in the kinematic mount (KMS by Thorlabs), same as in Fig. 5.9b was measured as a function of the average laser power before and after passing the compressor, see Tab. 6.4. At each power the temperature was measured after waiting five minutes for a steady state situation. After

Table 6.4: Temperature of uncooled grating as a function of average power before ($P_{before}$) and after ($P_{after}$) passing the compressor, after waiting 5 minutes at each laser power.

| $P_{before}\,[W]$ | $P_{after}\,[W]$ | Temperature [°C] |
|---|---|---|
| 9.0 | 7.0 | 31 |
| 21.8 | 17.2 | 44 |
| 43.1 | 30.6 | 64 |
| 71.6 | 53.7 | 88 |
| 83.2 | 62.6 | 95 |

20 minutes the grating reaches a temperature of 103°C. This is different from the GRISM compressor, where the grating reaches 91.4°C. Since the prism introduced some losses, more laser power passes the grating causing a stronger heat up.

To reduce the heat up, a copper strip connected to an aluminum body, is glued around the grating. Besides, the grating is now mounted on a Gimbaled three-axis optic tilt mount. The previous measurement is repeated with a waiting time of 10 minutes. The results are listed in Tab. 6.5. The attached cooling body reduces the maximum temperature of the grating by more than 30°C. As shown in Fig. 6.4 the gradient of temperature is reduced, however the minimum temperature of the grating, which was previously in Fig. 5.9b measured on the side of the grating mount, did not change. This confirms the hypothesis of the previous chapter. It

Table 6.5: Temperature of cooled grating as a function of average power before ($P_{before}$) and after ($P_{after}$) passing the compressor, after waiting 10 minutes at each laser power. *: This temperature was measured after 20 minutes of wait time.

| $P_{before}$ [W] | $P_{after}$ [W] | Temperature [°C] |
| --- | --- | --- |
| 9.5 | 6.5 | 31 |
| 23.5 | 16.8 | 36 |
| 46.0 | 34.0 | 48 |
| 81.6 | 62.4 | 68* |
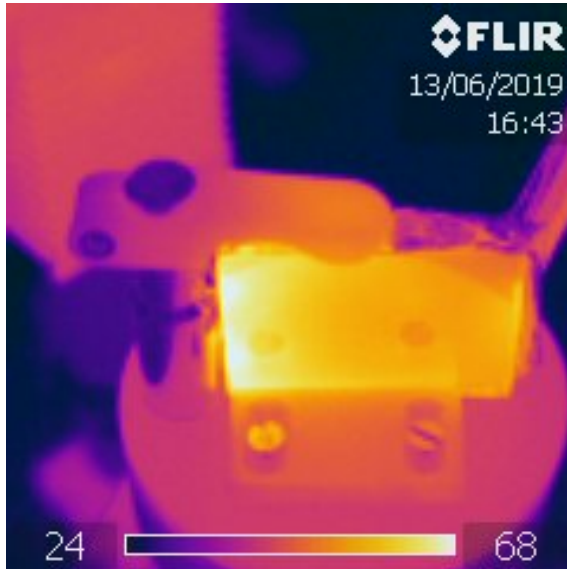


Figure 6.4: Heat image of grating surrounded by a copper strip, that is attached to an aluminum body.

was assumed that the temperature gradient is established due to the lack of a good heat conductor on the air-side of the grating opposed to the side in contact with the aluminum mount. Now the grating is surrounded completely by a good heat conductor and thus the heat is distributed more evenly. To investigate the quality of the beam and influence of heating, the beam profile was measured. The following beam profiles are measured at full power and maximal temperature, see Fig. 6.5b.

At position A the beam profile appears as a diamond shape and the intensity fades out over a much longer distance than the usual gaussian profile. At position B a sharp peak in the middle on top of a wider peak in x-direction is observed, this feature is not present at Position A. Filters in front of the beam profiler, which prevent the beam profiler from damage of the laser power, were checked for bad/damaged spots by tilting and translating them relative to the beam direction but no change was observed. Most likely the distortions are caused by the grating heat up. Therefore a grating with higher diffraction efficiency would be desirable, not only the output power would benefit but also the heat up may be reduced this way. The

(a) Position A           (b) Position B
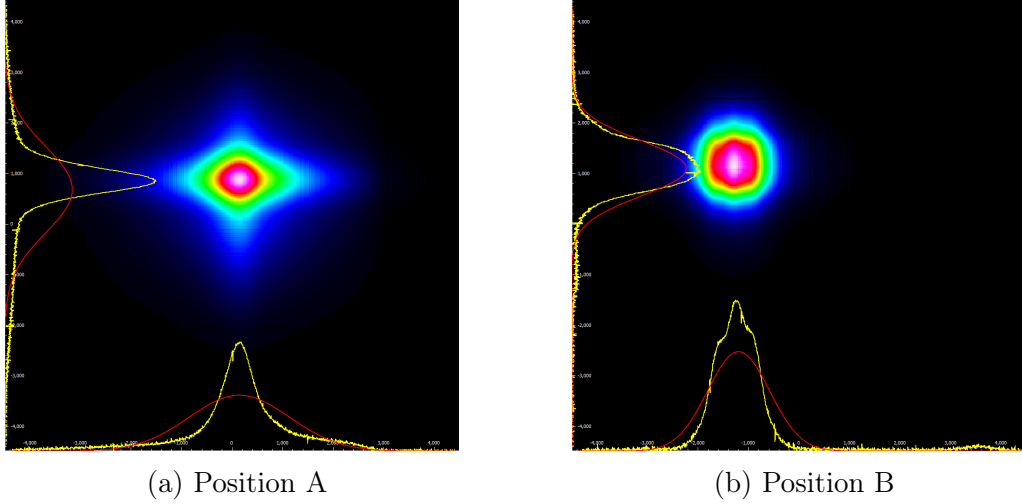
Figure 6.5: Two dimensional beam profiles behind grating compressor at 64 W transmitted power. Spatial intensity profile in x- and y-direction in yellow, gaussian fit in red.

beam profile is not perfectly, but less spread in x-direction at Position A and in general less distorted than the profiles at the same power behind the GRISM compressor in Fig. 5.8.

Now, to test whether the heat up of the grating affects the pulse compression two traces are measured. One at a low grating temperature, the other at a high temperature, but both while the rod-fiber is fully pumped. Thus, the only variable is the laser power passing the compressor. First, only 4 W, approximately 5% of the full power, are guided through the compressor. The temperature was not measured but should be less than 31°C according to Tab. 6.5. The trace is measured over 125 steps of $5\,\mu$m length, which equates to 33.33 fs of time delay per step, see Fig. 6.6 for the trace, Tab. 6.6 for the reconstructed parameters and in the Appendix Fig. A.16 for the error budget and noise parameters.

Table 6.6: Retrieval of a trace measured at 3 W after the compressor while the rod-fiber is fully pumped, resulting in a grating temperature below 31°C.

| $\mathrm{GDD_{fit}}\,[10^4\,\mathrm{fs}^2]$ | $\mathrm{TOD_{fit}}\,[10^5\,\mathrm{fs}^3]$ | $\tau$ [fs] | BW [nm] | FROG error |
|---|---|---|---|---|
| $(1.2 + \pm0.1 \pm 0.04)$ | $(7.8e + 05 + 0.2 - 2.0 \pm 0.1)$ | 266 | 8.8 | 0.00467 |

Then a trace is measured with the same compressor alignment as before, but now the full power is guided through the assembly. At an average power after the compressor of 60 W and a grating temperature of 67°C, the trace depicted in Fig 6.7 is measured over 100 delay steps of $7.5\,\mu$m length, which corresponds to 50 fs of time delay per step. The results of the retrieval are listed in Tab. 6.7, and the error budget as well as the noise parameters in the Appendix Fig. 6.7.

First of all, both FROG errors are around 0.5% and thus indicate an accurate
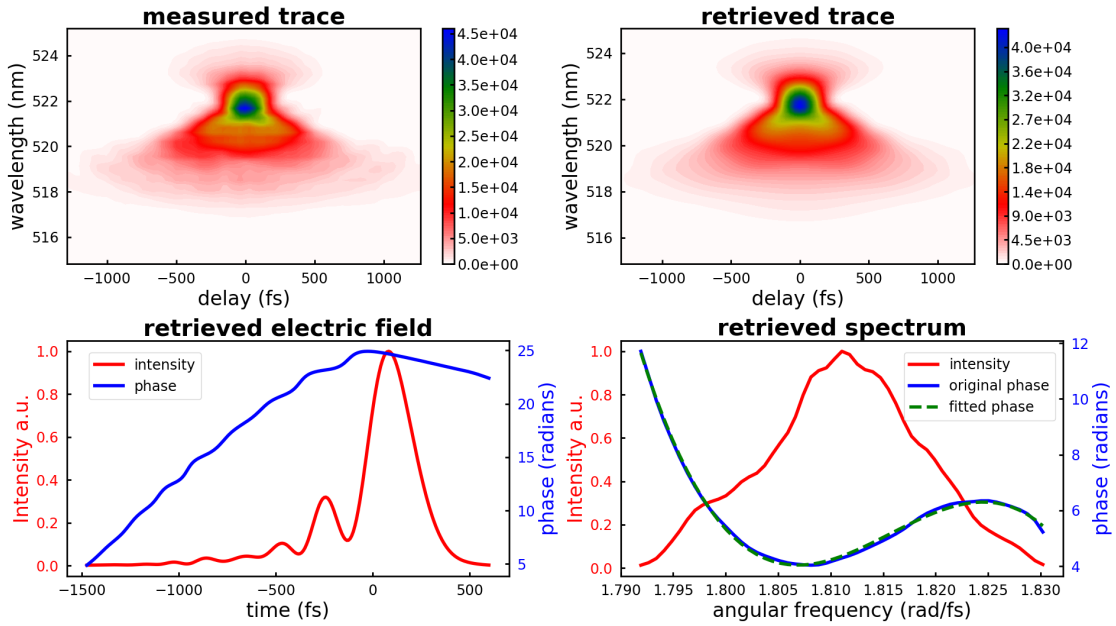
Figure 6.6: Retrieval of pulses at low power passing the grating compressor while rod-fiber is fully pumped. Less than 31°C grating temperature, 3 W average power after the compressor.
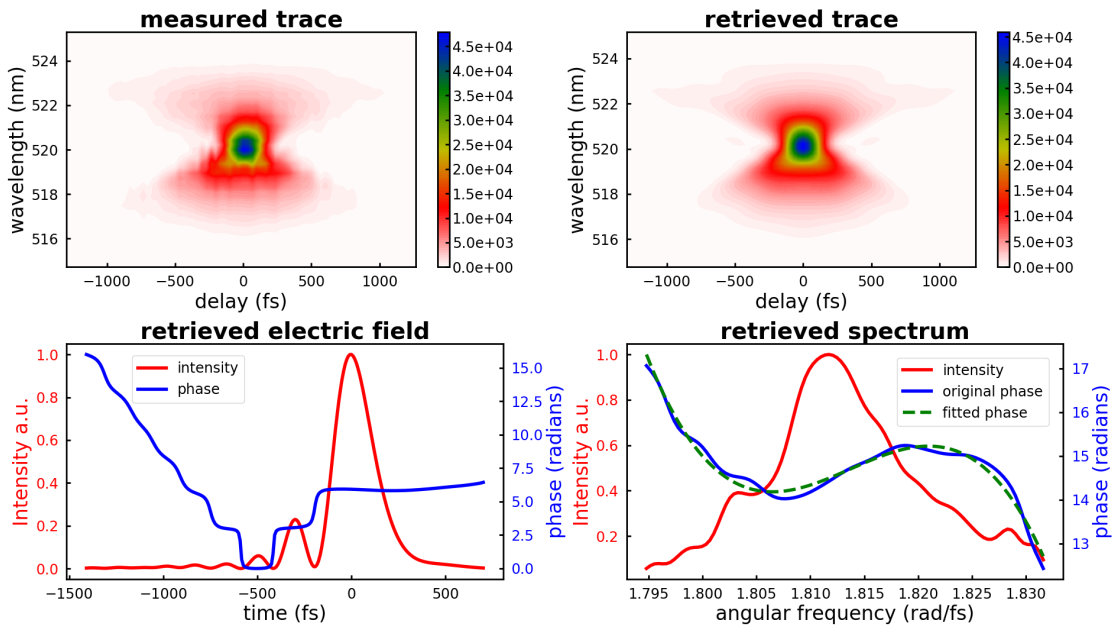


Figure 6.7: Retrieval of pulses at full power passing the grating compressor while rod-fiber is fully pumped with the same compressor alignment as for low power. 68°C grating temperature, 60 W average power behind the compressor.

Table 6.7: Retrieval of a trace measured at 60 W after the compressor while the rod-fiber is fully pumped, resulting in a grating temperature of approximately 67°C.

| GDD$_\text{fit}$ [$10^4$ fs$^2$] | TOD$_\text{fit}$ [$10^5$ fs$^3$] | $\tau$ [fs] | Bandwidth [nm] | FROG error |
|---|---|---|---|---|
| $(1.1 \pm 0.2 \pm 0.04)$ | $(8.7 + 0.3 - 0.6 \pm 0.4)$ | 271 | 11.4 | 0.00506 |

retrieval. The GDD values are the same, while the difference in TOD corresponds to less than $2\sigma$ according to the uncertainty of the fit and retrieval performance error. Consequently a significant difference in dispersion is not detectable. The deviation of the pulse duration is less than 2% and thus negligible. The cause of the discrepancy of 2.3 nm in bandwidth is not understood. A similar behavior was observed in a previous measurement, though there the low power trace had a higher bandwidth than the high power trace. In both cases two traces were measured, one directly after optimizing the compressor alignment at laser power 'a', while the alignment was not changed for the measurement of the second trace at a different power 'b'. The higher bandwidth is in both cases associated with the trace that was measured at the same power at which the compressor alignment was carried out. To summarize, it is ensured that the heat up of the grating does not alter the dispersion beyond the limits of the measurement accuracy.

# 7 Summary and Outlook

## 7.1 FROG setup

In this thesis a home-built FROG setup consisting of an autocorrelator and a spectrometer was commissioned. The existing spectrometer was rebuilt to cover a range of approximately 22 nm centered around 522 nm. A single 79 lines/mm Echelle grating is deliberately not operated at its blaze angle to enhance the angular dispersion and consequently enable the calibration with three Ne I transitions of a FeNe hollow cathode lamp, mentioned in Section 3.4.2.

Instead of the correct calibration values, a wavelength increment of 0.011445 nm/pixel and a wavelength offset of pixel 1 of 511.1891 nm, a wavelength increment of 0.011451 nm/pixel and wavelength offset of pixel 1 of 511.1774 nm were used throughout this thesis for calibration of the traces. However, the FROG retrieval program rounds the wavelength value corresponding to the first camera pixel to the first digit, which yields 511.2 nm for both calibrations. Over the 14 nm bandwidth of our laser the pixel-wavelength mapping would differ by 0.64 pixel. Or in other words, a 14 nm bandwidth is measured as 13.993 nm. In consideration of other uncertainties, discussed in the previous chapters, this difference is negligible.

Additionally, the readout of the spectrometer's line camera was adapted to be managed by python. This allowed the unification of the control of the autocorrelator's stepper motor and the camera to conveniently measure FROG traces using a single program. Subsequently various programs for data evaluation and visualization were written, which combined with a FROG retrieval algorithm and the built setup enable full pulse characterization including pulse duration, spectral bandwidth, intensity in both time and frequency domain as well as the phase in both domains.

## 7.2 Retrieval Performance

The performance of the retrieval algorithm, included in the program 'FROG' Version 3.2.4 from Femtosoft Technologies, was investigated. First, theoretically generated noise-free pulses with spectral phase distortions up to $10^5 \, \text{fs}^2$ of GDD and $10^7 \, \text{fs}^3$ of TOD were tested. The algorithm was able to reconstruct the dispersion values correctly up to 3 ps pulse duration, if GDD was dominant and up to 410 fs with a growing relative fit uncertainty of up to 50% in GDD, if TOD was dominant. Hence the range of dispersion values relevant in our experimental setup is covered.

Subsequently the retrieval performance on pulses with noise that is similar to the experimental noise was tested. The noise was simulated as additive noise from a gaus-

sian distribution, with a mean value equal to the peak signal to average background intensity ratio and a similarly quantified standard deviation. First the deviation of starting dispersion values, used for generation of the pulses, from the retrieved dispersion values depending on the subtraction tools used, was investigated. This comparison of the subtraction tools influence on the retrieval revealed that none of them significantly outperforms the others over three different sets of dispersion values, see Tab. 4.2.

Furthermore an error of the spectral phase based on theoretically generated traces with noise was calculated according to 4.3. However, the standard deviations were overestimated by a factor of two, consequently leading to an overestimation of the spectral phase uncertainty of experimentally measured pulses.

Additionally, it was found that the deviations of starting and retrieved dispersion values depend on the dispersion regime of the start values. In the regime of $8 \cdot 10^5 \, \mathrm{fs}^3$ of TOD, the TOD is overestimated. This is a typical TOD value of the measured grating compressed pulses, see Tab. 6.7. A change in GDD by one order of magnitude from $10^3 \, \mathrm{fs}^2$ to $10^4 \, \mathrm{fs}^2$, while the TOD was kept at $8 \cdot 10^5 \, \mathrm{fs}^3$ resulted in a change of relative GDD error from 18% to 35%. Therefore the procedure to determine deviations of the dispersion based on noise has to be carried out for each trace individually.

Over the course of this thesis, dispersion values of the measured trace are taken to generate theoretical pulses with noise similar to the experimental noise. Then, the retrieval of the noisy theoretical pulses suggests that, for example, the TOD is overestimated by approximately 10% in the presence of noise in the regime of $8 \cdot 10^5 \, \mathrm{fs}^3$ of TOD. However, the measured dispersion values may deviate from the true values, thus the calculated error may be based on false assumptions and at the true values the retrieval algorithm may react differently to the noise. Therefore an iterative treatment of the spectral error calculation would improve it's accuracy. The first step is the same as in this thesis, the measured dispersion values are considered for the spectral error calculation. Then, according to the determined error the start dispersion values are adjusted. In the example from above the starting dispersion values would be reduced by a small amount dependent on the size of the error, to compensate the overestimation. Subsequently this step is repeated until start dispersion values are found, which after the retrieval of the theoretical noisy trace yield the experimentally determined dispersion values. This procedure can be realized by using a retrieval algorithm in python in conjunction with the code already written during this thesis.

## 7.3 Results of the GRISM compressor

A GRISM compressor, consisting of a 800 lines/mm volume phase grating and a SF11 prism, was modeled, built and commissioned. The compressed pulses were characterized by the previously presented FROG setup. First, it was found that the design dispersion values of $+1.77 \cdot 10^6 \, \mathrm{fs}^2$ of GDD and $+2.86 \cdot 10^6 \, \mathrm{fs}^3$ of TOD of

the laser pulse, were not correct. Therefore, the arrangement had to be adjusted to achieve pulse compression. This was done first by tuning the angle $\beta$ between prism and grating, leading to great losses of approximately 50% because the incoming angle deviated from the Brewster angle and the anti-reflective coating was not suited for this purpose.

Another arrangement was found that compresses the seed laser, without pumping the rod-fiber, down to a temporal FWHM of 150 fs, shown in Fig. 5.3 and Tab. 5.1, with a transmission of approximately 68%, outperforming the commercial precompressed output which delivers pulses of 180 fs duration. The retrieved dispersion values of the GRISM compressed pulses are one order of magnitude smaller than those of the precompressed pulses and thus confirm the improved compression.

At a transmitted average power of 30 W a pulse duration of 192 fs was achieved,f see Fig. 5.5 and Tab. 5.3. Thus the average output power was tripled while the pulse duration is still competitive compared to the precompressed output.

At a maximum average output power of 57 W cavity operation using the compressed beam is prevented by a bad beam profile due to thermal lensing in the prism, shown in Fig 5.8. However, a transmission efficiency of 69% was demonstrated. Operation of the beam at a larger diameter inside the compressor and application of cooling, would decrease its intensity and consequently reduce the heat gradient that causes the observed thermal lens. A single shot based FROG setup would facilitate the search for the optimal GRISM arrangement and possibly enable compression below 190 fs after full amplification in the rod-fiber.


## 7.4 Results of the grating compressor

The grating compressor, utilizes the same grating as the GRISM and was built and commissioned over the course of this thesis. A quantitative measurement of the dispersion of experimental pulses was demonstrated by comparison to theoretical equations that describe the dispersion introduced in a double grating compressor. The distance between retroreflector and grating was changed over a range of 15 mm in steps of 3 or 6 mm. At every step a trace was recorded and retrieved. The reconstructed dispersion values were compared to the change in dispersion over the same distance according to Eq. 2.14 and Eq. 2.15. The results, shown in Fig. 6.2 and Fig. 6.3, demonstrate perfect agreement in determination of relative GDD and a deviation of 10% in TOD that agrees within $1\sigma$ with the theory. Furthermore an absolute dispersion measurement was carried out by combination of the dispersion parameters of a measured pulse and the grating compressor, whose parameters are based on the grating to RR distance during the FROG trace measurement of the pulse. The total dispersion found amounts to $7.2 \cdot 10^5$ fs$^2$ of GDD and $-0.84 \cdot 10^6$ fs$^3$ of TOD. A heat up of the grating was reduced from a maximum temperature of 103°C to 68°C by glueing a copper strip around it. A change in dispersion due to the heat up exceeding the measurement accuracy was not observed, see Tab. 6.6 and Tab. 6.7. The shortest reproducible pulse duration achieved is 223 fs at a trans-

mitted power of up to 69 W, shown in Fig. 6.1 and Tab. 6.1 with an acceptable beam profile, see Fig. 6.5.

To improve the grating compressor a new grating that possesses a higher diffraction efficiency as well as a lower groove density would be desirable. An increased diffraction efficiency would reduce the heat up and enable a higher transmitted power after compression. Since the total TOD of the uncompressed pulses is negative compression to the transform limit with a grating compressor is possible with the correct groove density. Besides, the efficiency of the GRISM would also benefit from a higher diffraction efficiency, since it is mainly limited by this currently. Utilizing the total dispersion parameters a new GRISM could be designed, to compensate

## 7.5 Comparison of grating and GRISM compressor

The grating compressor is a much simpler assembly compared to the GRISM compressor. The angle of incidence is determined by the Bragg condition and experimentally found by optimizing for power. The same holds for the incidence angle on the RRs. Adjusting for both angles is facilitated by the home-built rail. Then the only free parameter is the distance between the RR and grating. Consequently, the point of maximum compression is straightforward to find.

The GRISM on the other hand has far more free parameters, even though the incidence angle on the grating and prism are fixed in order to minimize power losses. Still a vast parameter space exists which derives from the position of the prism and the first RR in two dimensional space. That parameter space cannot be scanned in a fast manner like the one dimensional parameter space of the grating compressor by moving the RR on a rail. Instead, the prism has to be relocated beyond the range of the x-y stage, then the RR must be readjusted to be perpendicular to the beam path while introducing the correct horizontal shift. Additionally local minima of pulse duration can be encountered when more TOD at a approximately constant GDD leads to better compression. Furthermore the thermal lensing in the prism has to be reduced to achieve a higher quality beam profile that allows operation in the cavity.

Overall, the grating compressor is easier to operate, since setup and alignment are straightforward. Combined with the higher transmission efficiency and better beam profile, the grating compressor should be the choice for pulse compression, currently. Nonetheless, the GRISM compressor yields a better compression, possibly down to the transform limit, if the thermal lensing and alignment difficulty are overcome by previously mentioned methods. However, one needs to select the groove density very carefully.

# Part I
# Appendix

# A  Additional Information
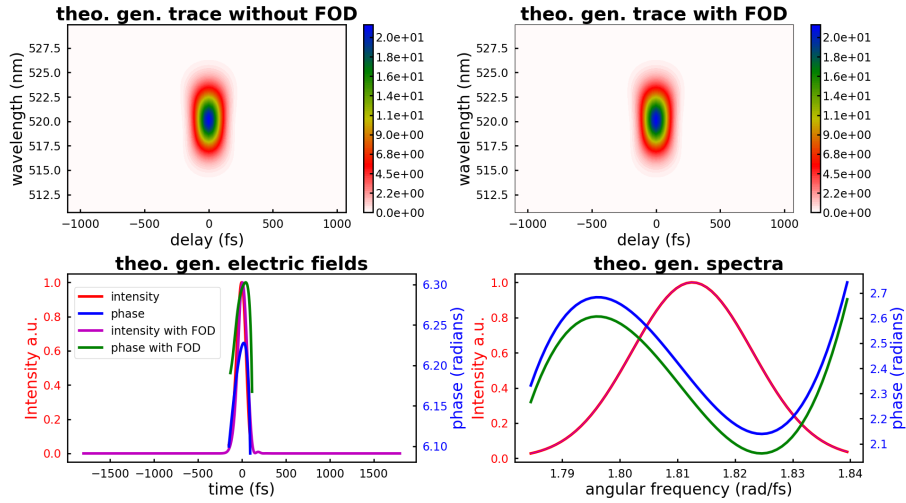
Figure A.1: Virtual trace with dispersion parameters of low power GRISM pulses with and without FOD.
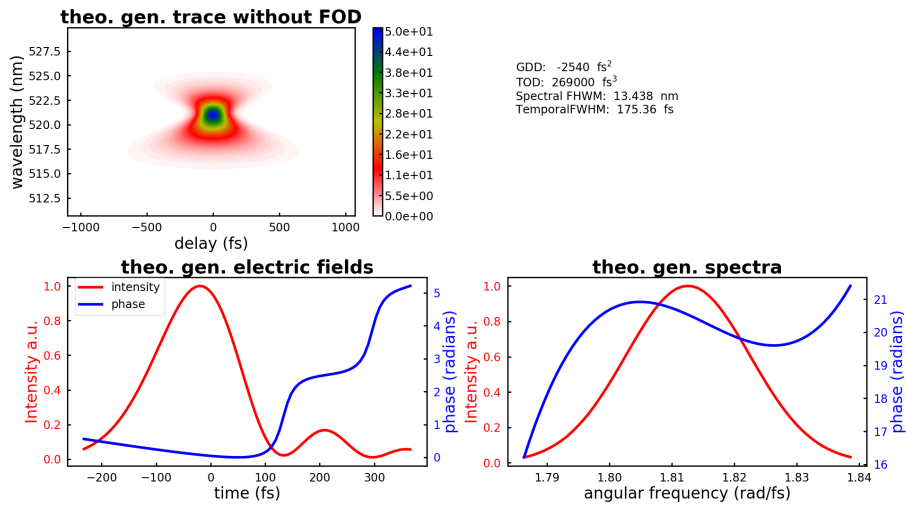


Figure A.2: Virtual trace with dispersion parameters of precompressed pulses.

## A.1 Error budgets and noise parameters of measured traces

```
PSNR: 90
PSSDR: 645
PSPR: 69
GDD_experimental_to_virtual_mean_error: -1.2e+02 fs^2
GDD_virtual_mean_fit_error:              +-5.5e+01 fs^2
GDD_experimental_fit_error:              +-1.5e+02 fs^2
GDD_systematic_error:                    (+2.0e+02 -1.6e+02) fs^2
GDD_statistical_error:                   +-1.0e+02 fs^2
TOD_experimental_to_virtual_mean_error: -1.6e+04 fs^3
TOD_virtual_mean_fit_error:              +-9.5e+02 fs^3
TOD_experimental_fit_error:              +-1.3e+04 fs^3
TOD_systematic_error:                    (+2.1e+04 -1.3e+04) fs^3
TOD_statistical_error:                   +-6.0e+03 fs^3
```

Figure A.3: GRISM compressed 150‚fs pulses at low power 6.4 W

```
PSNR: 602
PSSDR: 1128
PSPR: 148
GDD_experimental_to_virtual_mean_error: -1.1e+02 fs^2
GDD_virtual_mean_fit_error:              +-1.5e+02 fs^2
GDD_experimental_fit_error:              +-2.7e+02 fs^2
GDD_systematic_error:                    (+3.3e+02 -3.1e+02) fs^2
GDD_statistical_error:                   +-1.5e+01 fs^2
TOD_experimental_to_virtual_mean_error: 1.0e+03 fs^3
TOD_virtual_mean_fit_error:              +-7.7e+02 fs^3
TOD_experimental_fit_error:              +-2.9e+04 fs^3
TOD_systematic_error:                    (+2.9e+04 -2.9e+04) fs^3
TOD_statistical_error:                   +-1.1e+03 fs^3
```

Figure A.4: GRISM compressed 192 fs pulses at 30 W.

```
PSNR: 827
PSSDR: 5192
PSPR: 350
GDD_experimental_to_virtual_mean_error: -4.5e+02 fs^2
GDD_virtual_mean_fit_error:              +-4.4e+02 fs^2
GDD_experimental_fit_error:              +-4.0e+02 fs^2
GDD_systematic_error:                    (+5.9e+02 -7.5e+02) fs^2
GDD_statistical_error:                   +-1.6e+01 fs^2
TOD_experimental_to_virtual_mean_error: -4.0e+03 fs^3
TOD_virtual_mean_fit_error:              +-5.1e+02 fs^3
TOD_experimental_fit_error:              +-1.8e+04 fs^3
TOD_systematic_error:                    (+1.9e+04 -1.8e+04) fs^3
TOD_statistical_error:                   +-8.9e+02 fs^3
```

Figure A.5: Precompressed output, 181 fs pulses at 10 W.

```
PSNR: 1737
PSSDR: 4405
PSPR: 897
GDD_experimental_to_virtual_mean_error: -7.7e+02 fs^2
GDD_virtual_mean_fit_error:              +-1.2e+03 fs^2
GDD_experimental_fit_error:              +-1.1e+03 fs^2
GDD_systematic_error:                    (+1.8e+03 -1.6e+03) fs^2
GDD_statistical_error:                   +-2.5e+01 fs^2
TOD_experimental_to_virtual_mean_error: 1.6e+05 fs^3
TOD_virtual_mean_fit_error:              +-1.0e+03 fs^3
TOD_experimental_fit_error:              +-1.4e+04 fs^3
TOD_systematic_error:                    (+1.4e+04 -1.6e+05) fs^3
TOD_statistical_error:                   +-3.2e+03 fs^3
```

Figure A.6: Grating compressed 223 fs pulse at 69 W

```
PSNR: 546
PSSDR: 1282
PSPR: 276
GDD_experimental_to_virtual_mean_error: 2.3e+03 fs^2
GDD_virtual_mean_fit_error:              +-1.1e+03 fs^2
GDD_experimental_fit_error:              +-1.2e+03 fs^2
GDD_systematic_error:                    (+1.6e+03 -2.8e+03) fs^2
GDD_statistical_error:                   +-4.1e+02 fs^2
TOD_experimental_to_virtual_mean_error: 1.8e+04 fs^3
TOD_virtual_mean_fit_error:              +-1.7e+03 fs^3
TOD_experimental_fit_error:              +-2.0e+04 fs^3
TOD_systematic_error:                    (+2.1e+04 -2.7e+04) fs^3
TOD_statistical_error:                   +-8.3e+03 fs^3
```

Figure A.7: quantitative dispersion measurement: -13651 $\mu$m

```
PSNR: 473
PSSDR: 1531
PSPR: 253
GDD_experimental_to_virtual_mean_error: 2.5e+03 fs^2
GDD_virtual_mean_fit_error:              +-1.2e+03 fs^2
GDD_experimental_fit_error:              +-1.2e+03 fs^2
GDD_systematic_error:                    (+1.7e+03 -3.0e+03) fs^2
GDD_statistical_error:                   +-4.2e+02 fs^2
TOD_experimental_to_virtual_mean_error: 6.7e+04 fs^3
TOD_virtual_mean_fit_error:              +-1.2e+03 fs^3
TOD_experimental_fit_error:              +-2.8e+04 fs^3
TOD_systematic_error:                    (+2.8e+04 -7.3e+04) fs^3
TOD_statistical_error:                   +-9.8e+03 fs^3
```

Figure A.8: quantitative dispersion measurement: -8190 $\mu$m

```
PSNR: 1088
PSSDR: 2819
PSPR: 607
GDD_experimental_to_virtual_mean_error: 9.9e+02 fs^2
GDD_virtual_mean_fit_error:              +-1.2e+03 fs^2
GDD_experimental_fit_error:              +-1.1e+03 fs^2
GDD_systematic_error:                    (+1.6e+03 -1.9e+03) fs^2
GDD_statistical_error:                   +-3.1e+02 fs^2
TOD_experimental_to_virtual_mean_error: 8.0e+03 fs^3
TOD_virtual_mean_fit_error:              +-9.9e+02 fs^3
TOD_experimental_fit_error:              +-2.2e+04 fs^3
TOD_systematic_error:                    (+2.2e+04 -2.4e+04) fs^3
TOD_statistical_error:                   +-2.6e+03 fs^3
```

Figure A.9: quantitative dispersion measurement: –2730 $\mu$m

```
PSNR: 1834
PSSDR: 4566
PSPR: 734
GDD_experimental_to_virtual_mean_error: -1.5e+03 fs^2
GDD_virtual_mean_fit_error: +-1.4e+03 fs^2
GDD_experimental_fit_error: +-1.1e+03 fs^2
GDD_systematic_error: (+2.3e+03 -1.7e+03) fs^2
GDD_statistical_error: +-7.2e+02 fs^2
TOD_experimental_to_virtual_mean_error: 1.2e+05 fs^2
TOD_virtual_mean_fit_error: +-4.3e+03 fs^3
TOD_experimental_fit_error: +-2.2e+04 fs^3
TOD_systematic_error: (+2.2e+04 -1.3e+05) fs^3
TOD_statistical_error: +-2.8e+04 fs^3
```

Figure A.10: quantitative dispersion measurement: 0 $\mu$m

```
PSNR: 2125
PSSDR: 5316
PSPR: 726
GDD_experimental_to_virtual_mean_error: -9.5e+02 fs^2
GDD_virtual_mean_fit_error:             +-1.3e+03 fs^2
GDD_experimental_fit_error:             +-1.1e+03 fs^2
GDD_systematic_error:                   (+2.0e+03 -1.7e+03) fs^2
GDD_statistical_error:                  +-4.5e+02 fs^2
TOD_experimental_to_virtual_mean_error: 6.0e+03 fs^3
TOD_virtual_mean_fit_error:             +-9.3e+02 fs^3
TOD_experimental_fit_error:             +-2.5e+04 fs^3
TOD_systematic_error:                   (+2.5e+04 -2.6e+04) fs^3
TOD_statistical_error:                  +-3.9e+03 fs^3
```

Figure A.11: quantitative dispersion measurement: $2730 \, \mu$m

```
PSNR: 1205
PSSDR: 2631
PSPR: 384
GDD_experimental_to_virtual_mean_error: 5.0e+02 fs^2
GDD_virtual_mean_fit_error:             +-1.3e+03 fs^2
GDD_experimental_fit_error:             +-1.5e+03 fs^2
GDD_systematic_error:                   (+2.0e+03 -2.1e+03) fs^2
GDD_statistical_error:                  +-3.5e+02 fs^2
TOD_experimental_to_virtual_mean_error: 2.3e+04 fs^3
TOD_virtual_mean_fit_error:             +-2.3e+03 fs^3
TOD_experimental_fit_error:             +-2.9e+04 fs^3
TOD_systematic_error:                   (+2.9e+04 -3.7e+04) fs^3
TOD_statistical_error:                  +-4.4e+04 fs^3
```

Figure A.12: quantitative dispersion measurement: $5460 \, \mu$m

```
PSNR: 1080
PSSDR: 1584
PSPR: 373
GDD_experimental_to_virtual_mean_error: -3.2e+03 fs^2
GDD_virtual_mean_fit_error:             +-1.3e+03 fs^2
GDD_experimental_fit_error:             +-9.1e+02 fs^2
GDD_systematic_error:                   (+3.6e+03 -1.6e+03) fs^2
GDD_statistical_error:                  +-7.0e+02 fs^2
TOD_experimental_to_virtual_mean_error: 2.7e+04 fs^3
TOD_virtual_mean_fit_error:             +-3.3e+03 fs^3
TOD_experimental_fit_error:             +-1.5e+04 fs^3
TOD_systematic_error:                   (+1.5e+04 -3.1e+04) fs^3
TOD_statistical_error:                  +-1.6e+04 fs^3
```

Figure A.13: quantitative dispersion measurement: $8190 \, \mu$m

```
PSNR: 164
PSSDR: 366
PSPR: 120
GDD_experimental_to_virtual_mean_error: -1.1e+03 fs^2
GDD_virtual_mean_fit_error: +-9.5e+02 fs^2
GDD_experimental_fit_error: +-9.4e+02 fs^2
GDD_systematic_error: (+1.3e+03 -1.7e+03) fs^2
GDD_statistical_error: +-4.2e+02 fs^2
TOD_experimental_to_virtual_mean_error: -2.0e+05 fs^2
TOD_virtual_mean_fit_error: +-3.5e+03 fs^3
TOD_experimental_fit_error: +-1.5e+04 fs^3
TOD_systematic_error: (+2.0e+05 -1.5e+04) fs^3
TOD_statistical_error: +-1.5e+04 fs^3
```

Figure A.14: quantitative dispersion measurement: $10921 \, \mu$m

```
PSNR: 1195
PSSDR: 2526
PSPR: 743
GDD_experimental_to_virtual_mean_error: -1.9e+03 fs^2
GDD_virtual_mean_fit_error: +-1.2e+03 fs^2
GDD_experimental_fit_error: +-1.5e+03 fs^2
GDD_systematic_error: (+2.7e+03 -1.9e+03) fs^2
GDD_statistical_error: +-4.4e+02 fs^2
TOD_experimental_to_virtual_mean_error: -7.1e+04 fs^2
TOD_virtual_mean_fit_error: +-1.7e+03 fs^3
TOD_experimental_fit_error: +-2.6e+04 fs^3
TOD_systematic_error: (+7.6e+04 -2.6e+04) fs^3
TOD_statistical_error: +-2.7e+04 fs^3
```

Figure A.15: quantitative dispersion measurement: $13651\,\mu$m

```
PSNR: 1205
PSSDR: 2631
PSPR: 384
GDD_experimental_to_virtual_mean_error: 5.0e+02 fs^2
GDD_virtual_mean_fit_error:              +-1.3e+03 fs^2
GDD_experimental_fit_error:              +-1.5e+03 fs^2
GDD_systematic_error:                    (+2.0e+03 -2.1e+03) fs^2
GDD_statistical_error:                   +-3.5e+02 fs^2
TOD_experimental_to_virtual_mean_error: 2.3e+04 fs^3
TOD_virtual_mean_fit_error:              +-2.3e+03 fs^3
TOD_experimental_fit_error:              +-2.9e+04 fs^3
TOD_systematic_error:                    (+2.9e+04 -3.7e+04) fs^3
TOD_statistical_error:                   +-4.4e+04 fs^3
```

Figure A.16: Test effect of heat on dispersion $60\,$W after compressor

```
PSNR: 331
PSSDR: 2058
PSPR: 172
GDD_experimental_to_virtual_mean_error: 6.0e+02 fs^2
GDD_virtual_mean_fit_error:              +-8.0e+02 fs^2
GDD_experimental_fit_error:              +-9.7e+02 fs^2
GDD_systematic_error:                    (+1.3e+03 -1.4e+03) fs^2
GDD_statistical_error:                   +-2.6e+02 fs^2
TOD_experimental_to_virtual_mean_error: 1.9e+05 fs^3
TOD_virtual_mean_fit_error:              +-1.7e+03 fs^3
TOD_experimental_fit_error:              +-1.7e+04 fs^3
TOD_systematic_error:                    (+1.7e+04 -1.9e+05) fs^3
TOD_statistical_error:                   +-9.8e+03 fs^3
```

Figure A.17: Test effect of heat on dispersion $3\,$W after compressor

# B Lists

## B.1 List of Figures

76

# B.2  List of Tables

# C Bibliography

*FROG FastGuide Tutorial.*

A. Ackermann. Modellierung und charakterisierung eines kompressors für ultrakurze laserpulse durch strahlenverfolgung. Master's thesis, Ruprecht-Karls-Universität, Heidelberg., 2017.

Govind P. Agrawal. Nonlinear fiber optics. In P. L. Christiansen, M. P. Sørensen, and A. C. Scott, editors, *Nonlinear Science at the Dawn of the 21st Century*, pages 195–211, Berlin, Heidelberg, 2000. Springer Berlin Heidelberg. ISBN 978-3-540-46629-1.

David Attwood and Anne Sakdinawat. *Laser High Harmonic Generation*, page 279–314. Cambridge University Press, 2 edition, 2017. doi: 10.1017/9781107477629.010.

Edmond B. Treacy. Treacy, e.b. optical pulse compression with diffraction gratings. ieee j. quantum electron. qe-5, 454-458. *Quantum Electronics, IEEE Journal of*, 5:454 – 458, 10 1969. doi: 10.1109/JQE.1969.1076303.

H. Bekker, O. O. Versolato, A. Windberger, N. S. Oreshkina, R. Schupp, T. M. Baumann, Z. Harman, C. H. Keitel, P. O. Schmidt, J. Ullrich, and J. R. Crespo López-Urrutia. Identifications of euv transitions of promethium-like pt, ir, os and re. *Journal of Physics B: Atomic, Molecular and Optical Physics*, 48(14):144018, 2015. ISSN 0953-4075. URL http://stacks.iop.org/0953-4075/48/i=14/a=144018.

H. Bekker, C. Hensel, A. Daniel, A. Windberger, T. Pfeifer, and J. R. Crespo López-Urrutia. Laboratory precision measurements of optical emissions from coronal iron. *Phys. Rev. A*, 98:062514, Dec 2018. doi: 10.1103/PhysRevA.98.062514. URL https://link.aps.org/doi/10.1103/PhysRevA.98.062514.

J. C. Berengut and V. V. Flambaum. Manifestations of a spatial variation of fundamental constants in atomic and nuclear clocks, oklo, meteorites, and cosmological phenomena. *EPL (Europhysics Letters)*, 97(2):20006, jan 2012. doi: 10.1209/0295-5075/97/20006. URL https://doi.org/10.1209%2F0295-5075%2F97%2F20006.

J. C. Berengut, V. A. Dzuba, V. V. Flambaum, and A. Ong. Electron-hole transitions in multiply charged ions for precision laser spectroscopy and searching for variations in $\alpha$. *Phys. Rev. Lett.*, 106:210802, May 2011. doi:

10.1103/PhysRevLett.106.210802. URL https://link.aps.org/doi/10.1103/PhysRevLett.106.210802.

Eric D. Black. An introduction to pound–drever–hall laser frequency stabilization. *American Journal of Physics*, 69(1):79–87, 2001. doi: 10.1119/1.1286663. URL https://doi.org/10.1119/1.1286663.

Robert A. A. Campbell, Robert W. Eifert, and Glenn C. Turner. Openstage: A low-cost motorized microscope stage with sub-micron positioning accuracy. *PLOS ONE*, 9(2):1–18, 02 2014. doi: 10.1371/journal.pone.0088977. URL https://doi.org/10.1371/journal.pone.0088977.

P. Corkum and F. Krausz. Attosecond science. *Nature Physics*, 3, June J2007.

K. W. DeLong, Rick Trebino, J. Hunter, and W. E. White. Frequency-resolved optical gating with the use of second-harmonic generation. *J. Opt. Soc. Am. B*, 11(11):2206–2215, Nov 1994a. doi: 10.1364/JOSAB.11.002206. URL http://josab.osa.org/abstract.cfm?URI=josab-11-11-2206.

K. W. DeLong, Rick Trebino, and Daniel J. Kane. Comparison of ultrashort-pulse frequency-resolved-optical-gating traces for three common beam geometries. *J. Opt. Soc. Am. B*, 11(9):1595–1608, Sep 1994b. doi: 10.1364/JOSAB.11.001595. URL http://josab.osa.org/abstract.cfm?URI=josab-11-9-1595.

Kenneth W. DeLong and Rick Trebino. Improved ultrashort pulse-retrieval algorithm for frequency-resolved optical gating. *J. Opt. Soc. Am. A*, 11(9):2429–2437, Sep 1994. doi: 10.1364/JOSAA.11.002429. URL http://josaa.osa.org/abstract.cfm?URI=josaa-11-9-2429.

Kenneth W. DeLong, David N. Fittinghoff, Rick Trebino, Bern Kohler, and Kent Wilson. Pulse retrieval in frequency-resolved optical gating based on the method of generalized projections. *Opt. Lett.*, 19(24):2152–2154, Dec 1994c. doi: 10.1364/OL.19.002152. URL http://ol.osa.org/abstract.cfm?URI=ol-19-24-2152.

Andrei Derevianko, V. A. Dzuba, and V. V. Flambaum. Highly charged ions as a basis of optical atomic clockwork of exceptional accuracy. *Phys. Rev. Lett.*, 109:180801, Oct 2012. doi: 10.1103/PhysRevLett.109.180801. URL https://link.aps.org/doi/10.1103/PhysRevLett.109.180801.

J.-C. Diels and W. Rudolph. *Ultrashort Laser Pulse Phenomena: Fundamentals, Techniques and Applications on a Femtosecond Time Scale.* Academic Press, 1996.

Janko Nauta et al. Towards precision measurements on highly charged ions using a high harmonic generation frequency comb. *ScienceDirect*, 2017.

Michael Hemmer. *"Few-cycle Pulses Amplification For Attosecond Science Applications Modeling And Experiments"*. PhD thesis, University of Central Florida, 2011.

Daniel J. Kane and Rick Trebino. Single-shot measurement of the intensity and phase of an arbitrary ultrashort pulse by using frequency-resolved optical gating. *Opt. Lett.*, 18(10):823–825, May 1993. doi: 10.1364/OL.18.000823. URL http://ol.osa.org/abstract.cfm?URI=ol-18-10-823.

Jeffrey L. Krause, Kenneth J. Schafer, and Kenneth C. Kulander. High-order harmonic generation from atoms and ions in the high intensity regime. *Phys. Rev. Lett.*, 68:3535–3538, Jun 1992. doi: 10.1103/PhysRevLett.68.3535. URL https://link.aps.org/doi/10.1103/PhysRevLett.68.3535.

Morton A Levine, R E Marrs, J R Henderson, D A Knapp, and Marilyn B Schneider. The electron beam ion trap: A new instrument for atomic physics measurements. *Physica Scripta*, T22:157–163, jan 1988. doi: 10.1088/0031-8949/1988/t22/024. URL https://doi.org/10.1088%2F0031-8949%2F1988%2Ft22%2F024.

Janko Nauta, Andrii Borodin, Hans B. Ledwa, Julian Stark, Maria Schwarz, Lisa Schmöger, Peter Micke, José R. Crespo López-Urrutia, and Thomas Pfeifer. Towards precision measurements on highly charged ions using a high harmonic generation frequency comb. *Nuclear Instruments and Methods in Physics Research Section B: Beam Interactions with Materials and Atoms*, 408:285 – 288, 2017. ISSN 0168-583X. doi: https://doi.org/10.1016/j.nimb.2017.04.077. URL http://www.sciencedirect.com/science/article/pii/S0168583X17305281. Proceedings of the 18th International Conference on the Physics of Highly Charged Ions (HCI-2016), Kielce, Poland, 11-16 September 2016.

T. L. Nicholson, S. L. Campbell, R. B. Hutson, G. E. Marti, B. J. Bloom, R. L. McNally, W. Zhang, M. D. Barrett, M. S. Safronova, G. F. Strouse, W. L. Tew, and J. Ye. Systematic evaluation of an atomic clock at 2 10-18 total uncertainty. *Nature Communications*, 6:6896, April 2015. URL http://dx.doi.org/10.1038/ncomms7896.

Christian Reinhold Ott. *Attosecond multidimensional interferometry of single and two correlated electrons in atoms*. PhD thesis, Ruperto-Carola-University of Heidelberg, Germany, 2012.

Jérôme Paye, Malini Ramaswamy, James G. Fujimoto, and Erich P. Ippen. Measurement of the amplitude and phase of ultrashort light pulses from spectrally resolved autocorrelation. *Opt. Lett.*, 18(22):1946–1948, Nov 1993. doi: 10.1364/OL.18.001946. URL http://ol.osa.org/abstract.cfm?URI=ol-18-22-1946.

T. Rosenband, D. B. Hume, P. O. Schmidt, C. W. Chou, A. Brusch, L. Lorini, W. H. Oskay, R. E. Drullinger, T. M. Fortier, J. E. Stalnaker, S. A. Diddams,

W. C. Swann, N. R. Newbury, W. M. Itano, D. J. Wineland, and J. C. Bergquist. Frequency ratio of al+ and hg+ single-ion optical clocks; metrology at the 17th decimal place. *Science*, 319(5871):1808–1812, 2008. ISSN 0036-8075. doi: 10.1126/science.1154622. URL https://science.sciencemag.org/content/319/5871/1808.

M. S. Safronova, V. A. Dzuba, V. V. Flambaum, U. I. Safronova, S. G. Porsev, and M. G. Kozlov. Highly charged ions for atomic clocks, quantum information, and search for $\alpha$ variation. *Phys. Rev. Lett.*, 113:030801, Jul 2014a. doi: 10.1103/PhysRevLett.113.030801. URL https://link.aps.org/doi/10.1103/PhysRevLett.113.030801.

M. S. Safronova, V. A. Dzuba, V. V. Flambaum, U. I. Safronova, S. G. Porsev, and M. G. Kozlov. Highly charged ag-like and in-like ions for the development of atomic clocks and the search for $\alpha$ variation. *Phys. Rev. A*, 90:042513, Oct 2014b. doi: 10.1103/PhysRevA.90.042513. URL https://link.aps.org/doi/10.1103/PhysRevA.90.042513.

S. Schiller. Hydrogenlike highly charged ions for tests of the time independence of fundamental constants. *Phys. Rev. Lett.*, 98:180801, Apr 2007. doi: 10.1103/PhysRevLett.98.180801. URL https://link.aps.org/doi/10.1103/PhysRevLett.98.180801.

L. Schmöger, O. O. Versolato, M. Schwarz, M. Kohnen, A. Windberger, B. Piest, S. Feuchtenbeiner, J. Pedregosa-Gutierrez, T. Leopold, P. Micke, A. K. Hansen, T. M. Baumann, M. Drewsen, J. Ullrich, P. O. Schmidt, and J. R. Crespo López-Urrutia. Coulomb crystallization of highly charged ions. *Science*, 347(6227):1233, March 2015. URL http://science.sciencemag.org/content/347/6227/1233.abstract.

G. Taft, A. Rundquist, M. M. Murnane, I. P. Christov, H. C. Kapteyn, K. W. DeLong, D. N. Fittinghoff, M. A. Krumbugel, J. N. Sweetser, and R. Trebino. Measurement of 10-fs laser pulses. *IEEE Journal of Selected Topics in Quantum Electronics*, 2(3):575–585, Sep. 1996. ISSN 1077-260X. doi: 10.1109/2944.571757.

Rick Trebino and Daniel J. Kane. Using phase retrieval to measure the intensity and phase of ultrashort pulses: frequency-resolved optical gating. *J. Opt. Soc. Am. A*, 10(5):1101–1111, May 1993. doi: 10.1364/JOSAA.10.001101. URL http://josaa.osa.org/abstract.cfm?URI=josaa-10-5-1101.

Rick Trebino, Kenneth W. DeLong, David N. Fittinghoff, John N. Sweetser, Marco A. Krumbügel, Bruce A. Richman, and Daniel J. Kane. Measuring ultrashort laser pulses in the time-frequency domain using frequency-resolved optical gating. *Review of Scientific Instruments*, 68(9):3277–3295, 1997. doi: 10.1063/1.1148286. URL https://doi.org/10.1063/1.1148286.

J. K. Webb, J. A. King, M. T. Murphy, V. V. Flambaum, R. F. Carswell, and M. B. Bainbridge. Indications of a spatial variation of the fine structure constant. *Phys. Rev. Lett.*, 107:191101, Oct 2011. doi: 10.1103/PhysRevLett.107.191101. URL https://link.aps.org/doi/10.1103/PhysRevLett.107.191101.

Erklärung:

Ich versichere, dass ich diese Arbeit selbstständig verfasst habe und keine anderen als die angegebenen Quellen und Hilfsmittel benutzt habe.

Heidelberg, den (Datum)          . . . . . . . . . . . . . . . . . . . . . . . . . . . . . . . . . . . . . .